Trinity College Dublin
Coláiste na Tríonóide, Baile Átha Cliath
The University of Dublin

TRINITY COLLEGE DUBLIN

DOCTORAL THESIS

Characterisation of Semiconductor Lasers for use as a Pump Source for Microresonators

Author:
MICHAEL MCDERMOTT

Supervisor:
PROF. JOHN DONEGAN

A thesis submitted to the University of Dublin for the degree of Doctor of Philosophy

August 9, 2023

Declaration of Authorship

I declare that this thesis has not been submitted as an exercise for a degree at this or any other university and that it is entirely my own work.

I agree to deposit this thesis in the University's open access institutional repository or allow the Library to do so on my behalf, subject to Irish Copyright Legislation and Trinity College Library conditions of use and acknowledgement.

I have read and I understand the plagiarism provisions in the General Regulations of the University Calendar for 2022/2023, found at http://www.tcd.ie/calendar. I have also completed the Online Tutorial on avoiding plagiarism 'Ready, Steady Write', located at http://tcd-ie.libguides.com/plagiarism/ready-steady-write

Signed:

Date:

Abstract

Optical frequency combs (OFCs) were first developed in the 1990s, initially as a means to count the cycles from atomic clocks. They have since proved very useful as a tool for metrology, sensing and frequency synthesis. John L. Hall and Theodor W. Hänsch would go on to be awarded the 2005 Nobel Prize in Physics for their contributions to the development of OFCs. These first combs were generated in optical fibre by a train of pulses from mode-locked femtosecond lasers. These systems were initially quite bulky, often taking up the entirety of a lab bench, and were therefore unsuitable for practical applications. Further research was therefore necessary in order to miniaturise these systems such that the light source as well as the medium for comb generation could be integrated together on a single chip. An important advancement in this regard has been the generation of OFCs in microresonators. These are structures which have dimensions on the micrometre scale, which is a step towards chip-scale operation.

Our research group has designed and tested microring resonators of varying geometries and made from different materials such as AlN and Si_3N_4 in order to generate OFCs. We have successfully generated octave-spanning frequency combs as well as Kerr-soliton frequency combs within these microresonators. A tunable semiconductor laser (TSL) amplified by an erbium-doped fibre amplifier (EDFA), is used as a pump source. Both of these are bench-top pieces of equipment and are quite bulky, so our attention has now turned towards miniaturising this setup. Another project that is being researched in our group is the slotted lasers project. This is where we have developed arrays of semiconductor lasers that are tunable over the C-band and O-band for use in optical communications, particularly dense wavelength division multiplexing (DWDM). These lasers have micrometre dimensions which are fabricated with surface slots for wavelength discrimination rather than a buried heterostructure. This makes the fabrication process much simpler and efficient. They are perfect for photonic integration but have significantly broader linewidths than the lasers typically used to pump microresonators as well as lower output power. If it can be shown that soliton comb generation is possible using such devices, they would present excellent candidates as an alternative pump source for our microresonators that would aid in development of a chip scale system.

This work brings together both of these projects and demonstrates a path towards integrating a microresonator with one of our slotted lasers on the same chip. Firstly, three slotted laser arrays are characterised with each array having a different slot design. The wavelength tunability, side-mode suppression ratio (SMSR), linewidth and output power are all investigated in order to determine which slot design results in a performance best suited

for use as a pump source. A slotted laser with wavelength near one of the resonance modes of a microresonator was then selected as a pump source. Despite the broader linewidth of the slotted laser compared with the TSL, it was shown that an octave-spanning Kerr soliton microcomb could be generated using the slotted laser by sweeping the current supplied in order to red-shift the wavelength. Turn-key generation of the soliton microcomb was then demonstrated by increasing the current supplied to the slotted laser in a single step. The soliton comb was reliably produced using both methods, however the soliton existence range was found to be narrower for the slotted laser compared with the TSL and the overall noise was found to be greater when the slotted laser was used. Finally, to demonstrate the generation of microwave frequencies from an OFC, a commercial packaged device based on slots was used to generate a dual comb consisting of a soliton comb and a primary comb. By beating the primary comb lines with the soliton comb lines, microwave frequencies were generated. Once again, the noise of the signals generated by the laser was considerably greater than that of signals produced with the TSL.

Successfully generating soliton microcombs with a slotted laser is a promising step for miniaturising the system. However, the EDFA was still found to be necessary when pumping with the slot laser. Future work will need to be done in both improving the output power and linewidth of the slotted lasers. Improving the quality (Q) factor of the resonators would also reduce the required input power from the pump laser.

Acknowledgements

First and foremost, my sincere thanks to Professor John Donegan for his mentorship, patience and kindness throughout this PhD. He has been incredibly supportive and accommodating, especially throughout the disruptions caused by the COVID pandemic. He is the best supervisor you could hope to have. Likewise, Dr Haizhong Weng has been a wonderful mentor and friend and it has been a pleasure to work with him especially in the latter half when I began to work on the combs project. Thanks as well to the others in the combs and lasers group. Soon-to-be-Dr Dovydas Mickus, Dr Robert McKenna, Dr Caolan Murphy, Dr Adnan Afridi, Dr Gaurav Jain, and Dr Sepideh Naimi who have been generous with their time and help over the years and who have just been great to spend time with in general. Thanks as well to my family, both in Waterford and my new family, The Sheehans in the US who have been so supportive throughout. A special thanks to my mother, who has always been my greatest supporter, and my Granny who has lit more candles for me than I can count. Most of all, I would like to thank Mary. Though she could not help me with the content of my thesis, she has helped me in every other aspect of my life with love and support. When this PhD started she was my girlfriend, then she became my fiancée and finally wife. I'm looking forward to what the future brings. Special mention to Ian and his dog/moose Storm for all the TV time and takeaways that helped me relax after hard days in the lab. I also appreciate all the cats I have crossed paths with over the course of my academic career, even Thomas. Shout out to Cal and Noir. RIP Cookie and RIP (presumably) Marmalade who has looked like death for years. I know Jellybean is still waiting at the window on Denmark Street for me to come back with chicken, I hope his new flatmates are feeding him enough.

Contents

List of Figures

List of Tables

Publications

1. Weng, Haizhong, Adnan Ali Afridi, Jing Li, **Michael McDermott**, Huilan Tu, Liam P. Barry, Qiaoyin Lu, Weihua Guo, and John F. Donegan. "Dual-mode microresonators as straightforward access to octave-spanning dissipative Kerr solitons." Apl Photonics 7, no. 6 (2022): 066103.

2. Afridi, Adnan Ali, Haizhong Weng, Jing Li, Jia Liu, **Michael McDermott**, Qiaoyin Lu, Weihua Guo, and John F. Donegan. "Breather solitons in AlN microresonators." Optics Continuum 1, no. 1 (2022): 42-50.

3. Afridi, Adnan Ali, Haizhong Weng, Jing Li, Robert McKenna, **Michael McDermott**, Huilan Tu, Qiaoyin Lu, Weihua Guo, and John F. Donegan. "Effect of thermal tuning and mode coupling on soliton microcombs in AlN microresonators." IEEE Journal of Selected Topics in Quantum Electronics (2022).

4. **McDermott, Michael**, Robert McKenna, Caolan Murphy, Dovydas Mickus, Hai-Zhong Weng, Sepideh Naimi, Qiaoyin Lu et al. "1.3 μm wavelength tunable single-mode laser arrays based on slots." Optics Express 29, no. 10 (2021): 15802-15812.

5. McKenna, Robert, Dovydas Mickus, Sepideh Naimi, Caolan Murphy, **Michael McDermott**, Simon Corbett, David McCloskey, and John Francis Donegan. "Spatially resolved self-heating and thermal impedance of laser diodes using CCD-TR imaging." OSA Continuum 4, no. 4 (2021): 1271-1281.

List of Abbreviations

AR	**A**nti **R**eflection
AWG	**A**rbitrary **W**aveform **G**enerator
BPD	**B**are **P**hoto**d**iode
CEO	**C**arrier **E**nvelope **O**ffset
CW	**C**ontinuous **W**ave
DBR	**D**istributed **B**ragg **R**eflector
DFB	**D**istributed **F**eed**B**ack
DKS	**D**issipative **K**err **S**oliton
DS-H	**D**elayed **S**elf-**H**eterodyne
ECDL	**E**xternal **C**avity **D**iode **L**aser
EDFA	**E**rbium **D**oped**F**iber **A**mplifier
FWHM	**F**ull **W**idth **H**alf **M**aximum
FWM	**F**our **W**ave **M**ixing
HR	**H**igh **R**eflection
FP	**F**abry **P**erot
FPC	**F**iber **P**olarisation **C**ontroller
FSR	**F**ree **S**pectral **R**ange
HSRL	**H**ybrid **S**quare-**R**ectangular **L**aser
MI	**M**odulation **I**nstability
OFC	**O**ptical **F**requency **C**omb
OSA	**O**ptical **S**pectrum **A**nalyser
QW	**Q**uantum **W**ell
RTO	**R**eal **T**ime **O**scilloscope
SER	**S**oliton **E**xistance **R**ange
SHG	**S**econd **H**armonic **G**eneration
SMM	**S**cattering **M**atrix **M**ethod
SMSR	**S**ide **M**ode **S**uppression **R**atio
SOA	**S**emiconductor **O**ptical **A**mplifier
TE	**T**ransverse **E**lectric
TEC	**T**hermo **E**lectric **C**ooler
THG	**T**hird **H**armonic **G**eneration
TIR	**T**otal **I**nternal **R**eflection
TM	**T**ransverse **M**agnetic
TMM	**T**ransfer **M**atrix **M**ethod
TSL	**T**unable **S**emiconductor **L**aser
WDM	**W**avelength **D**ivision **M**ultiplexing

Chapter 1

Introduction

1.1 Optical Frequency Combs

The 2005 Nobel Prize in Physics was awarded for contributions to the field of optics. Half of the prize was awarded to Roy J. Glauber for his "contribution to the quantum theory of optical coherence". The second half of the prize was shared between John L. Hall and Theodor W. Hänsch for their "contributions to the development of laser-based precision spectroscopy, including the optical frequency comb technique". These combs were achieved using mode-locked femtosecond lasers in optical fibre [1] [2]. A train of pulses from the laser which are periodic in the time domain can be represented in the frequency domain as a series of equally spaced modes. This is an optical frequency comb.

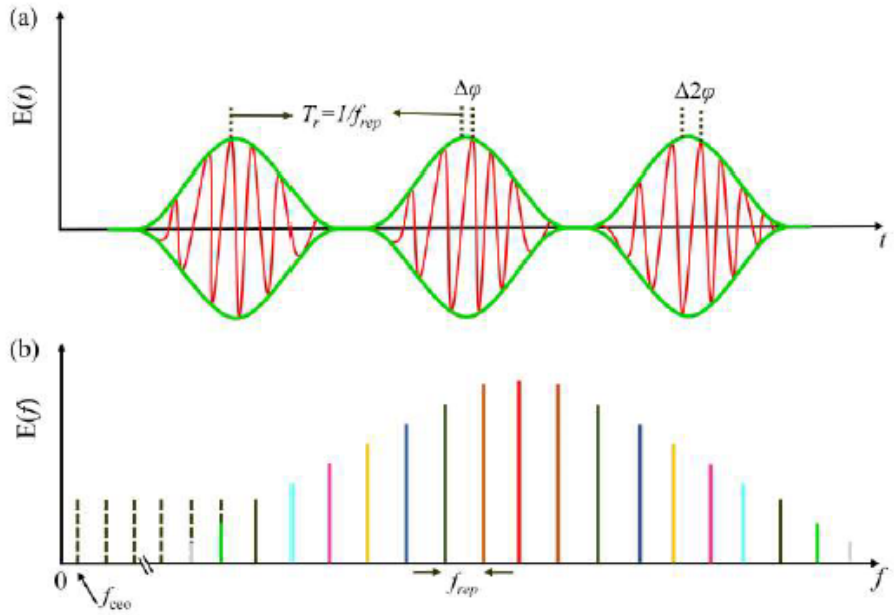

FIGURE 1.1: *a) pulse train in mode-locked laser. b) Optical spectrum in frequency domain.*

The pulses from the laser can be described as a quickly oscillating carrier wave and a more slowly varying envelope function. The relative position

between the carrier wave and the envelope changes due to effects such as dispersion, and this phase difference between the carrier wave and envelope is known as the carrier-envelope offset (CEO). Therefore, the spacing of the "teeth" of the comb generated in this way is given by:

$$f_n = f_{ceo} + nf_{rep} \tag{1.1}$$

where f_{rep} is the repetition rate, n is an integer and f_{ceo} is the carrier-envelope offset frequency. If both the repetition rate and the CEO frequency are known, then the frequency of every mode in the comb is then known. The repetition rate is easily determined from the optical spectrum in the frequency domain. However an octave-spanning comb, covering the spectrum of comb lines from n to $2n$, is required to accurately measure the carrier offset frequency. Once an octave spanning comb is achieved, the self-referencing f-2f scheme [3] [4] can be used. This is where $f_n = f_{ceo} + nf_{rep}$ is the comb line at the short end of the spectrum and $f_{2n} = f_{ceo} + 2nf_{rep}$ is the line at the long end of the spectrum as illustrated in 1.2.

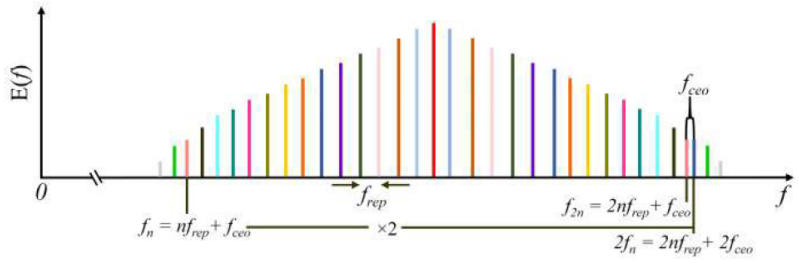

FIGURE 1.2: *Schematic illustration of f-2f self-reference scheme in an octave-spanning spectrum.*

f_n can be doubled by making use of the χ^2 non-linearity to produce the second harmonic, $2f_n$. By beating $2f_n$ with f_{2n}, the resulting beat note can be used to determine f_{ceo} as:

$$f_{ceo} = 2f_n - f_{2n} \tag{1.2}$$

1.2 Applications of Frequency Combs

Once all the mode frequencies are known, the comb can then be used as a reference to determine any unknown optical frequency within its span. This has many applications such as:

Low-noise microwave generation. Stabilised OFCs have been used to synthesise low noise, microwave signals with a hundredfold improvement in stability when compared with the highest performing electronic oscillators at room temperature [5].

Distance measurements and laser ranging. OFCs have been utilised in light detection and ranging (LIDAR) systems to great effect. OFC-based distance

measurements have been demonstrated at kHz measurement rates and micron ranging position while allowing for range measurements to objects at kilometre distances [6].

Spectroscopy. OFCs offer broad spectral bandwidth and high spatial coherence. This makes them ideal for use in a range of spectroscopic applications. These have included time-resolved spectroscopy [7] and high-precision molecular spectroscopy [8].

Other applications include optical frequency synthesizers [9], metrology [3] and optical clocks [10]. The majority of these applications are currently laboratory based and involve large systems which consume significant amounts of power. In order to expand the possible real-world applications for OFCs, such as integration with measurement devices on satellites where small size and efficiency is required, there is a strong motivation to miniaturise the systems required for OFC generation.

1.3 Microresonators

Previously developed systems for self-referenced optical frequency combs have been bulky, bench-top sized and sensitive to environmental change. For example, the first self-referenced frequency comb developed by Hänsch et al. at the Max-Planck Institute for Quantum Optics [11] is shown in Figure 1.3.

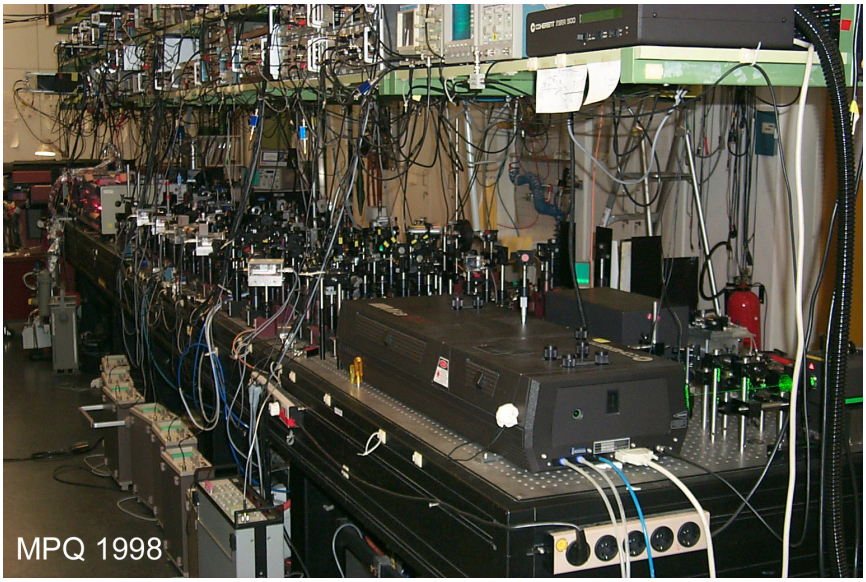

FIGURE 1.3: *The first self-referenced optical frequency comb at the Max-Planck Institute for Quantum Optics in 1998.*

The goal is therefore to develop a system whereby the light source as well as the medium for comb generation is reduced to chip-scale while still being able to operate with stability and to achieve an octave spanning comb for self-referencing. Microresonators are structures on the micron scale in which light can be confined and optical modes which satisfy some resonance condition can be generated. There have been many recent advances in OFC

generation using microresonators that have made chip-scale comb generation a feasible goal.
The generation of octave-spanning frequency combs in microresonators has been demonstrated for microring resonators, a microresonator in the shape of a ring which has micron dimensions, made from optically nonlinear material such as silicon nitride (Si_3N_4) or aluminium nitride (AlN) using a tunable laser whose power is amplified through an erbium-doped fibre amplifier (EDFA) [12] [13]. Another milestone was the demonstration that a soliton could be reliably generated by continuous-wave (CW) pumping of microresonators [14]. Solitons occur where the effects of optical nonlinearity and dispersion are in balance and the pulses can propagate through the waveguide without distortion [15]. The soliton state, when achieved, is highly stable. Our own group has demonstrated octave-spanning soliton frequency combs in AlN [16] and Si_3N_4 [17] microring resonators. The ability to produce stable, octave-spanning combs using a microring is an important step. However, the optical power and coherence required necessitates the use of a narrow linewidth tunable laser with its output boosted by an EDFA. To achieve on-chip operation, the pump source must also be miniaturised and integrated with the microresonator. Tunable diode lasers are ideal sources for this pump source and will be explored in this thesis.

1.4 Photonic Integration

The quality (Q) factor of a microresonator is a measure of the ability of the resonator to store energy and can be improved using methods such as mode delocalisation, incorporating a multimode structure and fabrication optimization to reduce sidewall roughness [18]. A higher Q resonator requires less input power for comb generation than a resonator with a poorer Q. A resonator with a sufficiently high Q and a diode laser with sufficient output power would eliminate the need for an EDFA, paving the way for both the microresonator and pump source to be integrated on-chip. Bowers et al. have demonstrated soliton comb generation using a low-noise external-cavity diode laser (ECDL) as a pump laser for a silica (SiO_2) microresonator with a Q factor [19]. With a linewidth as low as 63 Hz, they were able to generate a soliton comb with 70 mW of output power. The Bowers group has also demonstrated an integrated system of a commercial distributed-feedback (DFB) laser butt-coupled to a microresonator [20].
The lasers developed in our group's semiconductor laser project consist of surface-slotted single mode lasers designed for simple, monolithic photonic integration [21]. We have demonstrated arrays of such devices operating in the C-band a wide tuning range, high SMSR and relatively low linewidth [22], [23]. A semiconductor optical amplifier (SOA) has also been integrated to amplify the output power of the lasers [24]. We have also characterised such arrays designed for O-band operation [25] which is outlined in this thesis. The various designs are investigated and compared to determine their suitability for a pump source for comb generation in optical resonators.

1.5 Thesis Scope and Structure

The research work presented in this thesis is part of a funded project to develop chip-scale optical microresonators based on AlN and SiN materials. A key aspect of this work was the lasers to pump the resonators. As mentioned, our group has extensive experience in diode laser development based on surface-etched slots to form a high order grating. The initial plan was to use two diode lasers to pump the resonators, one centred near 1550 nm, the other near 1310 nm as we had suitable devices available. Chapter 2 of this thesis therefore deals with the background of semiconductor lasers. It is discussed how these devices are designed by our group to provide wavelength-stable and coherent CW operation while the simplicity of the design allows for easy fabrication and integration with other photonic systems. Chapter 3 then details the characterisation of several arrays of these lasers with a wavelength centred around 1310 nm. These arrays were originally designed with applications in optical communications such as dense wavelength-division multiplexing (DWDM). However the characterisation and contrasting of the different designs also gives insight into how future designs of these devices could be altered to improve their suitability as an integrated pump source for the microresonators, particularly the output power and the spectral linewidth. Our group has focused also on what we term dual-mode resonators. These are resonators where two modes are very close to one to one another from different mode families. We also investigate several hybrid square-rectangular lasers (HSRLs) which exhibit dual-lasing in order to determine whether these would work as a pump source to couple to the dual modes.

Chapters 4 and 5 detail the background theory behind the microring resonators used in our group as well as our experiments with using the slotted lasers as a pump source. The resonators obtained at the beginning of this project had a Q-factor of about 0.5 million. It was anticipated that the Q-factor would reach 5 x 10^6 or even 10^7 within a short time. While such values have been achieved [18], they are not easily achievable. To pump the resonators with Q-factor of about 1 million needs a few 100 mW power on chip. Such power levels are not available in the laser arrays we have in our group. We therefore need to combine these lasers with an EDFA to boost the power to the required level. We therefore used both a tunable external cavity commercial source and some lasers from our 1.5 micron arrays to act as pump sources in conjunction with the EDFA.

Chapter 2

Semiconductor Lasers

2.1 Energy Bands in Semiconductors

A single atom has discrete energy levels which electrons can occupy. When multiple atoms come into close proximity, the resulting perturbations cause the energy levels to split. As the number of atoms increases, so does the splitting of the energy levels. In a semiconductor material with a large number of atoms, these energy levels are close enough together to be considered a continuous band. Electrons will fill the lowest available energy level. The lower energy band is known as the valence band while the higher energy band is the conduction band. At $T = 0K$, the valence band is completely full while the conduction band is empty. The highest energy level which an electron can occupy at this temperature is known as the Fermi level (E_F) which lies between the valence and conduction bands. There is a gap between the highest level of the valence band and lowest level of the conductance band where no states exist which electrons can occupy. This difference in energy is the band gap energy (E_g). If sufficient energy is added to the system, electrons can be excited from the valence band to the conduction band provided they can overcome the band gap energy.

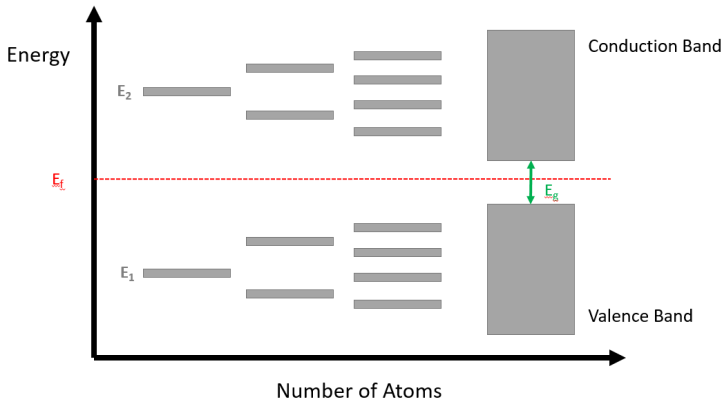

FIGURE 2.1: *Energy bands in solids.*

This 'band gap' (E_g) allows three main optical processes to occur: absorption, spontaneous emission and stimulated emission, which are illustrated in Figure 2.2.

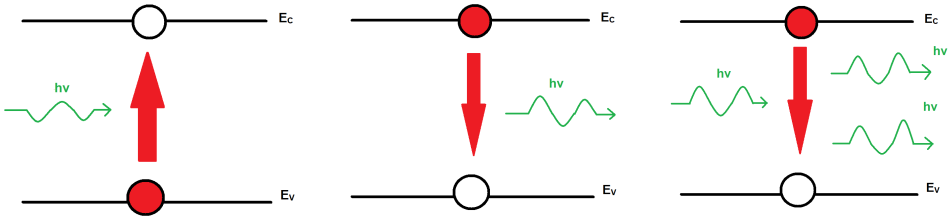

(a) *Absorption* (b) *Spontaneous Emission* (c) *Stimulated Emission*

FIGURE 2.2: *Optical processes in semiconductor materials.*

Absorption occurs when an incident photon with energy ($h\nu$) equal to or greater than the band gap energy is absorbed by an electron and is excited into the conduction band. This results in a positively charged quasiparticle called a 'hole' in the valence band.
Spontaneous emission occurs when an electron in the conduction band recombines with a hole in the valence band, resulting in the emission of a photon with an energy equivalent to energy difference between two states. This is a spontaneous process and the resulting photon will have a random phase and wavevector k. The rate of such an event occurring R_{sp} is proportional to the number of electron - hole pairs present. Therefore, $R_{sp} = BN^2$ where N is the carrier density and B is the bimolecular recombination coefficient.
Stimulated emission R_{stim} is when an incident photon induces an electron-hole recombination. The resulting photon will have the same phase and wavevector as the incident photon. It is this process that is vital to a laser's operation.
There can also be non-radiative recombination such as carrier leakage R_l through defects in the material, such a process is proportional to N. Auger recombination R_A occurs when a conduction band electron decays to fill a valence band hole, transferring kinetic energy to another conduction band electron. As there are two electrons and one hole involved, this process is proportional to N^3.

The band structure of a semiconductor is obtained by plotting the energy E of the valence and conduction bands against the corresponding wavevector. A material can be characterised as either 'direct' band-gap or 'indirect' band-gap as shown in Figure 2.3.

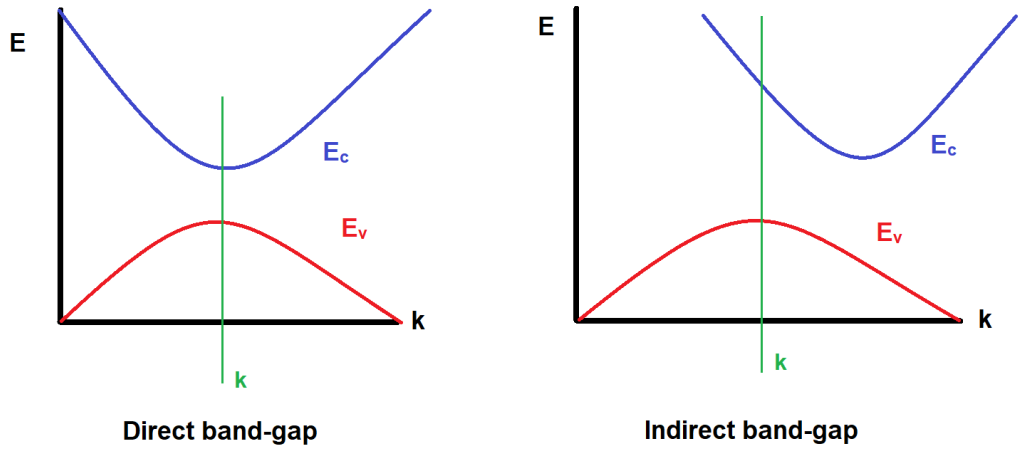

FIGURE 2.3: *Schematic of a direct and indirect band-gap.*

In an indirect band-gap material such as Si, the minimum conduction band energy and the maximum valence band energy occur at different wavevectors. Therefore, a change in momentum is required before an electron can transition between bands, which is an inefficient process requiring the participation of phonons. A direct band-gap is where the minimum conduction band energy and the maximum valence band energy coincide at the same wavevector. The transition then only involves energy transfer and is much more efficient. For this reason, direct band gap semiconductors such as GaAs, InP and GaN are used as the gain material in the active region of semiconductor lasers.
Semiconductor lasers are based on the principle of the double heterostructure, consisting of an undoped (intrinsic) active region sandwiched between an n-doped and p-doped region with a larger band gap An example of a double-heterostructure can be seen in Figure 2.4.

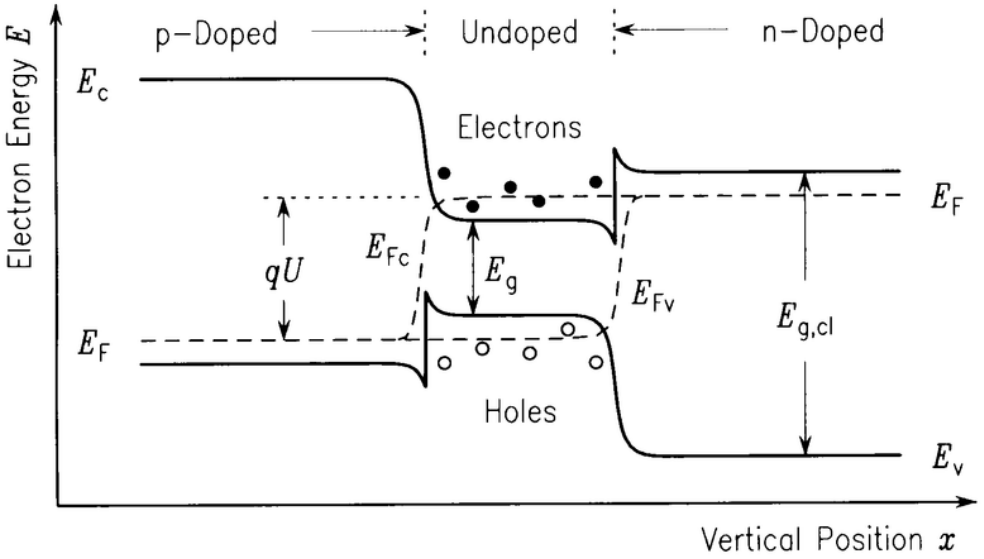

FIGURE 2.4: *An illustration of the band structure of a double-heterostructure with the active region sandwiched between a p-doped and n-doped region [26].*

Under forward bias, electrons from the n-doped region and holes from the p-doped region are injected into the active region. The high band gap on either side confines the carriers to the active region and forces electron-hole recombinations to occur in this region. Photons are therefore generated in this region at the band gap energy. A quantum well (QW) can be achieved by narrowing the width of this active region near to the de Broglie wavelength so that quantum confinement occurs. Since optical confinement results from the higher refractive index n of the active region relative to the surrounding doped regions, the narrowing of the active region to form a quantum well and improve carrier confinement results in decreased optical confinement. To maximise both carrier and optical confinement, a separate confinement heterostructure quantum well (SCH-QW) is utilised [27]. This consists of an additional cladding layer around the quantum well in order to improve the optical confinement. By alternating multiple active and cladding layers, a multiple quantum well (MQW) structure is obtained, which increases optical gain.

2.2 Optical Gain and the Fabry-Pérot Cavity

The simplest example of a laser is the Fabry-Pérot (FP) cavity, shown in Figure 2.5, and consists of a gain medium, energy source and feedback system.

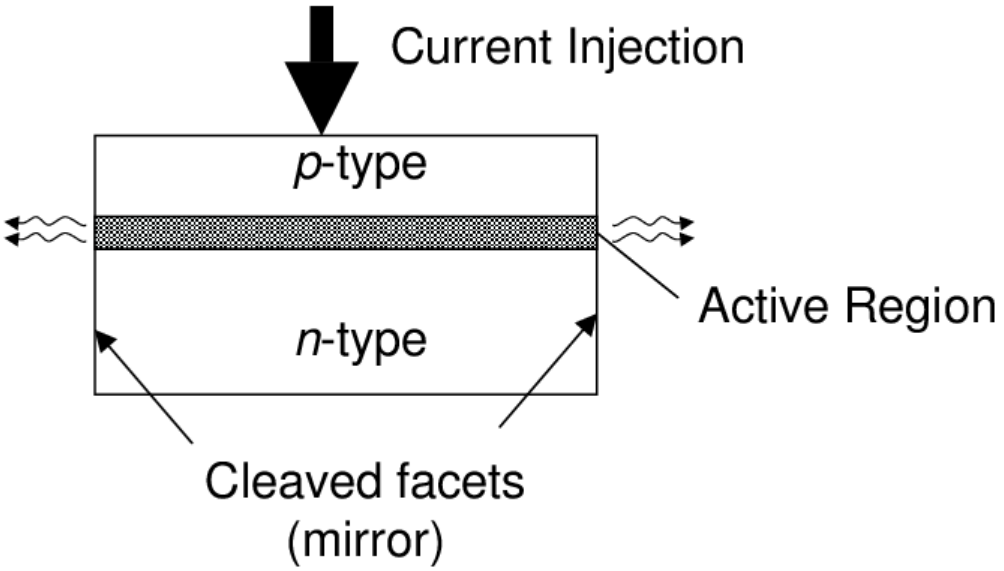

FIGURE 2.5: *Structure of a Fabry-Pérot cavity[28].*

The feedback system in an FP laser consists of two mirrors with reflectivities r_1 and r_2, respectively. In a semiconductor laser, the difference in refractive index between the semiconductor material and the surrounding air is sufficient to allow the cleaved facets to act as the partially reflected mirrors, allowing some of the light to transmit through and exit the cavity while confining the rest in the gain medium.
Light propagating through the cavity can be described by the propagation constant β [29]:

$$\beta = k_0 n_{eff} + i\frac{g_{net}}{2} \tag{2.1}$$

$$g_{net} = g\Gamma - \alpha_i \tag{2.2}$$

where k_0 is the free-space wavenumber, n_{eff} is the effective refractive index of the waveguide, g_{net} is the net modal gain, Γ is the confinement factor and α_i is the waveguide loss.
The lasing threshold is reached when the net gain over a round trip is equal to the losses over the same round-trip such that the wave replicates itself in one round-trip. This occurs when:

$$r_1 r_2 e^{-2i\beta L} = 1 \tag{2.3}$$

where r_1 and r_2 are the reflectivities of the front and back mirrors and L is the cavity length. The wavelengths at which lasing can occur are dependent on the optical path length of the cavity as they must have a constant phase after each round trip to add constructively. The longitudinal modes satisfying the resonance condition are given by:

$$\lambda_m = \frac{2n'_{eff}L}{m} \tag{2.4}$$

and the spacing of the longitudinal modes in the Fabry-Pérot cavity is:

$$\Delta\lambda_{FP} = \lambda_m - \lambda_{m+1} = \frac{\lambda_m^2}{2n_g L} \tag{2.5}$$

where n_g is the group refractive index.

Figure 2.6 shows the experimentally measured output spectrum of a Fabry-Pérot cavity along with the longitudinal modes that satisfy Equation 2.4. The wavelength relative to the modal gain curve determines the relative amplitude of the lasing modes.

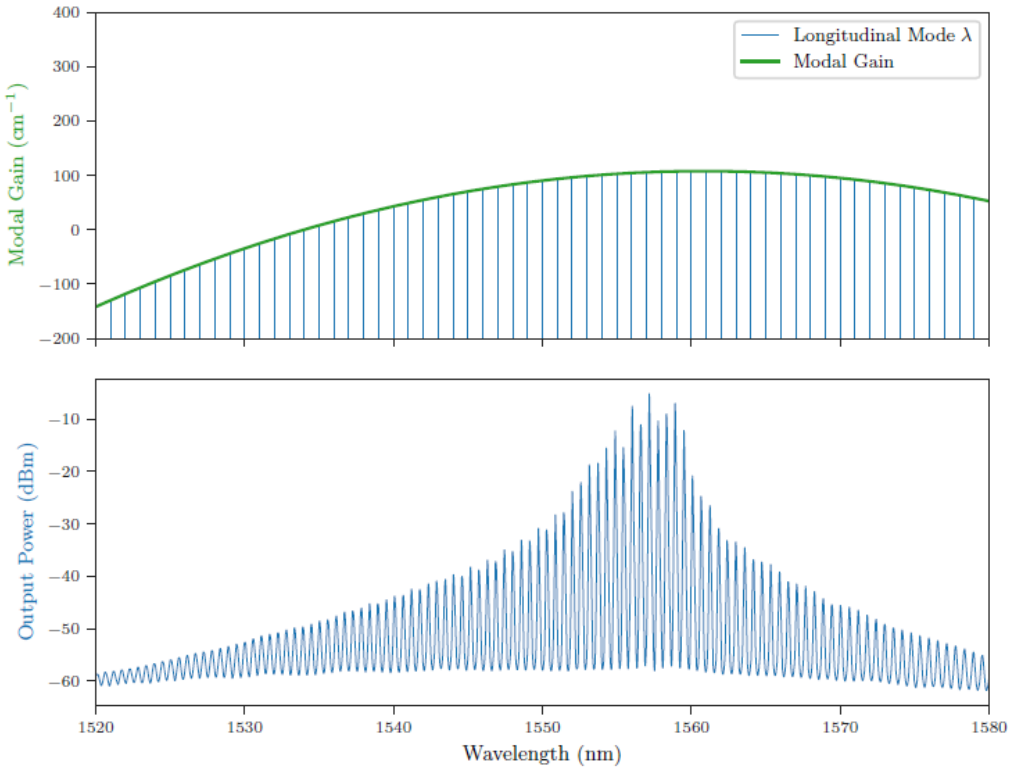

FIGURE 2.6: *Fabry-Pérot cavity's possible longitudinal modes and gain curve (top). Measured 400 µm Fabry-Pérot lasing spectrum at 60 mA (bottom). Data recorded by Dr Michael Wallace.*

The longitudinal cavity modes can be seen as well as the shape of the gain curve. The shape of the gain curve near threshold can be approximated as a parabola whose shape and peak position is determined by the carrier density and temperature in the active region [30]. The wavelength of a longitudinal mode relative to the gain curve determines the optical power of that mode.

2.3 Rate Equations and Lasing Threshold

In order for lasing to occur in a semiconductor diode, the number of conduction band electrons must be greater than the number of valence band electrons. This state is known as population inversion. Electrons are electronically pumped from the valence band to the conduction band to achieve a population inversion by applying a current to the active region. This increases the carrier density until the gain sufficient for one or more cavity modes to satisfy Equation 2.3 at which point threshold is reached. The injected current at this point is the 'threshold current' I_{th}. The increase in carrier density is given by:

$$G_{gen} = \frac{\nu_i I}{qV} \tag{2.6}$$

where G_{gen} is the rate of carrier generation, I is the applied current, ν_i is the injection efficiency (the fraction of the applied current that enters the active region) and V is the volume of the active region.
While carrier density is being increased due to the injected current, density is also lost due to the previously described recombination events. The total rate of recombination R_{rec} is given by:

$$R_{rec} = R_l + R_{sp} + R_A + R_{stim} \tag{2.7}$$

or in terms of the carrier density:

$$R_{rec} = AN + BN^2 + CN^3 + R_{stim} \tag{2.8}$$

where A and C are the coefficients related to the leakage and Auger recombination, respectively. The net rate of change of carrier density $\frac{dN}{dt}$ is then the generation rate minus the recombination rate:

$$\frac{dN}{dt} = \frac{\nu_i I}{qV} - AN - BN^2 - CN^3 - R_{stim} \tag{2.9}$$

At steady state operation, the system will reach an equilibrium where the carrier density does not change. i.e. $\frac{dN}{dt} = 0$. Figure 2.7 shows a schematic of the behaviour of a laser diode as the injected current is increased. The graph of the output power P_{out} of the light versus the current I is also known as the light-current or LI characteristic. The slope of the linear section after threshold has been reached ($\frac{\Delta P}{\Delta I}$) is known as the slope efficiency and is a measure of the performance of the laser.

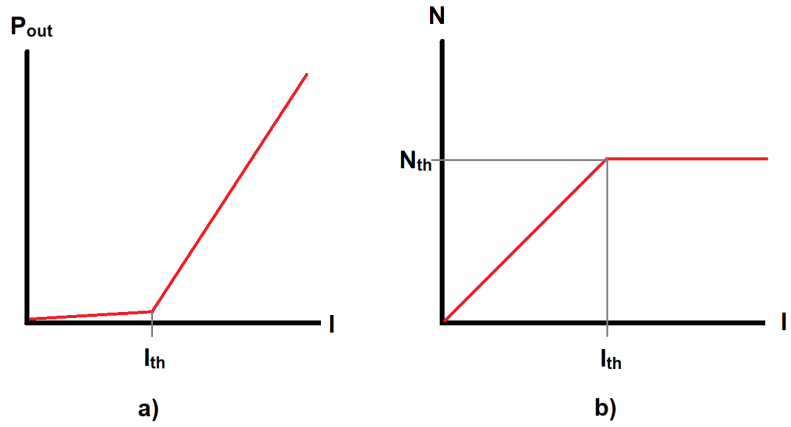

FIGURE 2.7: *a) Schematic of output power vs injected current. b) Schematic of corresponding carrier density vs injected current.*

Below the lasing threshold, spontaneous emission is the dominant photon generating process. The carrier density within the active region increases with the current injected into the cavity. Once the threshold is reached, the carrier density becomes fixed at the threshold density N_{th} and the output power begins to increase linearly as further carriers injected into the device will result in stimulated emission.

2.4 Semiconductor Lasers Based on Slots

2.4.1 Gratings

The spacing of cavity modes in a 400 μm Fabry-Pérot laser cavity is approximately 1 nm, with longer cavities resulting in an even smaller mode spacing. The gain spectrum of the materials used in these devices is on the order of 100 nm, therefore many cavity modes can attain threshold at once.
To achieve single-mode operation, one of these modes must be selected above all others. To accomplish this, a system of wavelength dependent reflectivity is incorporated. A grating is a periodic structure which is made up of a series of refractive index variations. The reflections from the grating. add up constructively for certain wavelengths defined by the Bragg condition:

$$\lambda_{Bragg} = \frac{2n_{eff}\Lambda}{m} \tag{2.10}$$

where λ_{Bragg} is the Bragg wavelength, Λ is the grating period and m is the grating order (an integer). When the Bragg condition is achieved, the cavity will undergo lasing at the Bragg wavelength.

Examples of grating structures are illustrated in Figure 2.8.

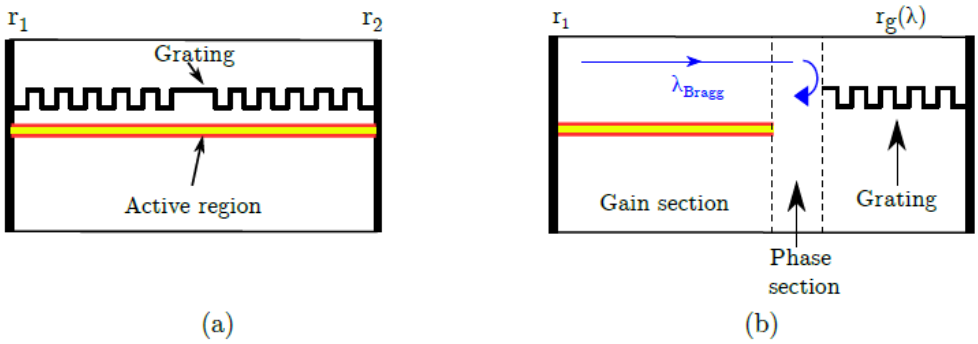

FIGURE 2.8: *Longitudinal cross-section of: a) Distributed feedback laser. b) Distributed Bragg reflector laser.*

A distributed feedback laser (DFB) is comprised of a grating which spans the entire active region, allowing only the wavelength which satisfies the Bragg condition to reach threshold. A distributed Bragg reflector (DBR) laser utilises a grating as one of the mirrors, resulting in maximum reflection of the wavelength that satisfies the Bragg condition. Both of these designs involve a grating section of low order ($m = 1$ or $m = 2$) which is buried within the structure. This requires precise, high-resolution lithography to create the grating followed by multiple regrowth steps. This is both difficult and costly to fabricate. The lasers used in our group instead consist of high-order (m»1) surface-etched slots which are much easier and less costly to fabricate.
A 2-dimensional cross-section of the ridge waveguide structure of a surface-slotted laser is shown in Fig. 2.9.

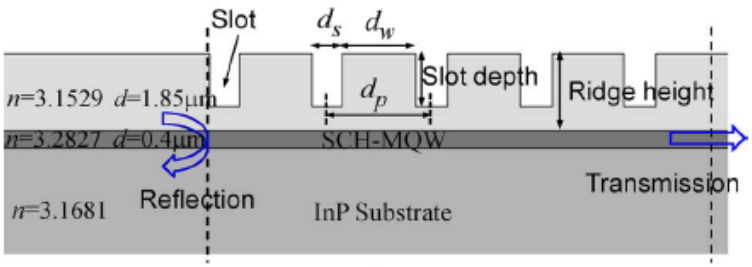

FIGURE 2.9: *2-D waveguide structure featuring slots used to form the laser grating.*

The width of each slot is approximately 1.1 μm, therefore standard photolithography can potentially be used for fabrication and, as the slots are etched into the surface of the device, there is no need for a regrowth step. This reduces the complexity of manufacture and increases the device yield.

2.4.2 Slot Parameters

In order to achieve the best performance from each device, the slot parameters such as the slot width (d_w), slot spacing (d_s), slot depth and the number of slots must be optimised to provide sufficient reflection. The grating period Λ is given by:

$$\Lambda = \Lambda_w + \Lambda_s \tag{2.11}$$

where Λ_w is the slot width and Λ_s is the slot spacing. The width and spacing are chosen to satisfy:

$$\Lambda_w = (m_w)\frac{\lambda_{Bragg}}{2n_w}\Lambda_s = (m_s)\frac{\lambda_{Bragg}}{2n_s} \tag{2.12}$$

where m_w and m_s are the slot width order and slot spacing order, respectively and are given by multiples of half-integers. m_w and m_s are the refractive indices of the slotted and unslotted waveguide, respectively. Higher-order periods result in a narrowing of the free spectral range (FSR), which is the difference between successive wavelengths that satisfy the Bragg condition for a given grating. The FSR $\Delta\lambda$ is given by:

$$\Delta\lambda = \frac{\lambda^2}{2n_g\Lambda} \tag{2.13}$$

where n_g is the group refractive index. For a grating order of 37, the FSR is approximately 40 nm. This means that there are three Bragg wavelength peaks that overlap with the gain curve of the material. This could result in a wavelength peak other than the one intended reaching threshold as the temperature changes and the gain curve shifts. This is known as a mode-hop and the gratings parameters are carefully chosen to minimise this issue.
The 2-dimensional scattering matrix method (2D-SMM) is employed to model the effect of a specific grating geometry on the reflectivity and transmission of the slots [31]. The optimum parameters were determined by analysing the grating using the 2D-SMM with varying slot parameters and the simulations were performed using the time-domain transfer matrix method (TDTMM) outlined in [32]. An open source python library called CAvity Modelling FRamework (CAMFR) was used to implement the 2D-SMM.
This method is based on eigenmode expansion and the use of scattering matrices to relate the inward a and outward b propagating waves. A representation of a scattering matrix is given in 2.10.

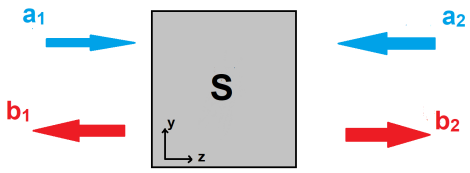

FIGURE 2.10: *Representation of a scattering matrix junction with inward and outward propagating waves.*

The outward propagating field can be related to the inward propagating field via a scattering matrix:

$$\begin{bmatrix} b_1 \\ b_2 \end{bmatrix} = \begin{bmatrix} S_{11} & S_{12} \\ S_{21} & S_{22} \end{bmatrix} \begin{bmatrix} a_1 \\ a_2 \end{bmatrix} \tag{2.14}$$

where S_{ij} are the scattering coefficients. Their physical significance is that S_{11} and S_{22} represent reflection while S_{12} and S_{21} represent transmission. The 2-dimensional electric field can be expressed as the sum of eigenmode solutions:

$$\mathbf{E}(y,z) = \mathbf{E}(y)e^{i\tilde{\beta}z} = \sum_{k}^{\infty}(a_k e^{i\tilde{\beta}_k z} + (b_k e^{-i\tilde{\beta}_k z})\mathbf{E}(y) \tag{2.15}$$

where $\tilde{\beta}$ is the complex propagation constant. This technique is outlined in [33]. A genetic algorithm has been developed in our group to improve the optimisation process [34]. The slot parameters are varied and the modelled output is evaluated to determine the best grating design. Using this data, the arrays are designed such that they span a broad range of wavelengths within the O-band and C-band, with a typical difference of 3 nm between neighbouring devices on the array. This is achieved by varying the periodicity of the slots in the grating section in order to change the centre wavelength. This optimisation work has been performed with WDM applications in mind. As such, parameters which are less relevant to comb generation such as the wavelength tunability range were prioritised. Future optimisation work for laser arrays designed as pump sources will therefore focus on parameters such as noise and wavelength stability which are vital for ensuring stable and reliable generation of frequency combs.

2.4.3 Device Structure

A schematic of a semiconductor laser based on slots is shown in Figure 2.11.

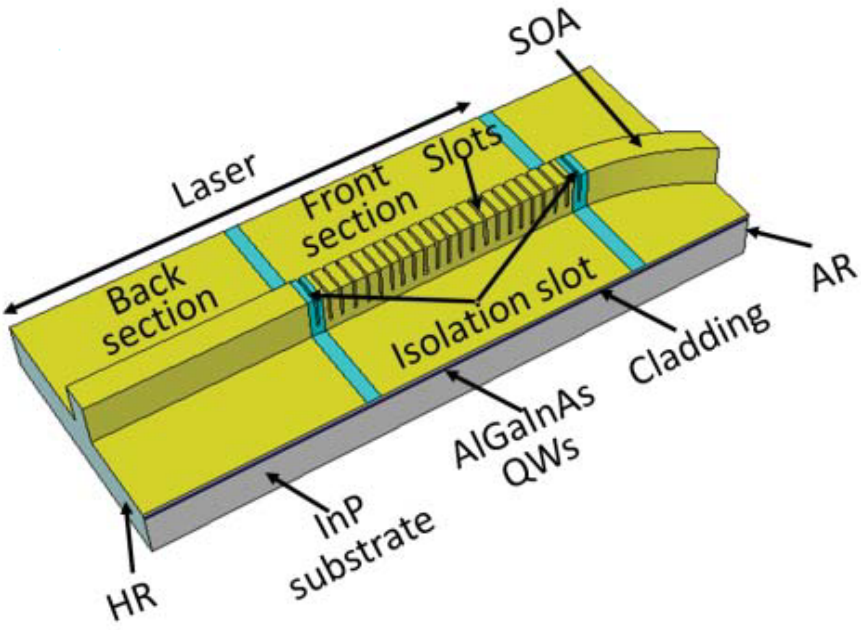

FIGURE 2.11: *Schematic structure of the slotted single-mode laser.*

The active layer consists of five compressively strained AlGaInAs quantum wells with a well thickness of 0.006 μm. Each laser consists of a 2.0 μm-wide surface ridge waveguide with three electrically isolated sections: the front SOA section, the middle grating section consists of a number of etched slots and the back gain section consisting of an active waveguide. Figure 2.12 shows a fabricated array of 12 such lasers with a 200 μm long SOA section (which is curved at a 7^o angle to reduce reflections from the front facet), and a gain and grating section with a combined length of 400 μm. An anti-reflection (AR) coating and high reflection (HR) coating are applied on the front and back facets, respectively.

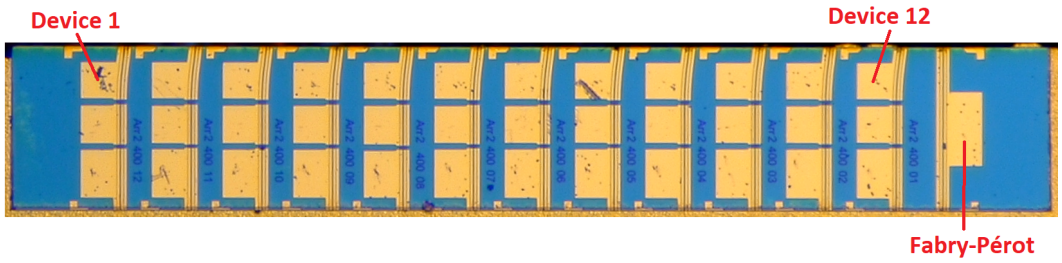

FIGURE 2.12: *12-channel slotted laser array.*

E-beam lithography was used to pattern the slots for this fabrication run due to limitations in the external foundry. Two steps of inductively coupled plasma (ICP) based dry etching with Cl_2 /N_2 gas combinations were used to form the ridge and the slots. First a shallow ridge was formed with the slot area being protected by SiO_2 during the dry etching. Afterwards the protection layer was removed and a second dry etching was used to form the slots

and also to etch the ridge to a depth of 1.3 μm. The ridge was then passivated and metal contacted to finish the laser structure. Finally, the laser bars were cleaved and mounted on aluminium nitride carriers.

2.5 Wavelength Tuning of Semiconductor Lasers

The output wavelength can be tuned by a controlled change in the refractive index of the laser. We can see from Equation 2.10 that the selected wavelength is dependent on the effective index. The wavelength change is described by:

$$\Delta\lambda = \Delta n \frac{\lambda}{n_{g,eff}} \tag{2.16}$$

where $n_{g,eff}$ is the effective group index [35]. This change in index is achieved by applying current to different sections of the device. Their tuning mechanism depends on whether the section of the laser provides optical gain (active tuning) or does not provide optical gain (passive tuning).

The **free-carrier plasma effect** changes the refractive index due to the injection of electron-hole plasma into the semiconductor material. This reduces the refractive index due to the polarization of the free carriers [36]. The index is reduced proportionally to the carrier density, blue-shifting the wavelength. A disadvantage of this is the Joule heating as a result of carrier injection, which limits the change in refractive index. The maximum refractive index change for this type of tuning is -0.04 [37].

The **thermal tuning effect** is widely used for single-mode lasers. This changes the refractive index of the material, but also the band gap energy and Fermi distribution is dependent on temperature. Therefore, a change in temperature changes the gain peak of the active medium. An increase in the device temperature using a heating block will red-shift the gain spectrum, thereby red-shifting the output wavelength. When current is supplied, the temperature is increased due to Joule heating though the temperature can also be controlled using a cooling block or heating element. The change in refractive index with temperature, known as the thermo-optic coefficient, is determined by the linear thermal expansion coefficient as well as the change in band-gap energy [38]. This can be expressed as:

$$\frac{dn}{dT} = \frac{n^2 - 1}{2n}\left[-3\alpha - \frac{1}{E_g}\frac{dE_g}{dT}\right] \tag{2.17}$$

where α is the linear thermal expansion coefficient. For single-mode DFB and DBR lasers, an increase in temperature of 1 ^0C will result in a 0.1 nm red-shift in the wavelength of the cavity and Bragg modes [39]. Wavelength tuning is essential for use of these lasers as pump sources for comb generation in microresonators where we need to precisely tune the wavelength onto

the cavity resonance and to maintain the pumping process as the power increases within the microresonator.

There are three main schemes for wavelength tuning illustrated in Figure 2.13, continuous, discontinuous and quasi-continuous.

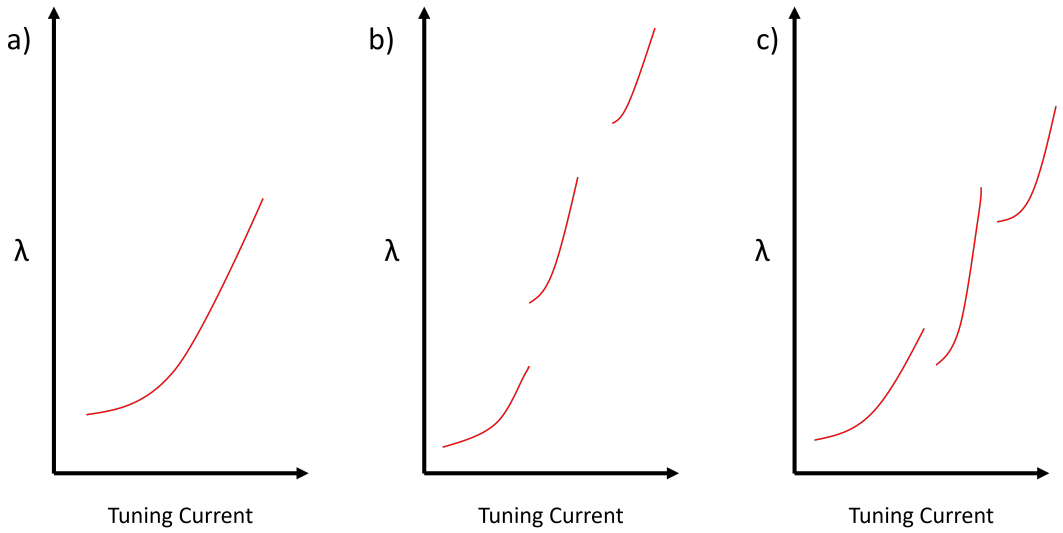

FIGURE 2.13: *Wavelength tuning schemes: a) continuous tuning, b) discontinuous tuning, c) quasi-continuous tuning.*

Continuous tuning (Figure 2.13 a)) is where the tuning current is swept and the wavelength is tuned continuously. There are no interruptions and every wavelength value in the interval between the starting and stopping wavelength is attainable. As the longitudinal modes occur at discrete wavelengths, this scheme is typically only possible over small ranges. **Discontinuous tuning** (Figure 2.13 b)) occurs when there discontinuities over the tuning range, this often results in gaps where certain wavelength values are not attainable. Each segment of this tuning range corresponds to a different cavity mode and this is therefore referred to as mode-hopping. **Quasi-continuous tuning** (Figure 2.13 c)) is a special case of discontinuous tuning where there is mode-hopping between cavity modes but there is overlap in the wavelengths covered by these cavity modes. As a result, every value of wavelength in the range is accessible.

2.6 Hybrid Square-Rectangular Lasers (HSRLs)

The Hybrid Square-Rectangular Lasers (HSRLs) consist of a square microcavity that is butt-coupled to a linear output waveguide. A Fabry-Pérot cavity is formed by cleaving the waveguide at a length of 300 μm, much longer than the side length of the microsquare. A schematic is seen in Figure 2.14.

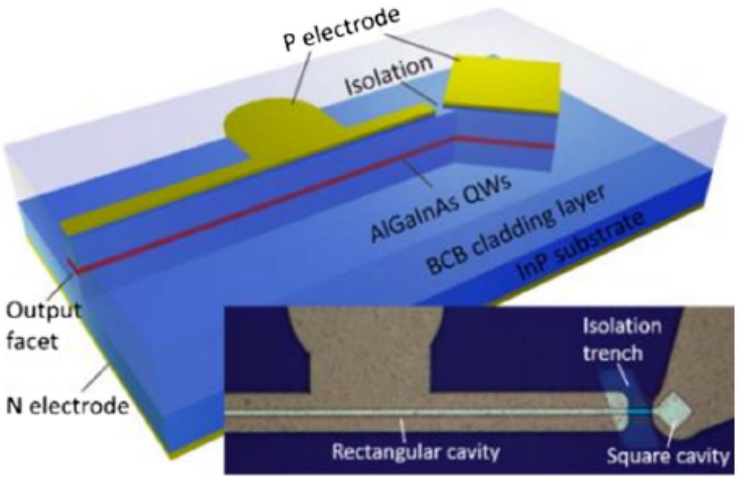

FIGURE 2.14: *Schematic and microscopic image of an HSRL [40]. Square and rectangular sections are electrically isolated by a 20 µm isolation trench.*

Mode coupling between the whispering-gallery modes (WGM) in the square microcavity and the longitudinal modes in the FP cavity allows for dual - mode lasing. The high Q-factor and compact size of WGM microcavity lasers such as these makes them highly suitable for use in photonic integrated circuits. Dual-mode lasers in particular are useful for photonic generation of microwaves using heterodyne mixing due to the advantage of their higher signal frequency, compact structure, and being free of electromagnetic interference.

2.7 Noise in Semiconductor Lasers

The Schawlow-Townes equation was developed even before a laser was experimentally demonstrated and calculates the fundament limit of the linewidth of a laser [41]:

$$\Delta\nu_{laser} = \frac{4\pi h\nu(\nu_0)^2}{P_{out}} \tag{2.18}$$

where $\Delta\nu_{laser}$ is the Schawlow-Townes linewidth, hν is the photon energy, ν_0 is the half-width of the resonance at half-maximum intensity, and P_{out} is the output power.
This was later modified by Lax [42] and verified for the He-Ne laser [43]. However, the linewidth measured for semiconductor lasers is many times greater than that predicted by the Schawlow-Townes equation.

The width of spectral lines is due to phase fluctuations in the optical field, caused by spontaneous emission events. These events alter the phase and intensity of the optical field as shown in the phasor model in Figure 2.15.

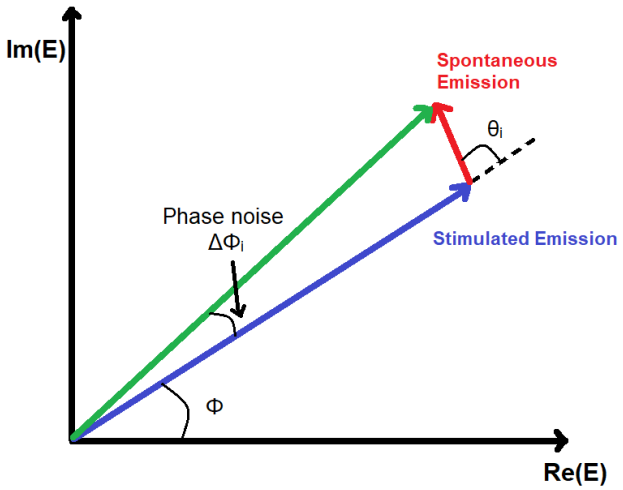

FIGURE 2.15: *Phasor model demonstrating effect of spontaneous emission on optical field.*

In addition to the instantaneous phase change brought about by spontaneous emission, a delayed phase change occurs as the laser undergoes relaxation oscillations to restore the steady-state field intensity. A change in carrier density results in a deviation of the imaginary and real refractive indices from their steady-state value. A change in the refractive index results in additional phase shifts in the optical field and causes line broadening.
Henry [44] considered the ratio of the deviation of the real refractive index (n') and the deviation of the imaginary refractive index (n''):

$$\alpha = \frac{\Delta n'}{\Delta n''} \tag{2.19}$$

and went on to show that the coupling of phase noise to intensity fluctuations leads to an increase in the laser linewidth by a factor of $(1+\alpha^2)$, where α is referred to as the 'linewidth enhancement factor. The laser linewidth, defined as the full width at half maximum (FWHM) of the optical spectral line, is an important parameter as it is a measure of the coherence of the laser light. Therefore, a narrow linewidth is desirable for many applications in optical communications. More relevant to this work, it has been found that reliable soliton generation in microresonators requires the linewidth of the pump laser to be narrower than the microresonator mode bandwidth [45] and also that the soliton comb lines inherit the linewidth of the pump laser [46].
The linewidth of semiconductor lasers is inversely proportional to the cavity length [47]. This is because as the cavity length increases, the threshold carrier density decreases. This reduces the spontaneous emission rate and, therefore, the linewidth. Our group has previously demonstrated a significant reduction in the linewidth of our slotted lasers by increasing the cavity length, with a 1 mm long device being recorded with a linewidth of less than 1 MHz [48].

Chapter 3

Characterisation of Semiconductor Lasers

3.1 Slotted Laser Arrays

Semiconductor laser arrays consist of a number of individual devices electrically isolated from each other on the same chip. Our group has previously designed and characterised arrays consisting of 9 devices [49], 10 devices [50] and 12 devices [23] with wavelengths in the C-band. Such arrays are designed for optical communications, particularly wavelength division multiplexing (WDM), which is illustrated in Figure 3.1.

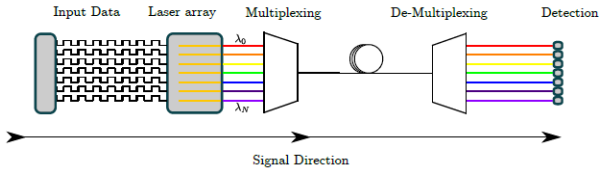

FIGURE 3.1: *Schematic demonstrating the principal of wavelength division multiplexing.*

WDM allows for high-speed data transfer as multiple signals at differing wavelengths can be sent simultaneously through a single fibre and then separated out at the receiver. An array of lasers can transmit through multiple wavelength channels at once, and the wide tunability of semiconductor lasers means that a wide range of WDM wavelength channels can be accessed. Arrays are therefore designed such that the possible output wavelengths of each device of the array yield a continuous tuning spectrum over a wide wavelength range.
Three 12-channel arrays with wavelengths covering the O-band were characterised. The centre wavelengths of the devices are determined by the slot parameters and are designed with the aid of simulations to be linearly spaced across the O-band. The arrays are all from the same fabrication run but differ in the number and period of their slots. Array 1 consists of slots of a single period and there are many slots (between 47 and 90) while Array 3 also consists of slots of a single period but with fewer slots (between 16 and 33). Array 2 consists of ten slots of three different periods for a total of 30 slots. It was previously shown in our characterisation of the nine-channel array [49]

that temperature tuning caused mode competition, reducing SMSR. With a FSR of 37 nm, there were 3 reflection peaks in the range of 1500 nm to 1600 nm, and the shifting of the gain peak with temperature led to other modes experiencing gain. To counteract this effect, arrays based on non-uniformly spaced slots, outlined in [23], were developed. The different slot periods each have their own associated FSR and it is therefore possible to choose these periods such that the reflection peaks associated with each period add up constructively at the desired wavelength while interfering destructively elsewhere. The optimal parameters are chosen by simulating the reflection spectra using SMM and choosing the parameters that best suppress the undesired peaks. Figure 3.2 shows such a simulation previously performed by our group to illustrate this concept [51].

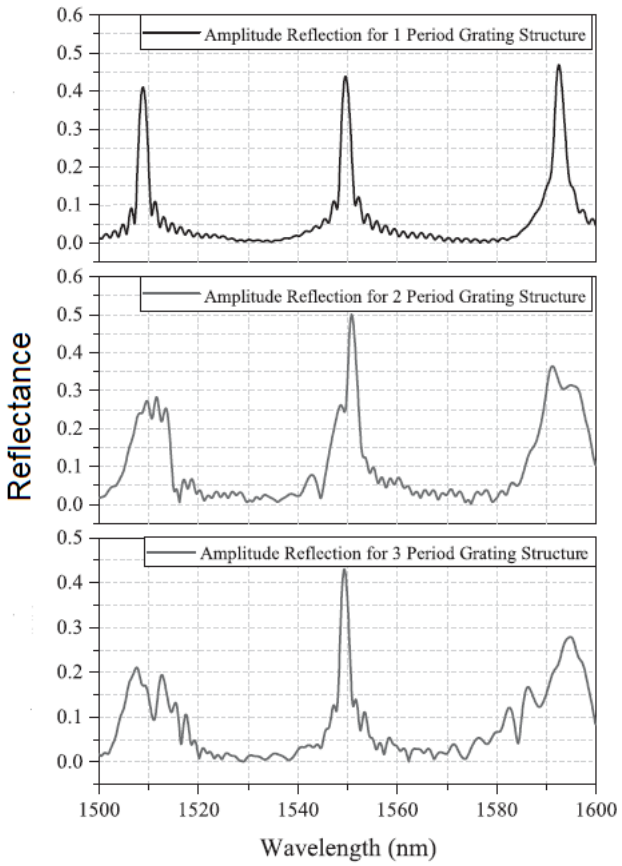

FIGURE 3.2: *Simulated reflection spectrum of one, two and three period grating structures.*

The reflection spectra of a single-period grating shows three clear peaks separated by one FSR. The incorporation of a two-period and three-period grating is seen to reinforce the central reflection peak while suppressing the adjacent reflection peaks. Though the reduction of the side-peaks is only by a factor of two, the resulting characterisation of these devices showed an improvement in SMSR and a reduction in mode-hopping while the device was thermally tuned.

The period, number of slots and design wavelength for each device is shown in 3.1. The total length of the grating plus gain section of each device is 400 μm and the SOA section is 200 μm long.

	Array 1			Array 2					Array 3			
	Period (um)	#of slots			Period1	Period2	Period3	#of slots		Period (um)	#of slots	Wavelength (nm)
Device 1	2.772	90		Device 1	4.752	5.346	5.940	[10, 10, 10]	Device 1	5.148	33	1280.0
Device 2	2.780	90		Device 2	4.766	5.361	5.957	[10, 10, 10]	Device 2	5.163	33	1283.6
Device 3	2.773	90		Device 3	4.779	5.377	5.974	[10, 10, 10]	Device 3	5.178	33	1287.3
Device 4	2.796	90		Device 4	4.793	5.392	5.991	[10, 10, 10]	Device 4	5.192	33	1290.9
Device 5	2.804	62		Device 5	4.807	5.407	6.008	[10, 10, 10]	Device 5	5.207	33	1294.5
Device 6	2.410	65		Device 6	4.820	5.423	6.025	[10, 10, 10]	Device 6	6.025	23	1298.2
Device 7	3.021	62		Device 7	4.834	5.438	6.042	[10, 10, 10]	Device 7	7.855	19	1301.8
Device 8	3.434	55		Device 8	4.848	5.454	6.060	[10, 10, 10]	Device 8	6.867	20	1305.5
Device 9	4.051	47		Device 9	4.861	5.469	6.077	[10, 10, 10]	Device 9	7.697	17	1309.1
Device 10	2.437	69		Device 10	4.875	5.484	6.094	[10, 10, 10]	Device 10	6.703	18	1312.7
Device 11	2.852	63		Device 11	4.889	5.500	6.111	[10, 10, 10]	Device 11	5.907	16	1316.4
Device 12	3.064	76		Device 12	4.902	5.515	6.128	[10, 10, 10]	Device 12	5.924	16	1320.0

TABLE 3.1: Parameters of the 12-channel arrays.

The devices were mounted on a copper heat sink and the temperature was controlled using a thermo-electric cooler (TEC). A current of 10 mA was injected into the SOA to ensure the section is biased at transparency. This is the current density where the net gain provided by that section is equal to zero and becomes "transparent". The devices were fibre-coupled to an Agilent 86140B optical spectrum analyser (OSA) with a resolution of 0.06 nm and a sensitivity of -70 dBm. A diagram of this setup is seen in Figure 3.3.

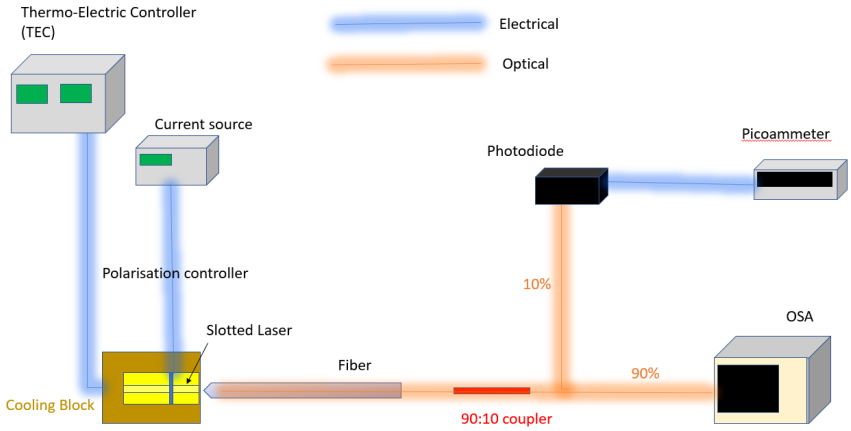

FIGURE 3.3: *Experimental setup for characterisation of laser arrays. The ambient temperature of the laser under investigation is controlled by a thermo-electric cooler while the injected current is supplied by a current source. The output light is collected by a lensed fibre and 10% of the light is sent to a photodiode in order to aid with coupling. The remaining 90% is analysed with an optical spectrum analyser.*

3.1.1 L-I Characteristic

The L-I (Light-Current) characteristic was performed by sweeping the current and measuring the output power using a bare photodiode, rather than the fibre, connected directly to the picoammeter. The photodiode response is calibrated with a tunable laser of known output power in order to determine

the optical power from the recorded photocurrent. The L-I characteristic for each of the arrays is shown in 3.4.

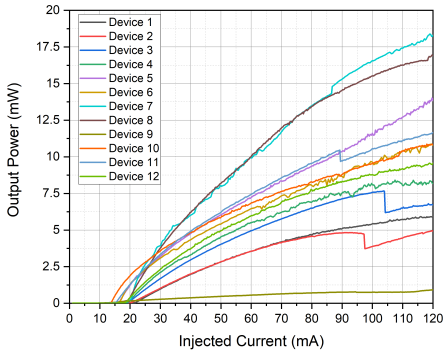

(a) *Array 1 L-I characteristic.*

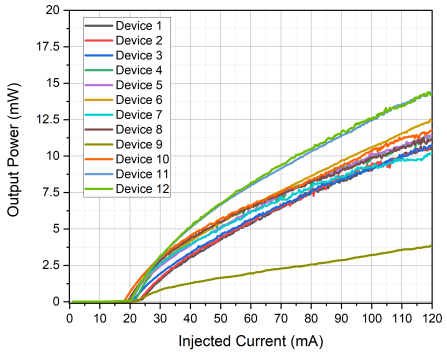

(b) *Array 2 L-I characteristic.*

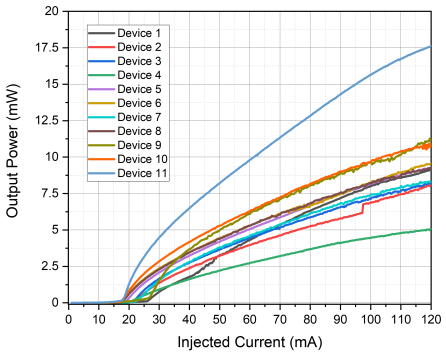

(c) *Array 3 L-I characteristic.*

FIGURE 3.4: L-I characterisation of the arrays at 20 ^{o}C with 10 mA injected into the SOA section.

The threshold current was found to vary from 16 mA to 25 mA for all devices. Device 9 on Array 1 and Array 2, and Device 4 of Array 3 array were found to emit significantly lower output power than the rest of the devices on that array. This is likely due to damage such as defects on the facets when cleaving or an error during fabrication. Apart from these outliers, the devices an Arrays 2 and 3, where the number of slots does not vary significantly, show a generally consistent behaviour. Array 1, where the number of slots very significantly between devices, has much less consistent behaviour.

3.1.2 Output Spectra

The output spectra of all devices in each array at 20 ^{o}C is presented in Figure 3.5.

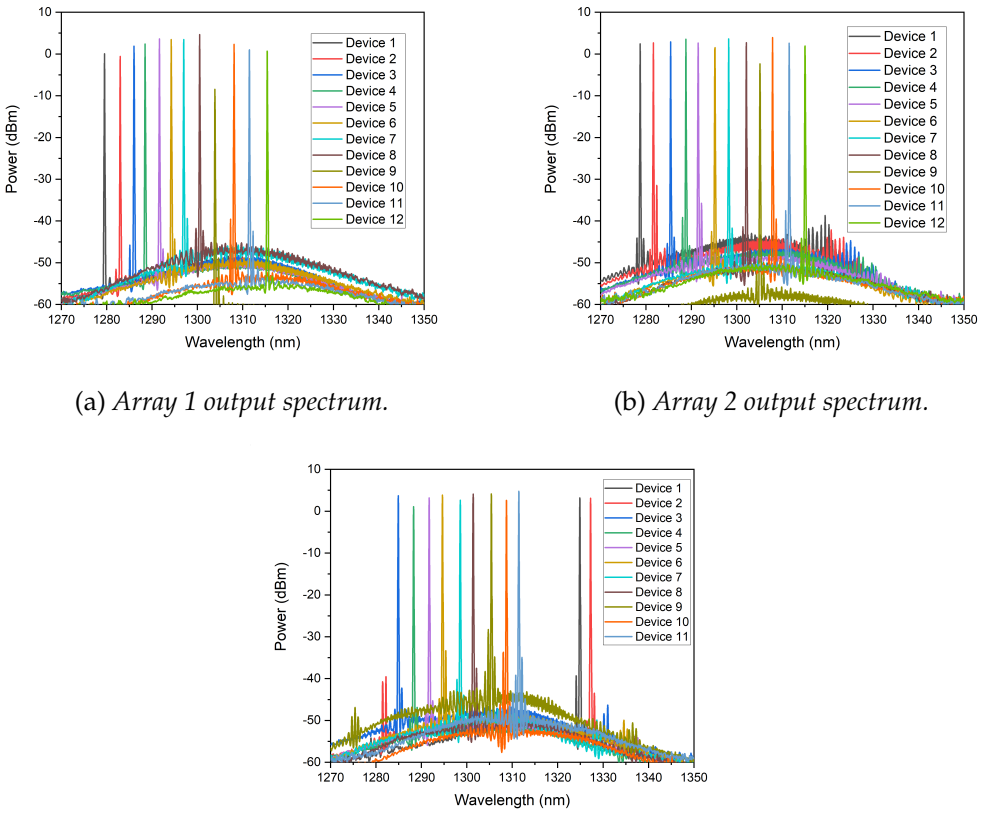

(a) *Array 1 output spectrum.*

(b) *Array 2 output spectrum.*

(c) *Array 3 output spectrum.*

FIGURE 3.5: *Output spectrum recorded at 20 ^{o}C with 100 mA injection current, SOA = 10 mA.*

The average spacing between modes is approximately 3.3 nm in each array. It was noticed that Devices 1 and 2 of Array 3 emit in the region of 1324 nm and 1327 nm, which is not the intended wavelength. These devices were designed to emit a wavelength of approximately 1280 nm and 1283 nm, respectively. The free spectral range (FSR) of a high-order grating with a slot spacing of 5.15 μm is approximately 47 nm, thus these devices are lasing at a mode one FSR away from the intended wavelength. The three-period devices of Array 2 emit at a wavelength close to the designed wavelength, though blue-shifted by approximately 3 nm from their design. As this was the first generation of 1.3 μm devices which have been designed and fabricated by our group, the gain and refractive index data were not precisely known at the beginning of this work and were therefore estimated from the 1550 nm devices. There is clearly room for improvement in future fabrication runs.

3.1.3 Thermal Tuning

Thermal wavelength tuning was accomplished by injecting a constant current of 100 mA split across the gain and grating sections such that the current density is equal in both sections, while increasing the temperature from 15 ^{o}C - 60 ^{o}C in 5 degree increments using the TEC. The output spectrum of each device on the arrays recorded at 5 degree increments over the temperature range are plotted together (3.6) to illustrate the wavelength tuning.

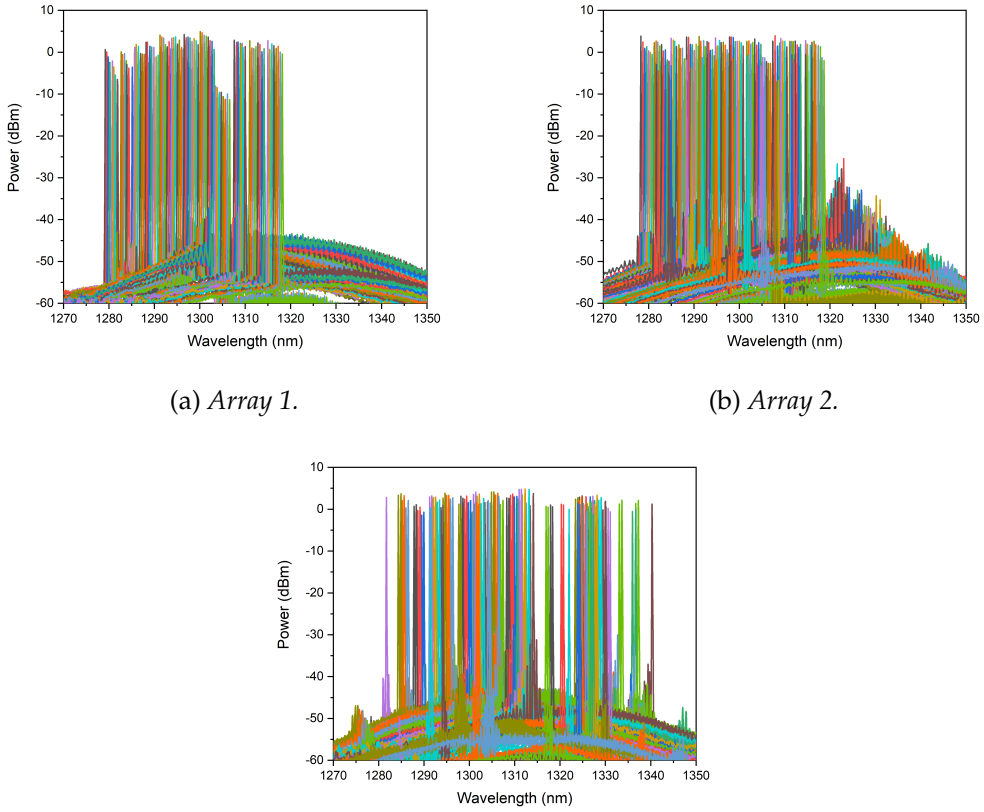

(a) *Array 1.*

(b) *Array 2.*

(c) *Array 3.*

FIGURE 3.6: *Thermal tuning spectra showing a continuous tuning range for Arrays 1 and 2. There are several clear discontinuities in the thermal tuning spectrum of Array 3 where FSR mode hopping occurred.*

The thermal tuning demonstrates a wavelength tuning range of ∼40 nm for both Array 1 and Array 2. However, there are clear discontinuities in the thermal tuning spectrum of Array 3 (Fig. 3.6c) although the range here is up to 60 nm. The plot of wavelength vs temperature for the three-period array (Fig. 3.7b) demonstrates a generally linear red-shift in wavelength of approximately 0.09 nm/^{o}C increase in temperature. In some cases, the wavelength blue-shifts with a temperature increase, due to crossing a mode boundary during tuning. Such mode hops are common in many DBR-type lasers [52]. As temperature increased, it was noticed that the wavelength of the devices

on the blue end of the array would reach a point where the emitted wavelength jumped by approximately one FSR, this occurred with 7 devices up to 60 ^{o}C. The jumps in wavelength can clearly be seen in Fig. 3.7c. Thus, there is not a continuous tuning range for the single-period array. For a majority of the devices, the SMSR is high over this tuning range, above 35 dB as seen in Fig. 3.8b. Devices 1 and 2 of this array have comparatively lower SMSR due to the competition from FSR modes in the region of 1320 nm - 1325 nm. We do not observe any jumps to the next FSR due to the suppression of these modes from the use of non-uniformly spaced slots.

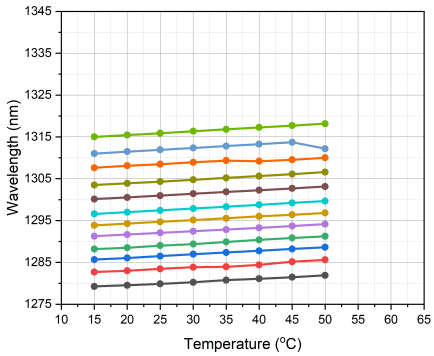

(a) *Array 1.*

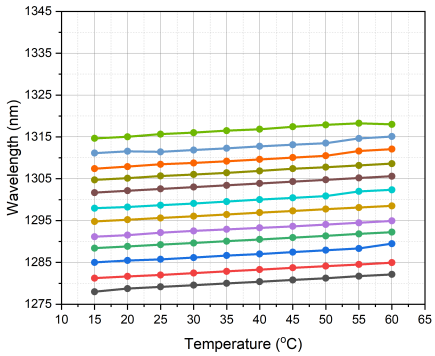

(b) *Array 2.*

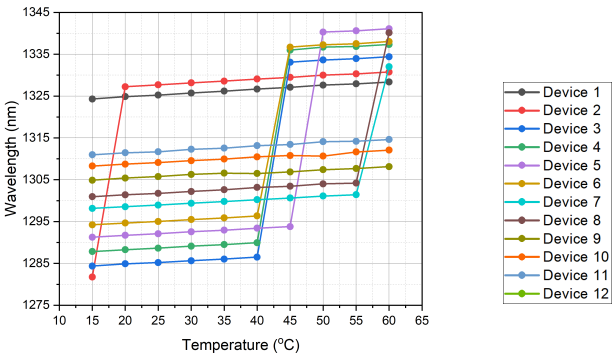

(c) *Array 3.*

FIGURE 3.7: *Wavelength vs temperature.*

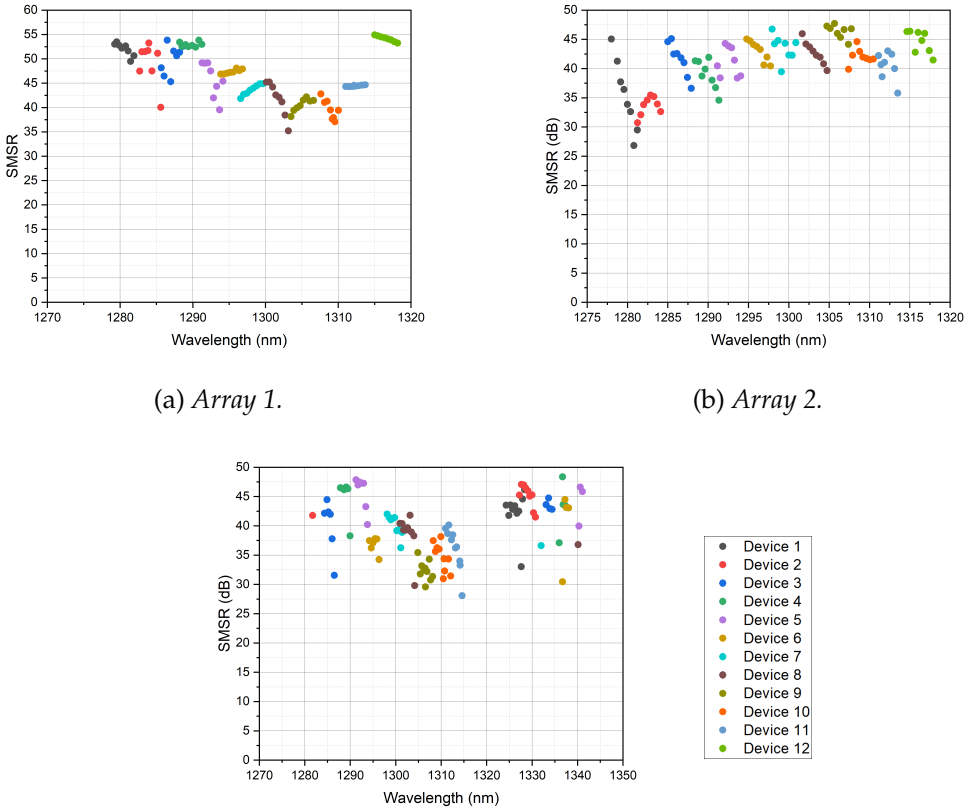

(a) *Array 1.*

(b) *Array 2.*

(c) *Array 3.*

FIGURE 3.8: *SMSR vs wavelength.*

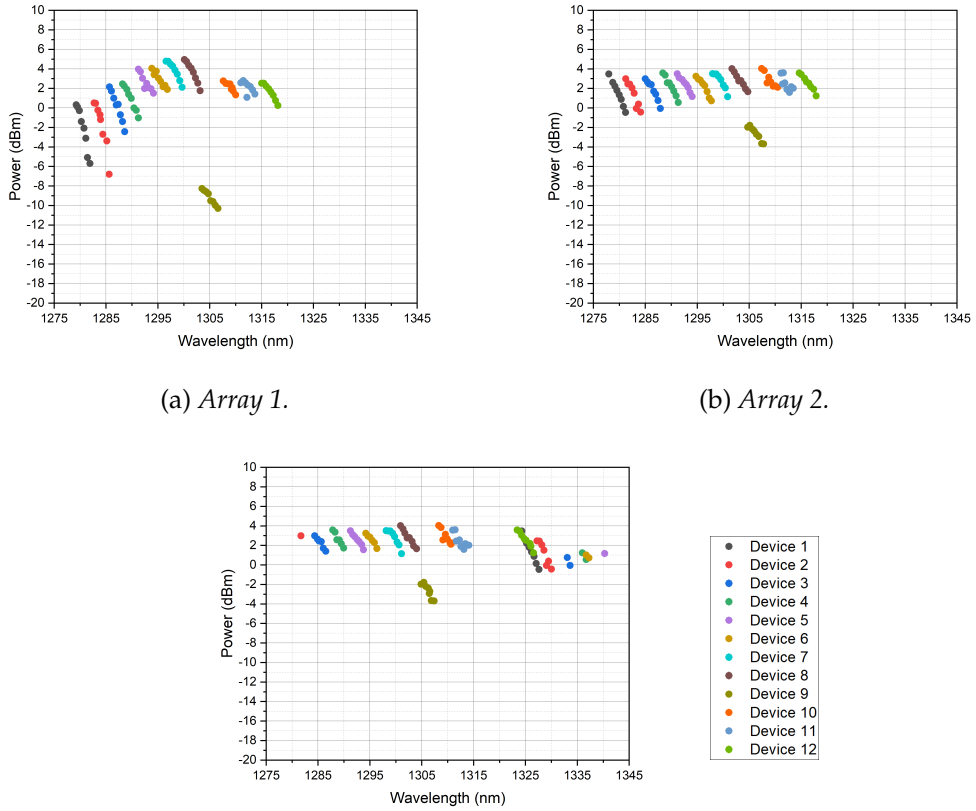

(a) *Array 1.*

(b) *Array 2.*

(c) *Array 3.*

FIGURE 3.9: *Power vs wavelength.*

The output power of each device generally decreased as temperature was increased (Figure 3.9). This is because non-radiative recombination and carrier leakage increase with temperature, reducing internal efficiency. Device 9 on both Array 1 and Array 2 produced noticeably lower output power compared to the rest of the devices on their respective arrays. There was no obvious damage on visual inspection so this may be a result of damage during fabrication.

3.1.4 SOA Characterisation

With a constant injection current of 100 mA at 20 ^{o}C, the SOA current was increased from 0 mA to 60 mA in increments of 2.5 mA. Figures 3.10, 3.12 and 3.13 show the recorded peak wavelength, SMSR and output power measured for all devices as SOA current was increased.

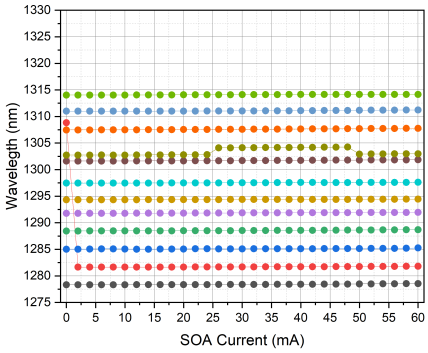

(a) *Array 1.*

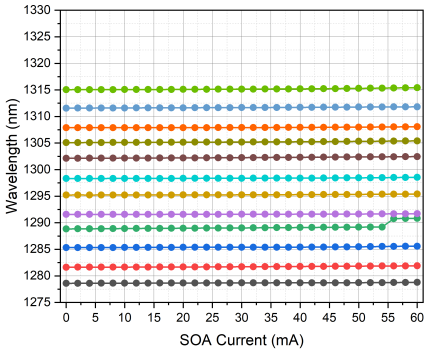

(b) *Array 2.*

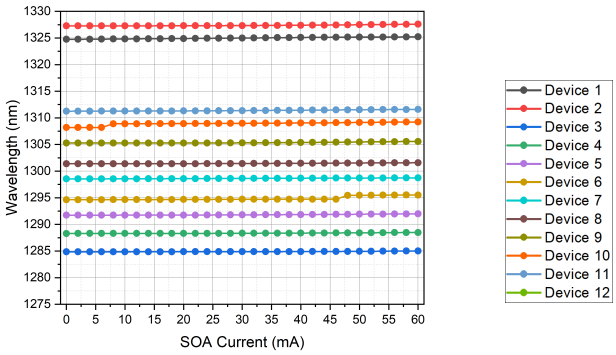

(c) *Array 3.*

FIGURE 3.10: *Wavelength vs SOA current.*

A slight red-shifting of the peak wavelength is observed with increasing SOA current and this is especially noticeable at higher SOA currents. Figure 3.11 shows the peak wavelength and SMSR recorded for Device 1 on each array as the SOA current is increased. The red-shifting of the wavelength varied between devices from a minimum of 0.15 nm to a maximum of 0.6 nm over the current range. Meaning a maximum of 0.01 nm/mA change in SOA current.

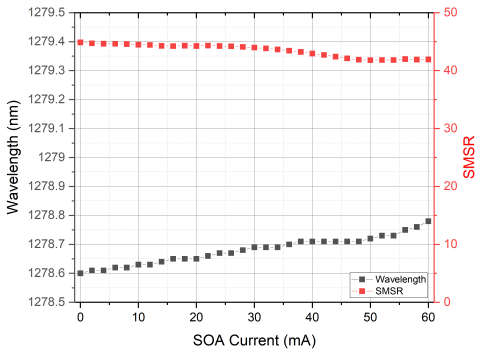

(a) *Array 2, Device 1.*

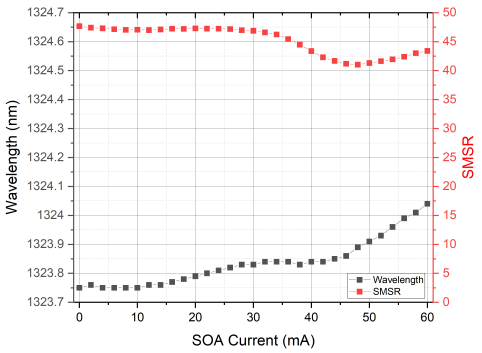

(b) *Array 3, Device 1.*

FIGURE 3.11: *SOA characterisation of single devices.*

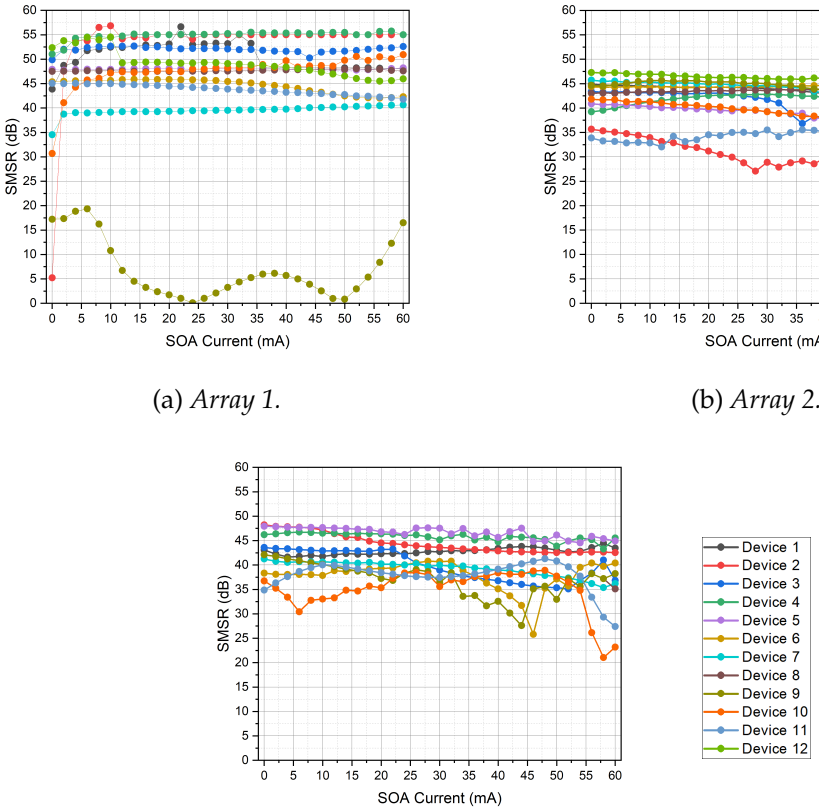

(a) *Array 1.*

(b) *Array 2.*

(c) *Array 3.*

FIGURE 3.12: *SMSR vs SOA current.*

SMSR generally remains high for most devices though it can be seen to drop sharply if a mode-hop is approached. With the exception of Device 9 of Array 1, which was damaged during the measurements when a probe destroyed the ridge, the increase in output power with SOA current is consistent for devices on the same array.

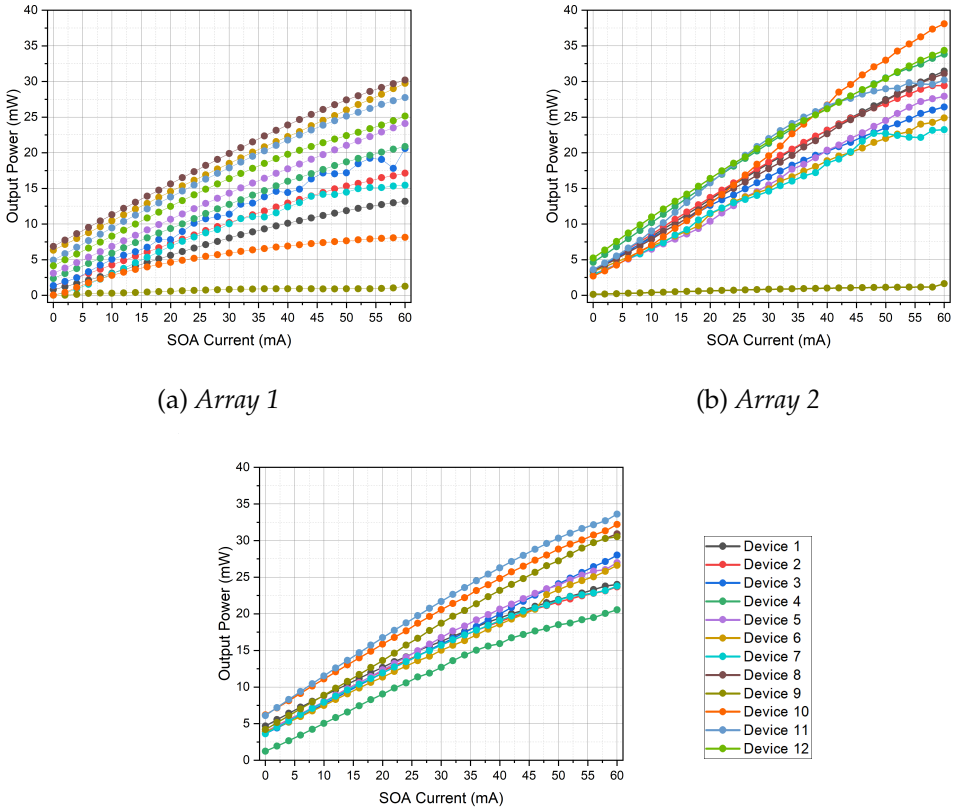

(a) *Array 1*

(b) *Array 2*

(c) *Array 3.*

FIGURE 3.13: *Output power vs SOA current.*

Output powers up to 35 mW are obtained for these devices with this simple SOA section, sufficient for applications in the O-band. An output power of at least 25 mW is achieved for many of these devices with a modest injection current into the SOA section almost double the power in some cases when compared with the values seen in the LI curves (Figure 3.4) where the SOA is only injected with enough current to bring the section to transparency. The highest output power was 38 mW for Device 10 on Array 2. These powers are still not sufficient for pumping the microresonators, which is the topic of the next two chapters, however further improvements to the integrated SOA may eliminate the need for an EDFA when pumping. Also, improving the Q factor of our resonators would allow for a pump laser with power in the tens of milliwatts to be effective in the future.

3.2 Noise Characterisation of Semiconductor Lasers

3.2.1 Laser Linewidth

As the resolution of the OSA is not sufficient to accurately determine the width of spectral lines, the spectral linewidth was measured using the delayed self-heterodyne (DS-H) method [53] as shown in Figure 3.14. The optical signal is converted to an electrical signal by splitting the beam, sending

one branch through a fibre spool to decorrelate the branches and the other branch is phase modulated. The beams are then recombined and the beat note is detected by a photodiode and then analysed with an ESA. As mentioned previously, low-noise lasers are desirable for both optical communications and pumping microresonators. It is therefore important to characterise the noise of these device to assess their suitability.

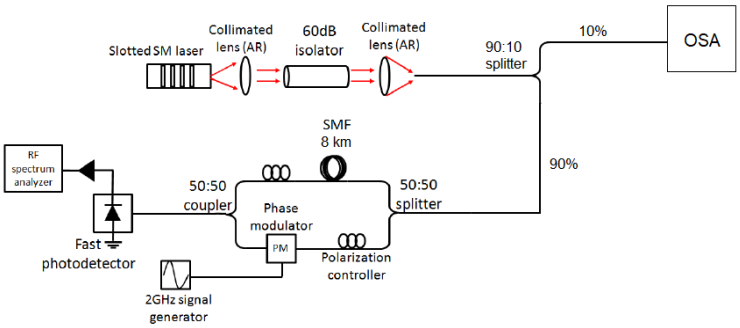

FIGURE 3.14: *Delayed self-heterodyne setup.*

Figure 3.15 shows the linewidth spectrum obtained for Device 6 of Array 2. The intrinsic linewidth of a spectral line is Lorentzian in profile while noise from equipment adds a Gaussian component to the overall shape. This results in a convolution of the Lorentzian and Gaussian shapes, known as a Voigt profile. The data was therefore fitted to a Voigt profile and a deconvolution was performed to obtain the Lorentzian full-width at half-maximum (FWHM), which corresponds to the 3 dB linewidth. The result must then be divided by a factor of 2 due to the nature of the DS-H method. The FWHM was determined to be 12.6 MHz, indicating a linewidth of 6.3 MHz.

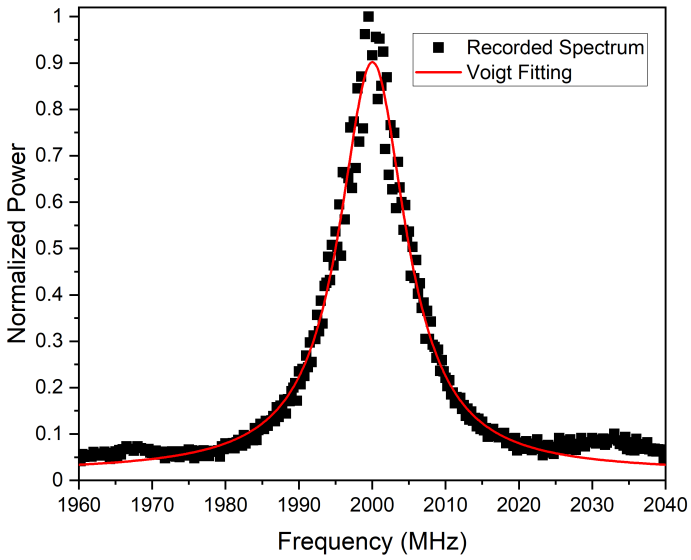

FIGURE 3.15: *Example linewidth spectrum of Array 2, Device 6.*

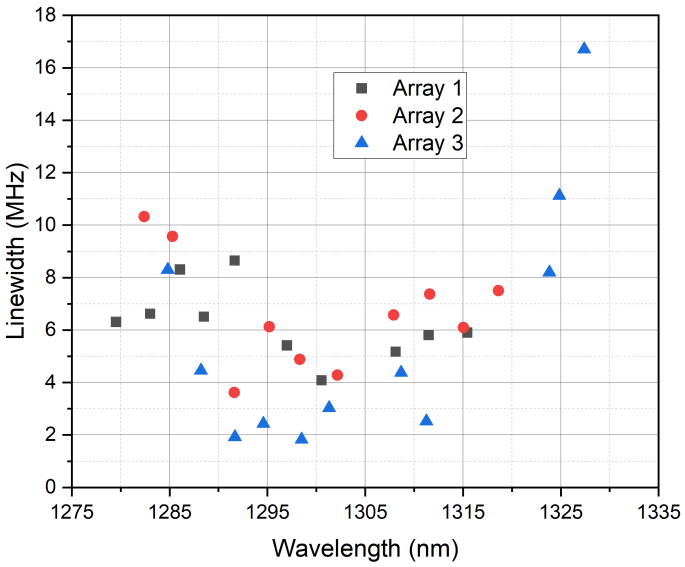

FIGURE 3.16: *Linewidth as a function of wavelength.*

We see the measured linewidth as a function of wavelength in Fig. 3.16. The linewidth enhancement factor increases as the gain peak wavelength is approached, thus we expect the devices lasing at the red end of the array to have the greatest linewidth. This is seen in Fig. 3.16 though we also see relatively large linewidth values at the blue end of the array also. There is no clear correlation between the grating design and the measured linewidth

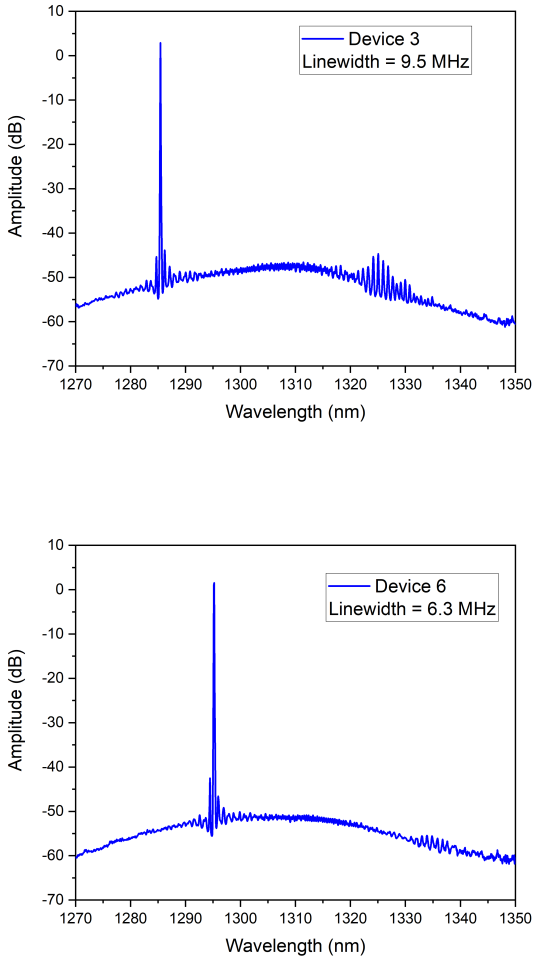

FIGURE 3.17: *(a) Optical spectrum of Device 3 of the three-period array. (b) Optical spectrum of Device 6 of the three-period array*

Figure 3.17 shows the output spectrum of Device 3, at the blue end of Array 2, compared to Device 6 which is in the centre of the same array. It can be seen that there is a significant amount of noise from 1325 nm to 1330 nm in the spectrum of Device 3 whereas this is much less prevalent in the spectrum of Device 6. This may explain why, even though the peak wavelength of Device 6 is red-shifted relative to Device 3, the measured linewidth is narrower. This trend was also observed for the linewidth of the 400 μm long devices measured in [23]. It was also shown that devices with longer cavity lengths (700 μm and 1 mm) had an overall narrower linewidth.

3.2.2 Phase Noise Measurement

The linewidth is a useful metric but does not tell the full story of the noise in the system. Low frequency or $1/f$ noise associated with the electronics as well as instantaneous fluctuations means that the intrinsic linewidth is obscured in the measured data. The measurement of the phase noise, outlined

in [54], is a much more robust measurement where the frequency modulated (FM) noise spectrum is recorded. This fully captures the noise processes contributing to the overall phase noise. This is measured using a similar DS-H setup as the linewidth measurement but the data is collected with a real-time oscilloscope (RTO) rather than an ESA (Figure 3.18. The signal was sampled at a rate of 5 Gs/s.

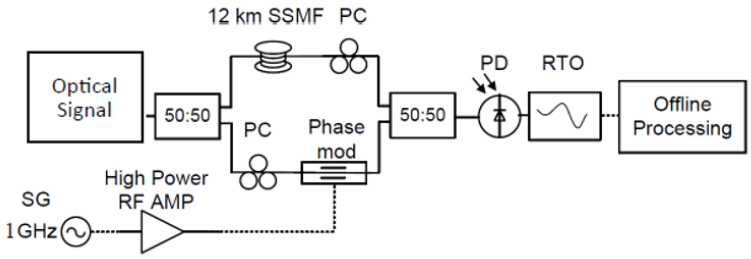

FIGURE 3.18: *Delayed self-heterodyne setup for phase noise characterisation.*

The electrical field of the light from a CW laser is given by:

$$E(t) = \sqrt{P_0 + \Delta P(t)} \times e^{i[\omega_0 t + \phi_n(t)]} \tag{3.1}$$

where $P_0 + \Delta P(t)$ is the output power at time t, ω_0 is the angular optical frequency and $\phi_n(t)$ is the phase noise. The light is split in the DS-H system with one branch undergoing a time-delay and the other branch being phase-modulated. Figure 3.19 illustrates how this alters the field in both branches.

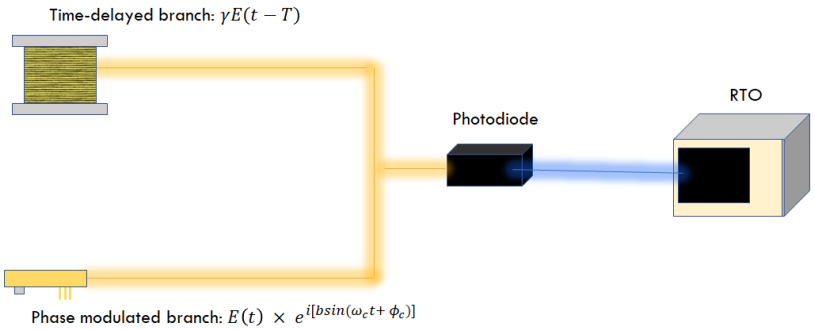

FIGURE 3.19: *Time delayed and phase-modulated branches.*

The field delayed by the fibre spool can be expressed as:

$$\gamma E(t-T) \tag{3.2}$$

where T is the time-delay caused by the fibre spool and γ is the ratio of the amplitude of optical power of each branch. The field that is phase modulated can be expressed as:

$$e^{i[b\sin(\omega_c t + \phi_c)]} \tag{3.3}$$

where b is the modulation index (a measure of the extent of modulation of the signal by the phase modulator), ω_c and ϕ_c are the modulation carrier frequency and phase of the driving signal at the modulator input.
When these two branches are recombined at the photodiode, the overall incident electrical field is given by:

$$E_i\,(t) = \frac{1}{2}[\gamma\, E(t-T) - E(t)\ \times\ e^{i[bsin(\omega_c t+\phi_c)]}] \tag{3.4}$$

The current that results when this field is incident on a photodiode with responsivity $\mathcal{R}$ is given by:

$$\begin{aligned} i_{pd}(t) = &-\frac{\gamma\mathcal{R}[P_0+\Delta P(t)]}{2} cos(\Delta\phi_n(t)+\omega_0 T)\times cos[bsin(\omega_c t+\phi_c)] \\ &+\frac{\gamma\mathcal{R}[P_0+\Delta P(t)]}{2} sin(\Delta\phi_n(t)+\omega_0 T)\times sin[bsin(\omega_c t+\phi_c)] \end{aligned} \tag{3.5}$$

where $\Delta\phi_n(t)$ is the differential phase noise. Applying Bessel coefficient expansion, the in-phase $I(t)$ and quadrature $Q(t)$ of the differential phase noise are given by:

$$I(t) = cos[\Delta\phi_n(t)+\omega_0 T] \tag{3.6}$$

$$Q(t) = sin[\Delta\phi_n(t)+\omega_0 T] \tag{3.7}$$

These can be found at even and odd harmonics of the photo-detected signal. By offline processing of the RTO signal and analysing the first and second harmonics, an FM-noise spectrum can be obtained. As we are analysing both of these harmonics to extract the phase noise, it is necessary to ensure that the amplitudes of the harmonics are approximately equal. Figure 3.20 shows a signal from a 1550 nm device that has been sufficiently modulated such that the signals at 400 MHz and 800 MHz are equal. We modulated at 400 MHz as the bandwidth of our RTO is 1 GHz.

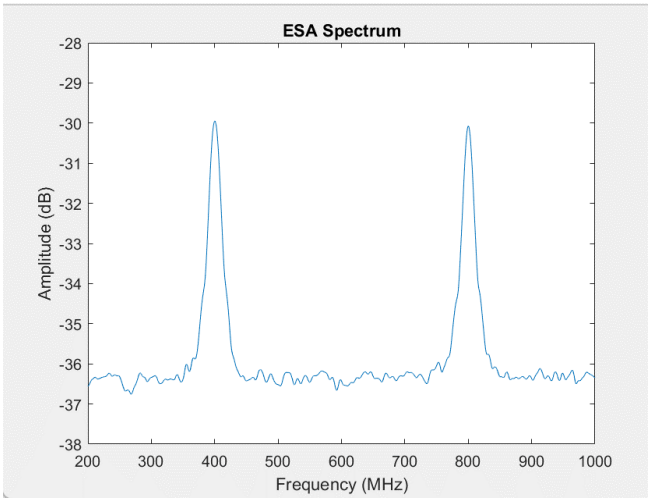

FIGURE 3.20: *Collected ESA spectrum of the first and second harmonic of a signal modulated at 400 MHz.*

The 1310 nm phase modulator proved to be insufficient to achieve parity between these harmonics and so only the simple linewidth measurement data was successfully recorded for the arrays. It was possible to record the phase noise for devices with a wavelength centred around 1550 nm. An example is shown in Figure 3.21 where a single-period device with a cavity length of 400 μm was characterised.

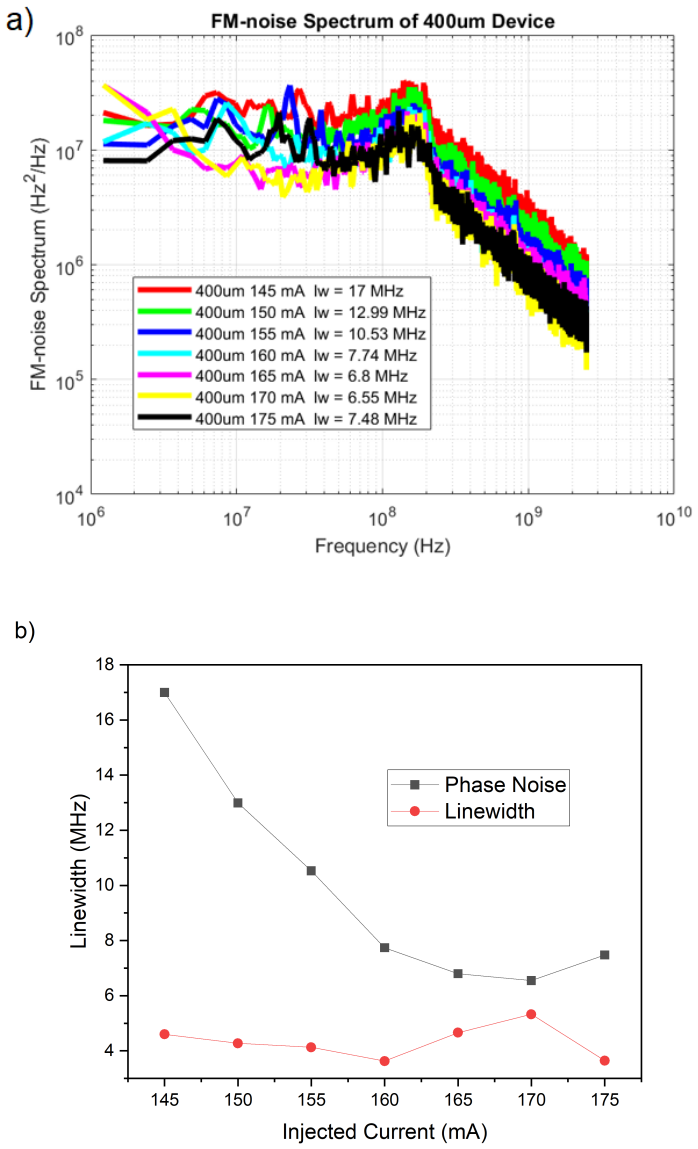

FIGURE 3.21: *a) FM-noise spectra of a 400 µm device with different injection current. b) The linewidth calculated from the flat, low-frequency region of the FM-noise spectra compared with the Lorentzian linewidth determined from the simple linewidth measurement.*

The Lorentzian linewidth can be extracted from the flat region of the FM-noise spectra [53]. The linewidth calculated from the phase noise measurement is larger than that of the simple linewidth method, though it follows

the expected trend of a decrease in linewidth with an increase in injected current. The noise of three 1550 nm devices with differing cavity lengths was also recorded 3.22.

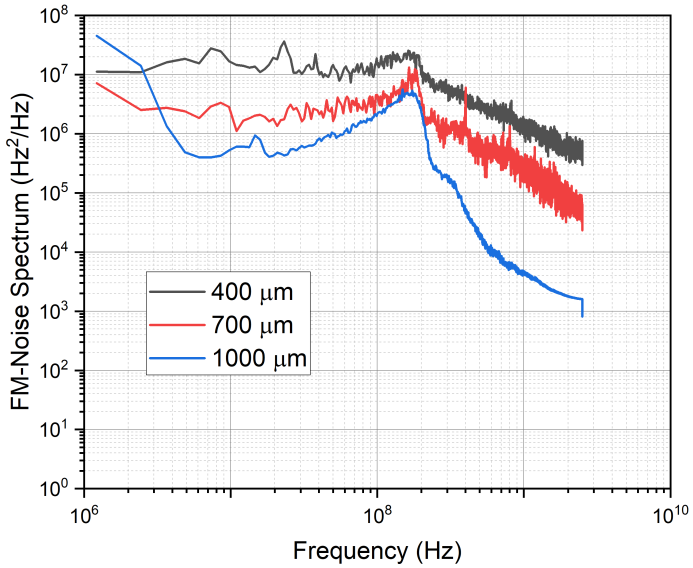

FIGURE 3.22: *FM-Noise spectra of 1550 nm devices with cavity lengths of 400, 700 and 1000 µm.*

This also follows the expected trend where the the longer cavity length corresponds to less noise. The measurement of the phase noise is important to the work on frequency combs because it gives us a full picture of the noise in our pump laser, which limits the quality of the comb and it is also a standard measurement for demonstrating the noise reduction before and after self-injection locking in a microresonator system [55].

3.3 Hybrid Square-Rectangular Lasers

The motivation for investigating the HSRLs is that the dual-lasing would allow the pumping of multiple microresonator resonances simultaneously from a single device. They are therefore characterised to determine the spacing of the dual modes, their tunability and the output power.

3.3.1 Dual-Lasing Measurements

Two arrays, each containing 15 HSRLs, were investigated. LI curves were obtained for each device by injecting a constant current of 10 mA into the square microcavity and sweeping the current of the Fabry-Pérot (FP current) while measuring the output power with a bare photodiode. The LI curves for both arrays are seen in Figure 3.23.

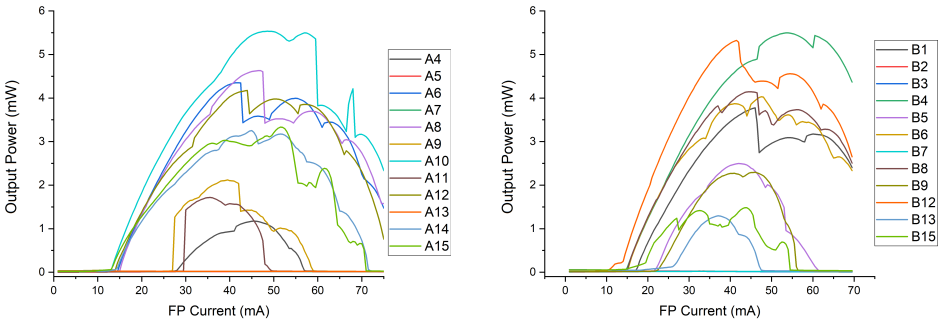

(a) (b)

FIGURE 3.23: *LI curves for two arrays (A and B) of HSRLs where FP current is swept while square current is kept constant at 10 mA*

The threshold FP current varied between 13 mA and 30 mA. Of the 30 devices tested, 12 produced very little output power and were disregarded for further measurements. The functioning devices were then examined to see if dual lasing could be observed.
As shown in Figure 3.24, the FP current was swept while the square current was kept constant, and vice versa, and spectral map of each was produced.

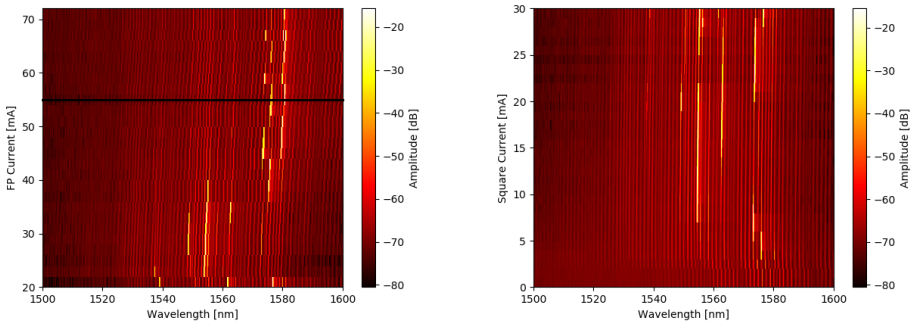

(a) *Spectral map where square current is kept constant at 8 mA while FP current is swept.* (b) *Spectral map where FP current is kept constant at 32 mA while FP current is swept.*

FIGURE 3.24: *Spectral data for device A14 (14th device on array A), amplitude recorded over 100 nm span of wavelengths for a range of FP and square currents.*

This allowed the lasers which showed dual lasing to be distinguished from those in which only single-mode lasing was present. Of the functioning devices, 6 showed instances of dual lasing. It was found that the device 'A14' showed the best dual lasing behaviour and this device was focussed on. Figure 3.25 shows a spectrum obtained from this device corresponding to the black line in Figure 3.24a. The mode lasing at the shorter wavelength is referred to as the 'blue' wavelength and the mode lasing at the longer wavelength is referred to as the 'red' wavelength. The SMSR of both of these peaks is calculated relative to the peak with the third highest amplitude in the spectra.

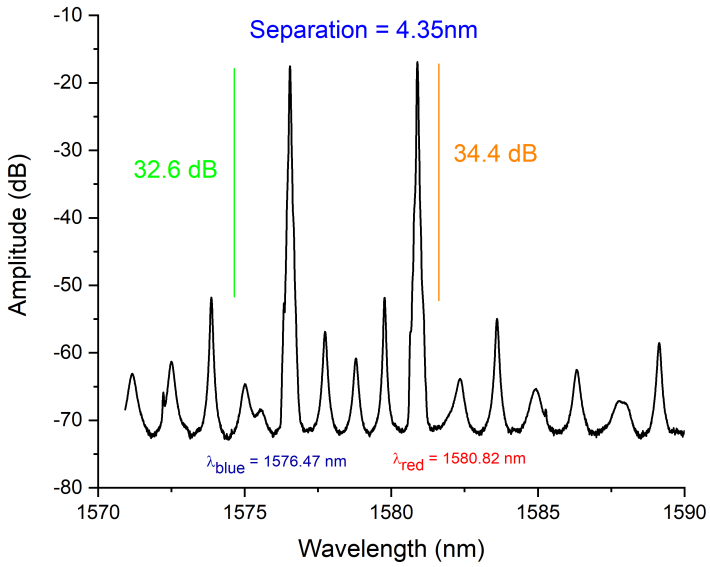

FIGURE 3.25: *Dual-lasing spectrum of a HSRL device*

In order to investigate the dual lasing behaviour, maps were generated that plot wavelength and power at various combinations of FP current and square current. In Figure 3.26, the FP current was swept between 15 mA and 70 mA in steps of 1 mA while the square current was swept between 5 mA and 40 mA in steps of 0.5 mA. An algorithm was developed to search through this data to identify points at which dual lasing is occurring. The wavelength and amplitude of the 3 peaks in the spectrum with the highest amplitudes were recorded from the OSA. The algorithm determines at which points there exists two lasing modes with amplitude greater than 20 dB more than the third peak and are separated by greater than 1.5 nm (the longitudinal mode-spacing of the 300 μm FP cavity is 1.2 nm) and these points were recorded as exhibiting dual lasing. The data is separated into data for the 'blue' mode and the 'red' mode. Figure 3.26 shows the SMSR map for both modes. White space on the map indicates that no dual lasing behaviour is present at these points.

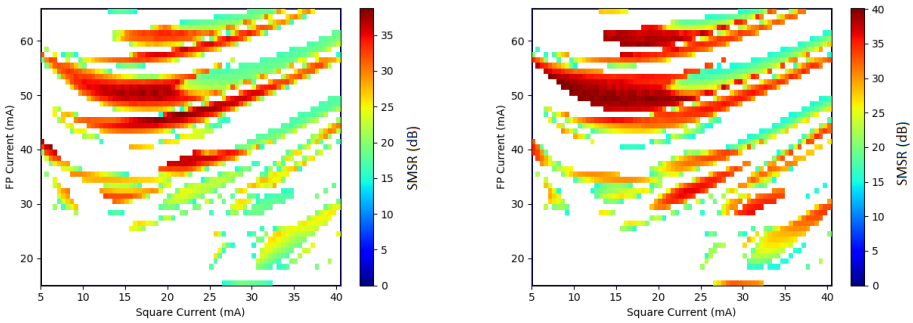

(a) *SMSR map for blue lasing mode.* (b) *SMSR map for red lasing mode.*

FIGURE 3.26: *SMSR maps for HSRL device, showing only regions where dual lasing is present.*

High SMSR for both modes is apparent in the region where the FP current is between approximately 48 mA and 57 mA and the square current is between 5 mA and 25 mA. Another scan was performed in this region, this time with the FP current swept in steps of 0.5 mA and the square current was swept in steps of 0.25 mA and the resulting maps are shown in Figure 3.27.

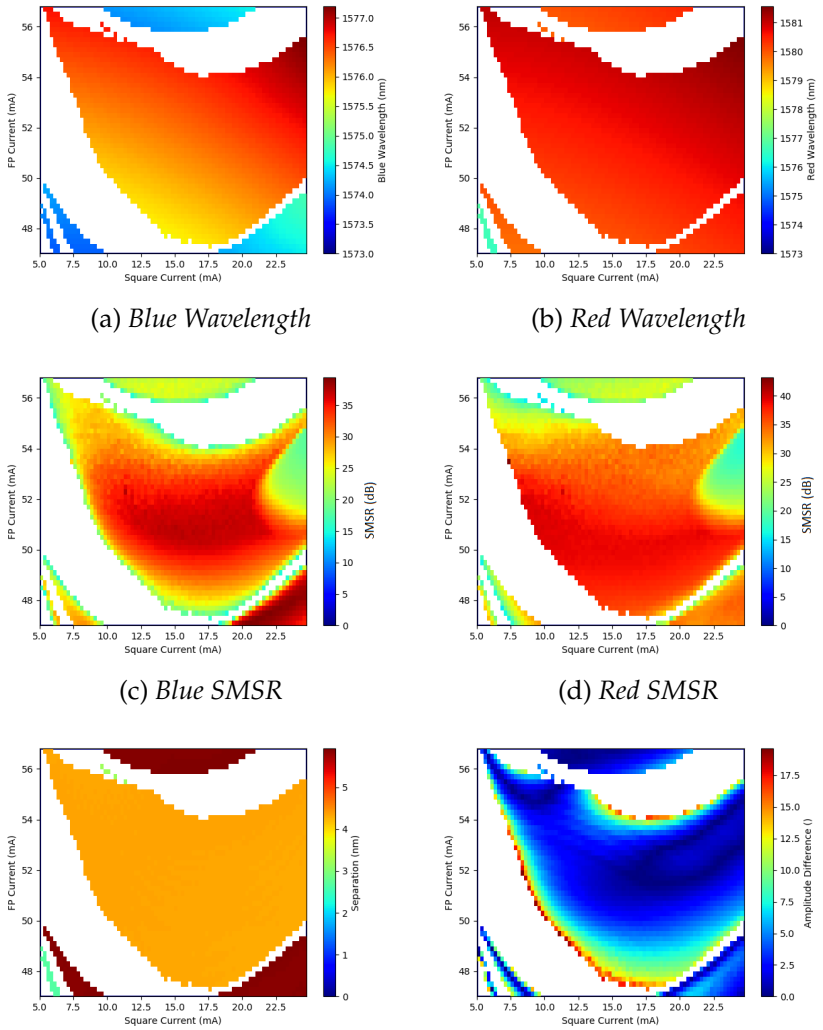

(a) *Blue Wavelength* (b) *Red Wavelength*

(c) *Blue SMSR* (d) *Red SMSR*

(e) *Mode Separation* (f) *Mode Amplitude Difference*

FIGURE 3.27: *Maps taken of dual-lasing region with high SMSR as seen in Figure 3.26*

As seen in Figure 3.27e, the mode separation is not tunable. The separation of 4.35 nm, which is constant for most of the regions where dual lasing is achieved corresponds to approximately 540 GHz, which is much greater than FSR of our microresonators.

3.3.2 Dual Wavelength Tuning

The wavelength maps show that, by varying the FP and square currents, the wavelength of both modes can be varied over a range of 2 nm, approximately between 1575 nm - 1577 nm for the blue mode and between 1579 nm - 1581 nm for the red mode. Figure 3.27e is a map of the wavelength separation between the blue and red mode. This separation is relatively constant at approximately 4.3 nm, corresponding to a frequency difference of approximately 0.5 THz. Figure 3.27f is a map of the difference in amplitude between the blue mode and the red mode. It is important for practical applications

that the intensity of both modes is approximately equal. By combining the data from SMSR, mode separation and intensity difference maps, the wavelength of the dual lasing modes can be tuned over a certain range such that the SMSR remains >30 dB, the separation remains constant and the intensity of the modes are equal.
A current path was selected using the data from Figure 3.27 and the spectral data was recorded as the FP and square currents were incrementally increased resulting in Figure 3.28a.

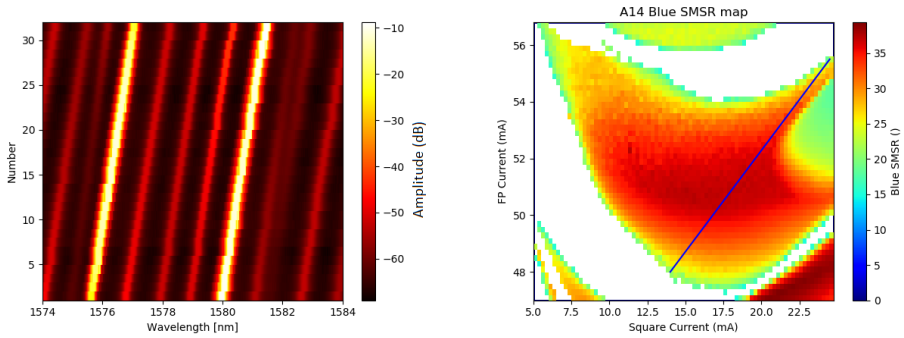

(a) *Spectral map showing tuning range of device A14.* (b) *Current path used for wavelength tuning of device A14.*

FIGURE 3.28: *Continuous wavelength tuning of device A14 over a range of 1.44 nm.*

The blue mode was tuned continuously from 1575.62 nm to 1577.05 nm while the red mode was tuned from 1579.96 nm to 1581.41. A tuning range of approximately 1.44 nm where the separation had a maximum deviation of 0.04 nm over this range.
The graphs in Figure 3.29 show the SMSR for each mode, mode separation and amplitude difference at each point in the current path shown in Figure 3.28b.

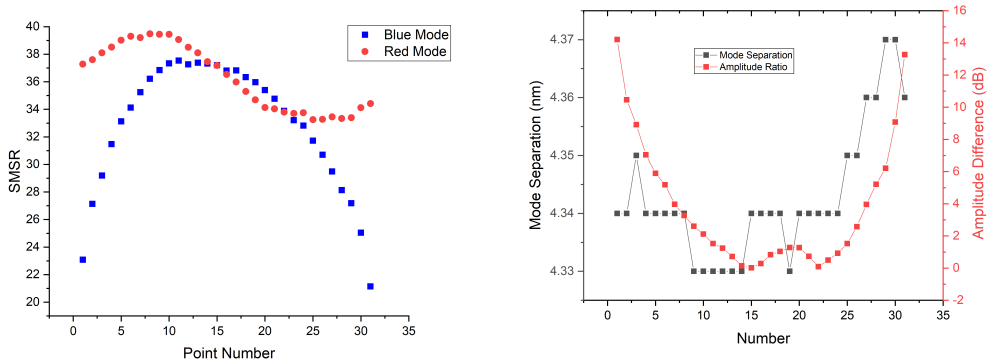

(a) *SMSR for each step in current path*

(b) *Mode separation and amplitude difference for each step in current path.*

FIGURE 3.29: *Mode information for each step of current path*

The SMSR for the blue mode is noticeably quite poor at the beginning and end of the current path. A current path that yields better overall SMSR and mode amplitude difference can possibly be attained although this will likely come at the cost of the wavelength range.

3.4 Conclusion

The arrays designed to operate near 1300 nm show a consistent L-I characteristic and output power across all devices, with the exception of Device 9 of Array 2. A continuous thermal tuning range of around 40 nm was obtained for the Array 2 with good SMSR ($>$ 35 dB) over the majority of the temperature range. However, SMSR is poorer at the blue end of our arrays where there is significant competition from the next FSR modes and SMSR drops below 30. This will be improved in future designs by incorporating more slots on the blue end of the array and through the use of the genetic algorithm code to optimize the designs [34]. The output power is shown to be in excess of 25 mW at 100 mA injection current and biasing the SOA section at a modest current. The Array 3 devices, with a lower number of slots and a single period, were insufficient to suppress the FSR modes adequately. As a result, devices on the blue end of the array lase at these FSR modes instead of the intended wavelength, and more of the devices make this wavelength jump as the temperature is increased. This resulted in a discontinuous wavelength tuning range. Linewidth was found to vary from 2 MHz for devices in the centre of each array to up to 12 MHz for devices at either end of the array. The overall linewidth can be improved by increasing the cavity length of the device but also with designs that suppress the FSR modes. In applications where linewidth is not a major consideration, the FSR mode hops could be exploited to increase the tuning range of the array. Overall these results indicate the laser array based on non-uniformly spaced etched slots has great potential for use as a source in O-band DWDM applications due to the tuning range of 40 nm with high SMSR. With a judicious choice of grating designs, it may be possible to use the FSR jumps in a positive fashion to produce a much wider tuning range of 60 nm or more.
Multiple-channel laser arrays such as these show promise as a pump source for microresonators as multiple resonances can be pumped simultaneously. For example, a multi-mode interference coupler such as the one shown in Figure 3.30 allows light from several devices to be combined and to pump the resonator simultaneously and with a much higher input power than a single device on its own.

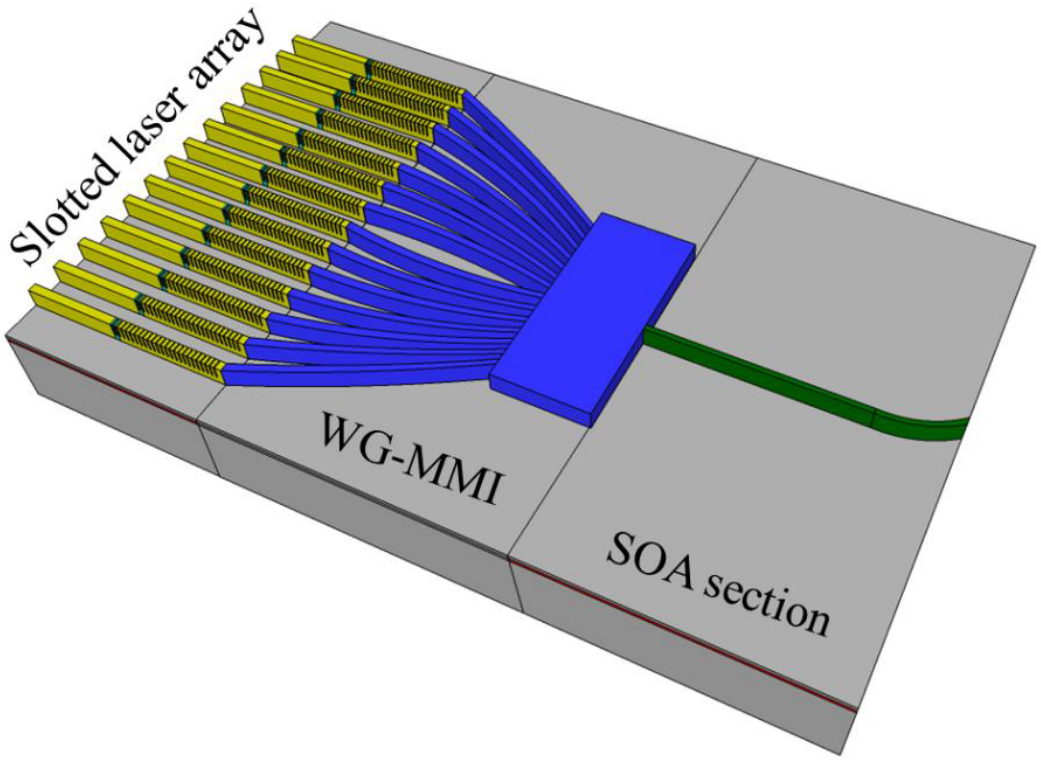

FIGURE 3.30: *Schematic structure of 12-channel laser array integrated with multi-mode interference coupler.*

This scheme is more suitable for DWDM applications rather than for comb generation as the noise from multiple lasers will be transferred to the noise of the comb.It is therefore vital to characterise and understand the behaviour of each device on the array so that the correct wavelength can be generated and the input power to the resonator controlled to ensure stability.
While dual-lasing was observed and shown to be tunable over a range while maintaining both modes, there is little tunability in the mode separation of the dual-modes. Since the separation of these modes does not match the resonance spacing in the dual-mode microresonators, we could not use these for pumping experiments. It was subsequently found, however, that only a single pump laser is required to excite the dual mode system and generate soliton microcombs. It was therefore decided to focus on using the slotted laser arrays as a pump source instead. In the next chapter, it is demonstrated how even a single device from one of these array can successfully generate a soliton from microresonator pumping with its power boosted by an EDFA.

Chapter 4

Octave-Spanning Frequency Combs in AlN Microresonators

Microresonators, using CW lasers as a pump source, can be used to generate an optical frequency comb (OFC) with relatively low input power and a high pump-conversion efficiency [9]. If the optical path length of the microring is an integer multiple of the wavelength of the incident light, then constructive interference can occur through multiple round-trips, building the intensity of the light.

Nonlinear optical effects can be seen when a microresonator is pumped by CW light [56]. In particular, the four-wave mixing (FWM) that occurs in whispering-gallery mode (WGM) microresonators can be used to generate OFCs. Beginning with light at two or more equally spaced frequencies, the process of FWM can generate light at more frequencies with equal spacing [57].

4.1 Optical Non-linearity and the Kerr Effect

At low intensity, the response of a material to light is expected to scale linearly with the amplitude of the electric field. If there is a high intensity of light incident upon the material, such as from a continuous-wave (CW) laser, "non-linear" effects can be observed. In this case, the polarisation density of the material has a non-linear response to the electric field of the incident light. This is expressed as a Taylor series expansion of the polarisation density $P(t)$ in terms of the electric field $E(t)$. [58]

$$P(t) = \epsilon_0(\chi^1 E(t) + \chi^2 E(t)^2 + \chi^3 E(t)^3 + ...) \tag{4.1}$$

where χ^n is the n^{th}-order optical susceptibility, which represent the nature of the interaction between the light and the material.

χ^2 interactions result in the generation of light at frequencies not present in the incident beam and include:
Sum/difference frequency generation (SFG/DFG), where two photons of frequencies, ω_1 and ω_2, from the pump source interact within the non-linear material to generate a single photon of frequency, ω_3. The frequency of the

generated photon is equal to the sum/difference of the frequencies of the incident photons. i.e. $\omega_3 = \omega_1 \pm \omega_2$
Second harmonic generation (SHG), this is a special case of SFG/DFG where the incident photons have the same frequency, $\omega_1 = \omega_2$. The frequency of the photon generated in the non-linear material, ω_3 from the two incident photons is then double the initial frequency, or $\omega_3 = 2\omega_1$.
Each of these χ^2 are illustrated in Figure 4.1.

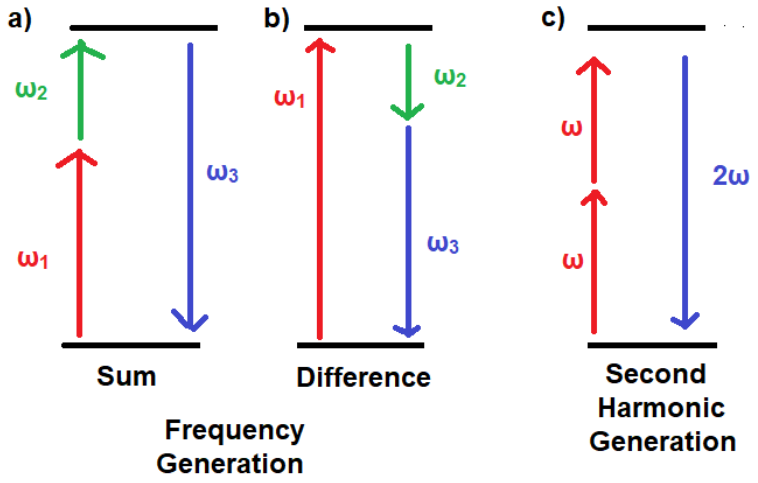

FIGURE 4.1: *Second-order non-linear processes. a) sum frequency generation. b) difference frequency generation. c) second harmonic generation.*

The χ^3 processes occur due to the optical Kerr effect where the refractive index of a material changes in the presence of an applied electric field. The change in index is proportional to the square of the electric field strength.
χ^3 non-linearities include:
Third harmonic generation (THG), where three photons of the same frequency, $\omega_1 = \omega_2 = \omega_3$, from the pump source interact to generate a single photon with frequency, ω_4. The frequency of the generated photon is equal triple the frequency of the incident photons. i.e. $\omega_4 = 3\omega_1$
Self-phase modulation (SPM), where the optical intensity of the light induces a non-linear refractive index change in the medium, causing a delay in the phase of the beam.
Cross-phase modulation (XPM), where the phase of a light beam is changed due to the interaction with another beam of light in the medium.
Four-wave mixing (FWM), where three photons of any frequencies interact to generate a photon of a new in the non-linear medium. i.e. $\omega_4 = \omega_1 + \omega_2 + \omega_3$. This can be degenerate, where the frequencies of two of the incident photons are equal. The process can also be non-degenerate, where all frequencies are different.
These χ^3 processes are illustrated in Figure 4.2.

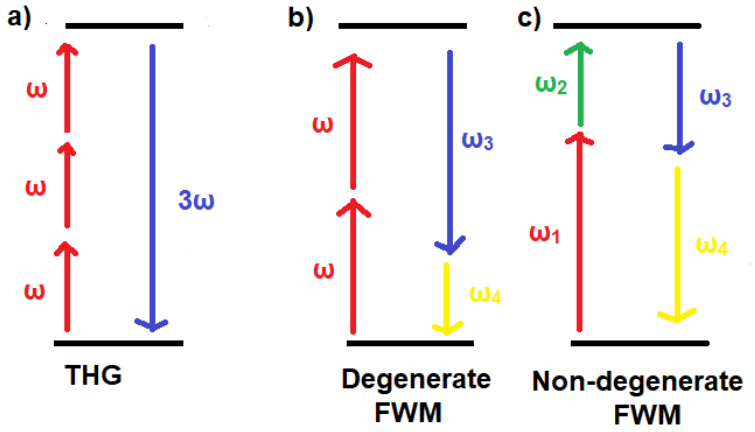

FIGURE 4.2: *Third-order non-linear processes. a) third harmonic generation. b) degenerate four-wave mixing. c) non-degenerate four-wave mixing.*

4.2 Comb Generation in Microresonators

In microresonator-based combs, the four-wave mixing process due to the χ^3 Kerr non-linearity is the mechanism which initiates the comb generation. They are therefore referred to as Kerr frequency combs. The first side-bands are generated via a degenerate FWM, where two pump photons with the same angular frequencies are annihilated and create two new photons on the side-bands with the frequency upshift known as signal ω_3 and frequency downshift known as idler ω_4. The signal and idler side bands can enhance the process of creation by the multiple side-band generation if their modes coincide with microresonator modes. For a cascaded process, non-degenerate FWM processes are significant in achieving the broadband frequency comb with the discrete and equidistant spectral lines in the frequency domain. In the non-degenerate process, two idler and/or signal photons serve as pump photons and produce two new photons of different frequencies. The process is termed non-degenerate as the frequencies of all four photons are different. Both degenerate and non-degenerate FWM leads to cascaded FWM and the comb spectrum contains discrete, equidistant comb lines. The broadening of the comb is limited by the microresonator dispersion.

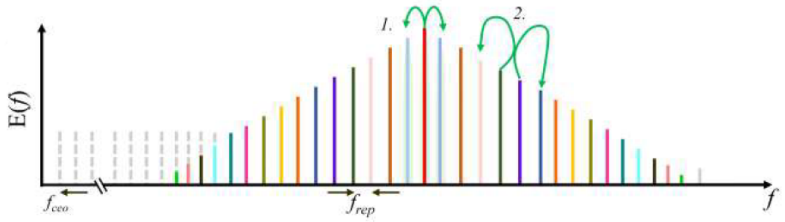

FIGURE 4.3: *Microresonator-based optical frequency comb spectrum via cascaded FWM.*

4.2.1 Octave Spanning Microcombs

An octave-spanning comb covers the spectrum of comb lines from n to $2n$ and the carrier envelope offset (CEO) frequency can be detected using the self-referencing f-2f scheme [3] [4]. This is where $f_n = f_{ceo} + nf_{rep}$ is the comb line at the short end of the spectrum and $f_{2n} = f_{ceo} + 2nf_{rep}$ is the line at the long end of the spectrum as illustrated in Figure 4.4. f_n can be doubled by making use of the χ^2 non-linearity to produce the second harmonic, $2f_n$.

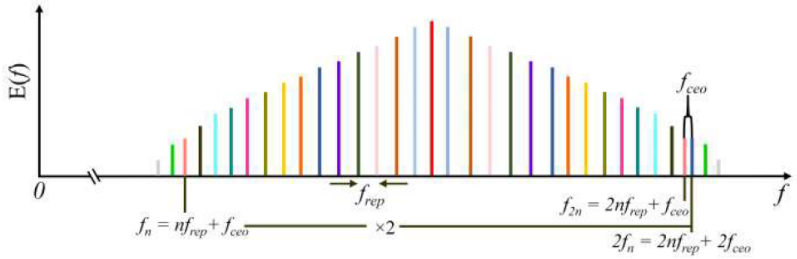

FIGURE 4.4: *Schematic illustration of f-2f self-reference scheme in an octave-spanning spectrum.*

By beating $2f_n$ with f_{2n}, the resulting beat note can be used to determine f_{ceo} as:

$$f_{ceo} = 2f_n - f_{2n} \tag{4.2}$$

4.3 Ring Microresonators

An all-pass microresonator consists of an optical waveguide in the shape of a closed loop which forms a resonant cavity which is evanescently coupled to a lateral, straight waveguide. An example of an all-pass microring resonator used in this work is seen in Figure 4.5.

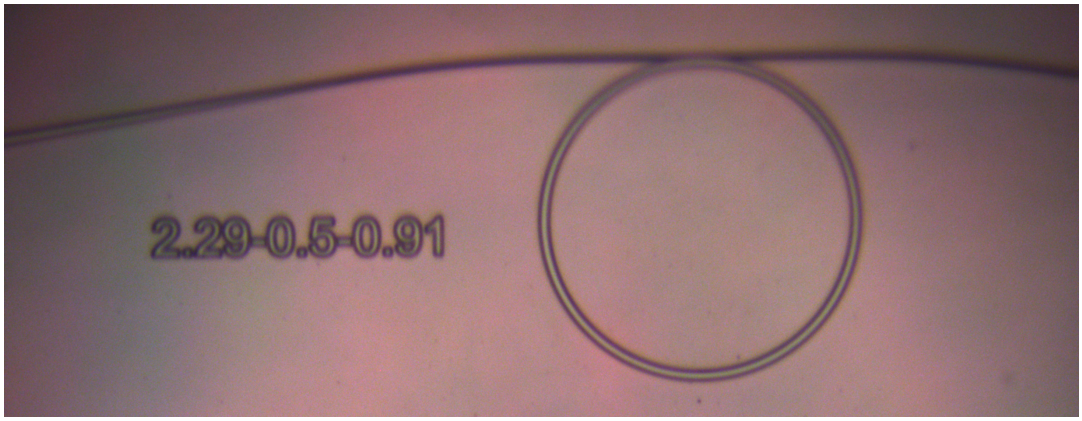

FIGURE 4.5: Microscope image of AlN microresonator. Note on left side of image, the waveguide is tapered to allow easier coupling with the pump laser.

Light from a continuous wave laser is injected into the input of the straight waveguide and then enters the microring through evanescent coupling in the region where the straight waveguide and microring are in close proximity. The light is confined within the waveguide due to total internal reflection (TIR) arising from the refractive index of the waveguide material (n_2) being greater than that of the cladding material (n_1). For TIR to occur, the angle of incidence of the incident light must be greater than the critical angle (θ_c) which is defined as:

$$\theta_c = sin^{-1}(\frac{n_1}{n_2}) \tag{4.3}$$

Figure 4.6 shows the waveguide structure, an AlN ridge on a sapphire substrate with SiO_2 substrate.

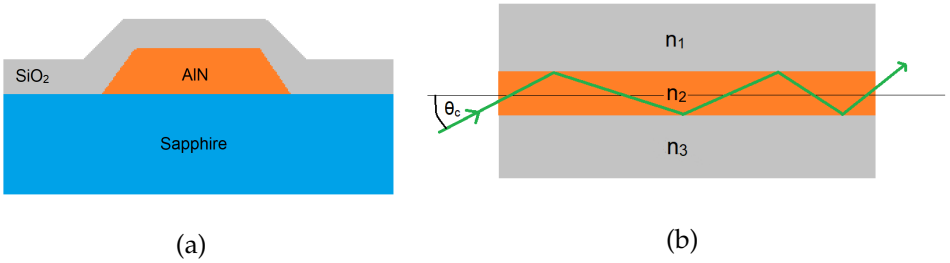

FIGURE 4.6: *a) cross-section of AlN waveguide on a sapphire substrate with SiO_2 cladding. b) illustration of total internal reflection.*

The phase of the light changes as it propagates through the waveguide. To minimise loss, the incident light must remain in phase with itself to achieve constructive interference. Light propagating with a particular angle in the waveguide corresponds to a waveguide mode with distinct phase velocity and therefore have a distinct refractive index. Furthermore, the optical waveguide modes have a definite electromagnetic field of propagation and

modes can be divided into the transverse electric (TE) and transverse magnetic (TM) fields. The TE and TM modes have transverse fields perpendicular to the plane of incidence.
The optical path length in a microresonator is a function of the dimensions of the microring and of the effective index of the waveguide. Constructive interference will occur when this optical path length is an integer multiple of the input light wavelength λ. The optical path length is the distance travelled by the light times the refractive index of the material. The condition is therefore:

$$n_{eff}L = m\lambda \tag{4.4}$$

where n_{eff} is the effective index, L is the effective cavity length and m is an integer. The light is injected into the input end of the straight waveguide and the constructive interference occurs at the region where the microring and straight waveguide are at close proximity. This is known as the coupling region and is where evanescent coupling. The evanescent field is an electric field that does not propagate as a wave, but instead is outside the waveguide and decays with distance from the surface. If another waveguide is within close proximity then the field can couple to the second waveguide and propagate. The coupling efficiency depends on the distance between the waveguides. This therefore allows the light to couple from the waveguide into the microring and vice versa, and the coupling can be optimised by narrowing the distance between the microring and waveguide.

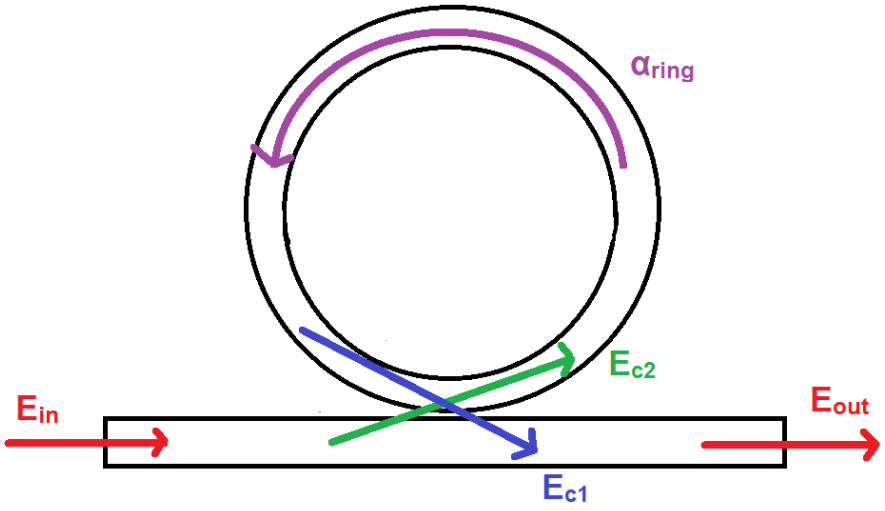

FIGURE 4.7: Illustration of coupling constants in an all-pass microresonator.

The input laser results in an electric field $E_{in} = E_{in}e^{-i\omega t}$ where ω is the angular frequency. Some amount of this light is then coupled into the ring in the coupling region, which is denoted by E_{c2}. This light then circulates in the ring and a certain amount, E_{c1}, is coupled back into the straight waveguide when it reaches the coupling region. The amplitude is reduced each cycle due to intrinsic losses in the ring such as material absorption, scattering and sidewall

roughness. The amplitude reduction is given by $a = e^{-\alpha_{ring} L/2}$ where α_{ring} is the intrinsic propagation loss in the ring per round-trip. The light coupled from the ring back into the straight waveguide is then collected at the output as E_{out}, which can be collected by an optical fibre and analysed.

4.3.1 Transmission, Enhancement and Quality Factors

Important factors in the resonator performance are the transition coefficient t through the coupler, which is the ratio of the input and output fields on each pass, as well as the cross-coupling coefficient k which compares the fields before and after the coupling region (E_{c2} and E_{c1}). In order for lossless coupling to occur, the following condition must be satisfied:

$$|k|^2 + |t|^2 = 1 \tag{4.5}$$

The performance is dependant on t and the intrinsic round-trip loss a. The desired coupling state is the critical coupling state, where the external coupling and intrinsic cavity losses are equal ($t = a$) and the intracavity power is at a maximum. If the gap between the microring and waveguide is too large, the coupling will be weak, a condition known as "under-coupling". This is where the cavity loss is greater than the coupling strength ($t < a$). Conversely, the system can be over-coupled, where the cavity loss is less than the external coupling strength ($t > a$), which can occur if the gap between the microring and waveguide is too narrow. An optical microresonator is characterized by measuring some of the following significant parameters such as transmission spectrum T, enhancement factor B and quality factor Q. The transmission spectrum is the ratio of the transmitted power to the input power at a particular frequency.

Transmission and Enhancement

The output field of the microresonator can be written in matrix form [59] [60] as:

$$\begin{bmatrix} E_{c2} \\ E_{out} \end{bmatrix} = \begin{bmatrix} t & ke^{\frac{i\pi}{2}} \\ ke^{\frac{i\pi}{2}} & t \end{bmatrix} \begin{bmatrix} E_{c1} \\ E_{in} \end{bmatrix} \tag{4.6}$$

After a single cycle around the cavity, the field undergoes a phase change ϕ, which can be expressed as:

$$\phi = \beta L = \frac{2\pi n_{eff}}{L} \tag{4.7}$$

Accounting for this phase shift and the cavity losses through the ring, the field coupled back into the straight waveguide when it reaches the coupling region, E_{c1}, can be expressed as:

$$E_{c1} = e^{-\alpha_{ring} L} e^{i\beta L} E_{c2} = a e^{i\phi} E_{c2} \tag{4.8}$$

the field coupled into the ring from the waveguide, E_{c2} can be expressed as:

$$E_{c2} = tE_{c1} + ke^{\frac{i\pi}{2}}E_{in} \tag{4.9}$$

and the field at the output of the waveguide, E_{out} is given by:

$$E_{out} = ke^{\frac{i\pi}{2}}E_{c1} + tE_{in} \tag{4.10}$$

From equations 4.8, 4.9 and 4.10 we obtain:

$$E_{c2} = ke^{\frac{i\pi}{2}}E_{in} + tae^{i\phi}E_{c2} \tag{4.11}$$

$$E_{out} = tE_{in} + kae^{i\phi}e^{\frac{i\pi}{2}}E_{c2} \tag{4.12}$$

equation 4.11 can be rearranged as:

$$E_{in} = \frac{E_{c2} - tae^{i\phi}E_{c2}}{ke^{\frac{i\pi}{2}}} \tag{4.13}$$

Combining equations 4.12 and 4.13:

$$E_{out} = \frac{tE_{c2} - t^2ae^{i\phi}E_{c2}}{ke^{\frac{i\pi}{2}}} + ae^{i\phi}e^{\frac{i\pi}{2}}kE_{c2} \tag{4.14}$$

$$E_{out} = \frac{tE_{c2} - t^2ae^{i\phi}E_{c2} - ak^2e^{i\phi}E_{c2}}{ke^{\frac{i\pi}{2}}} \tag{4.15}$$

$$E_{out} = \frac{tE_{c2} - ae^{i\phi}E_{c2}}{ke^{\frac{i\pi}{2}}} \tag{4.16}$$

From equations 4.13 and 4.16 we can obtain the ratio between the output and input electrical fields:

$$\frac{E_{out}}{E_{in}} = \frac{t - ae^{i\phi}}{1 - ate^{i\phi}} \tag{4.17}$$

The transmission T can therefore be expressed as:

$$T = |\frac{E_{out}}{E_{in}}|^2 = \frac{t^2 + a^2 - 2atcos\phi}{1 + a^2t^2 - 2atcos\phi} \tag{4.18}$$

An enhancement or build-up factor, B can also be expressed as the ratio between the optical field circulating in the ring to the input field:

$$\frac{E_{c1}}{E_{in}} = \frac{ake^{i\phi}}{1 - ate^{i\phi}} \tag{4.19}$$

and so:

$$B = |\frac{E_{c1}}{E_{in}}|^2 = \frac{(1 - t^2)a^2}{1 + a^2t^2 - 2atcos\phi} \tag{4.20}$$

At the critical coupling condition ($t = a$), the transmission is near zero and the enhancement factor is at a maximum. This can be seen in Figure 4.8.

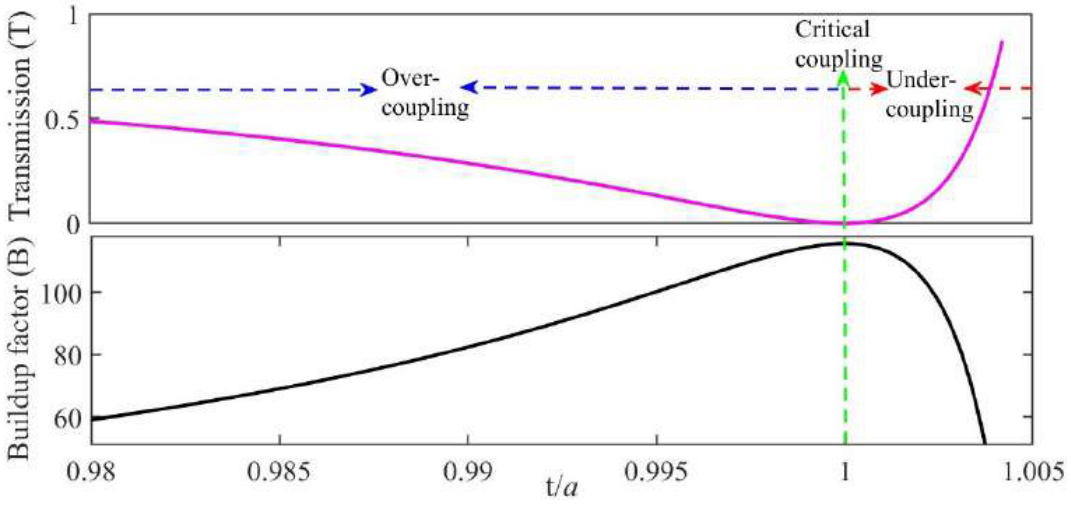

FIGURE 4.8: Calculation of transmission and enhancement factors vs t/a ratio for AlN microresonator. Modelling by Dr Adnan Afridi.

For the best operation of the microresonator, it is therefore necessary to optimise these parameters. t can be optimised by carefully choosing the length of the gap between the microring and the waveguide, while a can be improved by using fabrication techniques to limit cavity losses.

4.3.2 Free Spectral Range and Full Width at Half Maximum

The free spectral range (FSR) in microresonators refers to the separation between adjacent resonance modes, which is related to the effective cavity length. The FSR can be defined by the frequency spacing between modes as:

$$FSR = \Delta f = f_{m+1} - f_m \tag{4.21}$$

where

$$\Delta f = \frac{c}{n_g L} \tag{4.22}$$

or in terms of wavelength as:

$$FSR = \Delta\lambda \approx \frac{\lambda^2}{n_g L} \tag{4.23}$$

where the dominator is the group index, n_g, rather than the effective index. The group index takes dispersion effects into account [60] and is defined as:

$$n_g = n_{eff} - \lambda_0 \frac{dn_{eff}}{d\lambda} \tag{4.24}$$

The group index and the corresponding group velocity $v_g = \frac{c}{n_g}$ describes the velocity of the pulse envelope travelling in a dispersive medium.

The optical path length L for a ring resonator is given by the circumference of a resonator of radius r. The path length is therefore $L = 2\pi r$ and we can express the FSR for a microring resonator as:

$$FSR = \frac{\lambda^2}{2\pi n_g r} \tag{4.25}$$

Therefore, a decrease in the ring radius will result in a larger FSR as shown in Figure 4.9

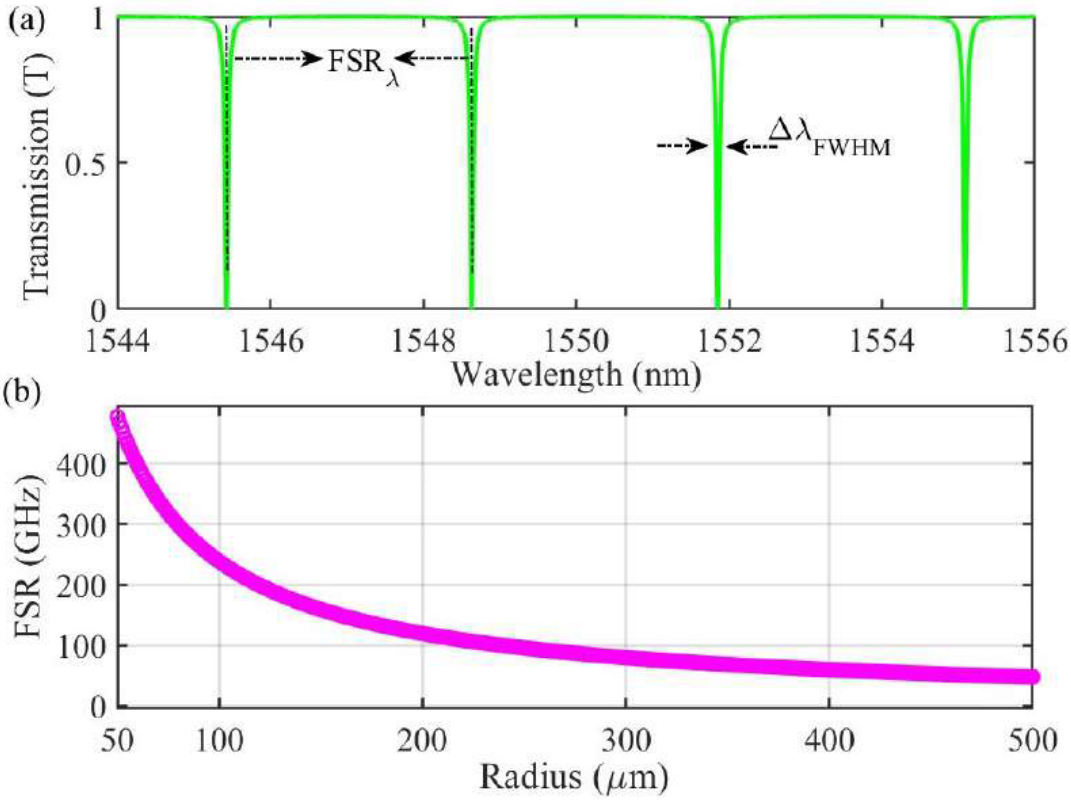

FIGURE 4.9: a) Simulated transmission versus wavelength for 60 μm radius AlN microresonator. b) Simulated free spectral range vs ring radius. Modelling by Dr Adnan Afridi.

The FWHM is a measure of the broadness of spectral peaks and is defined by the width of the peak at a the point that it as half of the maximum amplitude. The FWHM, $\Delta\lambda_{FWHM}$ can be expressed as [60]:

$$\Delta\lambda_{FWHM} = \frac{(1-at)\lambda_{res}^2}{\pi n_g L\sqrt{at}} \tag{4.26}$$

or, in terms of the FSR

$$\Delta\lambda_{FWHM} = \frac{FSR_\lambda(1-at)}{\pi\sqrt{at}} \tag{4.27}$$

Quality Factor

The quality factor Q is a measure of how well the microresonator confines the incident light. When light is coupled into a microresonator, there is loss associated with the propagation of the light through the cavity through absorption, scattering etc. and these intrinsic losses are associated with an intrinsic quality factor Q_{int}. There is also loss as a result of the coupling between the microresonator and the waveguide, denoted by the coupling quality factor Q_c. The overall loss is referred to as the loaded quality factor Q_L and is related to the intrinsic and coupling factors as:

$$\frac{1}{Q_L} = \frac{1}{Q_{int}} + \frac{1}{Q_c} \tag{4.28}$$

Q_L can be defined as the ratio of the energy stored by the resonator to the energy lost per round trip. This parameter also determines the sharpness of resonance modes and can be measured experimentally as:

$$Q_L = \frac{\lambda_{res}}{\Delta\lambda}\frac{1}{Q_c} \tag{4.29}$$

where $\Delta\lambda$ is the FWHM of the resonant mode. From 4.27, we can write this as:

$$Q_L = \frac{\pi L n_g}{\lambda}\frac{\sqrt{at}}{1-at} \tag{4.30}$$

As the intrinsic quality factor describes only the energy in the resonator itself, ignoring the coupling from the waveguide, an expression for Q_{int} can be obtained by setting $t = 1$.

$$Q_{int} = \frac{\pi L n_g}{\lambda}\frac{\sqrt{a}}{1-a} \tag{4.31}$$

as $a = e^{-i\alpha_{ring}L}$, we can therefore approximate 4.31 as

$$Q_{int} = \frac{2\pi n_g}{\lambda\alpha_{ring}} \tag{4.32}$$

The intrinsic and coupling quality factors are related to the loaded quality factor and the transmission [61] and can be expressed as:

$$Q_c = \begin{cases} \frac{2Q_L}{1+\sqrt{T}}, & \text{if } a > t \\ \\ \frac{2Q_L}{1-\sqrt{T}}, & \text{if } a < t \end{cases} \tag{4.33}$$

$$Q_{int} = \begin{cases} \frac{2Q_L}{1-\sqrt{T}}, & \text{if } a > t \\ \\ \frac{2Q_L}{1+\sqrt{T}}, & \text{if } a < t \end{cases} \tag{4.34}$$

Figure 4.10 shows the calculated variation of each Q factor versus the internal cavity loss of the microring for each coupling condition. It was noticed that at the critical coupling condition, ($Q_{int} = Q_c$) and the loaded Q factor could be obtained as $2Q_L = Q_{int} + Q_c$. In the case of over-coupling, $Q_{int} > Q_c$ whereas in the under-coupled regime, $Q_{int} < Q_c$. The coupling quality factor is therefore something we can optimise to achieve our desired, overall Q_L.

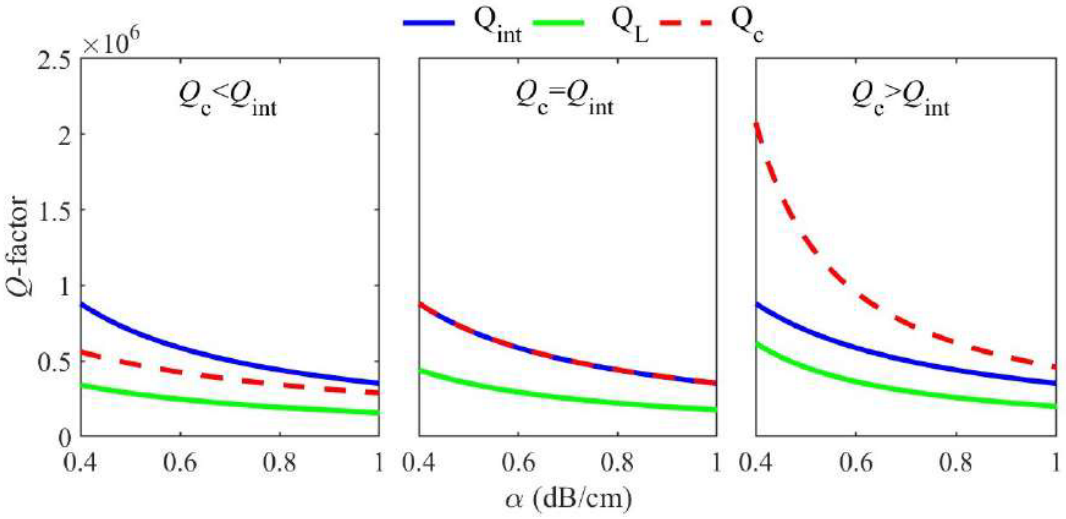

FIGURE 4.10: Simulated intrinsic, coupling and loaded Q factors as a function of internal cavity losses for each coupling condition. Modelling by Dr Adnan Afridi.

Another parameter is the ratio between the maximum and minimum transmission (T_{max} and T_{min}), known as the extinction ratio (ER). This can be expressed mathematically as:

$$ER = \frac{T_{max}}{T_{min}} = \left(\frac{Q_{int} - Q_c}{Q_{int} + Q_c}\right)^2 \tag{4.35}$$

The extinction ratio is at a maximum at the critical coupling condition, which can be seen in 4.11 where the calculated ER is plotted against Q_c / Q_{int}, which is equal to 1 at the critical coupling condition.

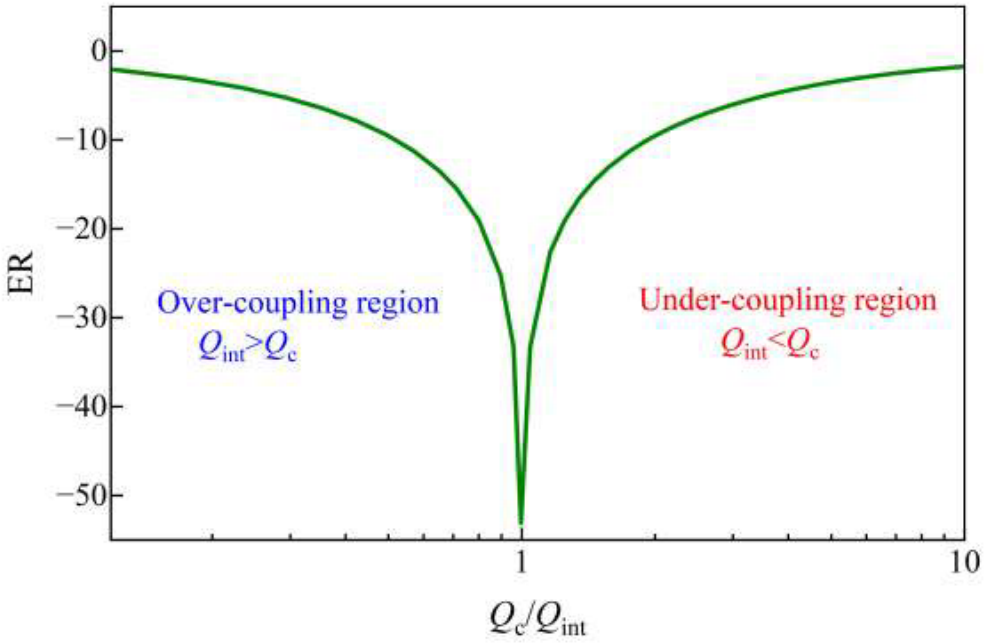

FIGURE 4.11: Simulated extinction ratio versus the ratio of the coupling quality factor to the intrinsic quality factor. Modelling by Dr Adnan Afridi.

The extinction ratio can also be expressed as the logarithm of the ratio of the maximum and minimum transmissions.

$$ER = 10\log_{10}\left(\frac{T_{max}}{T_{min}}\right) \tag{4.36}$$

4.3.3 Dispersion in Microresonators

In a medium, the refractive index is generally a function of the frequency, and therefore wavelength. i.e. $n = n(f)$ or $n = n(\lambda)$ This results in a process called dispersion, where the waves propagating through a medium will travel with different speeds depending on their frequency. In an optical waveguide, there is additional dispersion due to boundary conditions which depend on the waveguide's geometry. This geometric dispersion is dependent of factors such as the width, height and angle of the waveguide. The parameter known as the effective index, n_{eff} is used to account for both the refractive index of the waveguide material and the geometry of the waveguide [58] and is given by:

$$n_{eff} = \frac{\beta}{k_0} \tag{4.37}$$

where $k_0 = \frac{2\pi}{\lambda}$ is the wavevector in free space. As light propagates through a dispersive medium, each component of the input field experiences a phase shift due to the frequency dependence of the propagation constant [62]. An exact expression is difficult to obtain, but it can be expanded as a Taylor series around the carrier frequency ω_0:

$$\beta_w = \beta_0 + \beta_1 (\omega - \omega_0) + \frac{1}{2!} (\omega - \omega_0)^2 + ... \tag{4.38}$$

The zero-order term, β_0 describes a common phase shift. The first order term, β_1, is related to the inverse of the group velocity v_g and describes a time delay of the pulse envelope. The second-order term, β_2 is related to the group velocity dispersion (GVD) and is given by the derivative of the inverse group velocity with respect to the frequency. The GVD is represented by the dispersion parameter D, which is dependent on how the refractive index varies with the frequency.

$$D = -\frac{\lambda}{c} \frac{\partial^2 n_{eff}}{\partial \lambda^2} \tag{4.39}$$

Depending on the sign of D, the dispersion can be classified as either anomalous or normal. If $D < 0$, the dispersion is normal, and the refractive index generally increases with an increase in the frequency of the light. In the case that $D > 0$, the dispersion is anomalous. This means that, at certain frequency ranges, the refractive index can actually decrease with increasing frequency.
Anomalous dispersion is required for the generation of broadband frequency combs due to modulational instability and high four-wave mixing efficiency [63].
Due to dispersion, comb lines may not be equidistant as modes at different frequencies experience dispersion differently. The result is that the FSR increases with increasing frequency. As illustrated in Figure 4.12, the spacing between modes becomes larger for modes at higher frequencies.

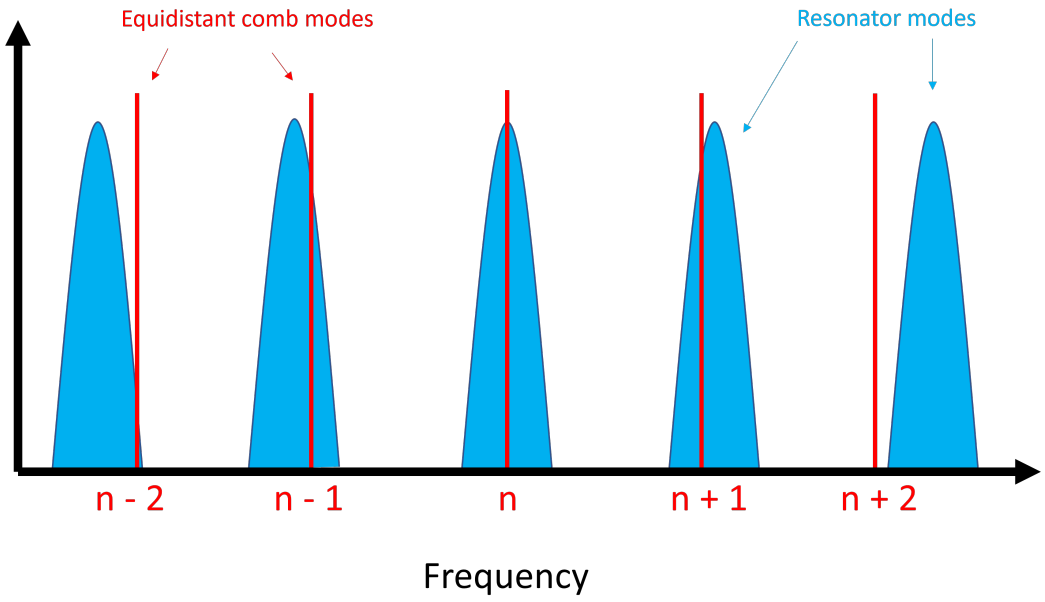

FIGURE 4.12: Schematic showing the non-equidistant comb lines as a result of dispersion effects.

To avoid this, it is necessary to engineer the geometry of the resonator such that there is near-zero anomalous dispersion ($D \approx 0$) over the required range. The resonance frequencies of a microresonator can be Taylor-expanded around a central pump frequency ω_0, using the relative mode number μ [64]:

$$\omega_\mu = \omega_0 + D_1\mu + \frac{1}{2!}D_2\mu^2 + \frac{1}{3!}D_3\mu^3 + ... \tag{4.40}$$

where $D_1/2\pi$ is the FSR in the range around the pump frequency and D_2 and D_3 are the second and third order dispersion terms, respectively.
The deviation of the resonance frequencies and dispersion terms when compared to a comb of fully equidistant frequency modes is defined as the integrated dispersion (D_{int}) [65] and can be expressed as:

$$D_{int} = \omega_\mu - (\omega_0 + D_1\mu) \tag{4.41}$$

The microresonators used in our group were therefore designed with geometries to achieve this near-zero anomalous dispersion in order to generate broad frequency combs with equally spaced modes. This was achieved using the COMSOL software in order to simulate the material and geometric dispersion resulting from various resonator geometries. It had previously been shown that the wave-optics module in COMSOL could be configured to accurately model the effective index and field distribution [66].

4.4 Generation of Dissipative Kerr Soliton Microcombs

A soliton is a waveform that preserves its shape as it propagates in a dispersive medium. Dissipative solitons achieve this by balancing the optical losses and gain in the resonator cavity as well as balancing the nonlinear effects of the material with dispersion. This "double-balance is represented in Figure 4.13. Dissipative Kerr solitons (DKSs) are so named because the source of the parametric gain in the resonator is the four-wave mixing which arises due to the Kerr non-linearity.

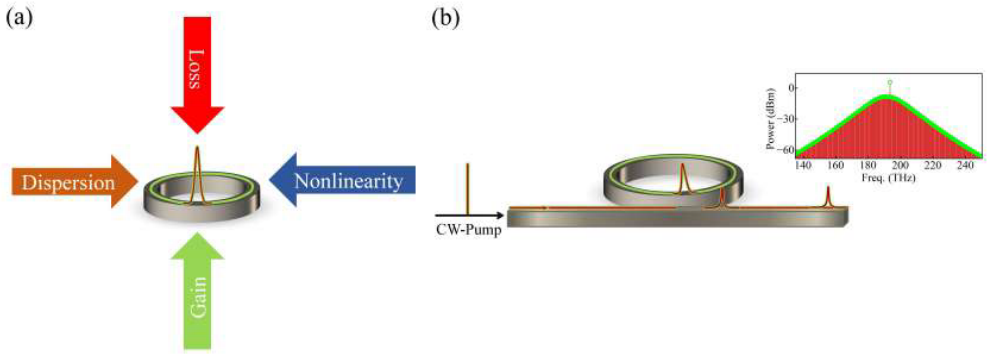

FIGURE 4.13: a) Sketch of effects, such as dispersion balanced by Kerr non-linearity and loss balanced by the gain to maintain the single soliton state. (b) Single soliton in the microresonator cavity and the obtained spectrum at the output.

Soliton microcombs are highly desirable as they are compact, low-noise, require low input power and can operate with gigahertz to terahertz line-spacing [67]. However, accessing the soliton state is difficult due to the fine balancing of parameters. To generate and maintain a soliton requires the minimisation of the thermo-optic effects which occur as the resonator heats up while pumping, resulting in instability. Methods have been developed to overcome this problem such as power-kicking [68], thermal cavity tuning [69], single-sideband modulation [70] and the use of an auxiliary pump laser [71]. Many of these methods are highly effective, though they require additional equipment and their complexity makes them unsuitable for many practical applications.

A dual-mode scheme, where dual resonance modes are used to compensate for the thermal effects in order to generate DKSs, with a mixed polarisation has been shown to aid in stabilising the soliton state [72], however this is a complex method due to the requirement of very precise polarisation control. We utilise a relatively simpler method. A CW laser is used to pump two close resonances with the same polarisation. This method of a single pump, two resonances and the same polarisation is referred to as the one pump, two resonance, one polarisation (1P2R-1P) scheme [73]. In this scheme, the fundamental transverse electric (TE_{00}) resonance mode is pumped by the CW laser at the same wavelength, initiating the FWM process while the higher-order TE_{10} mode is used as an auxiliary mode to offset thermal effects and stabilise the soliton. The stages of this process are illustrated in Figure 4.14.

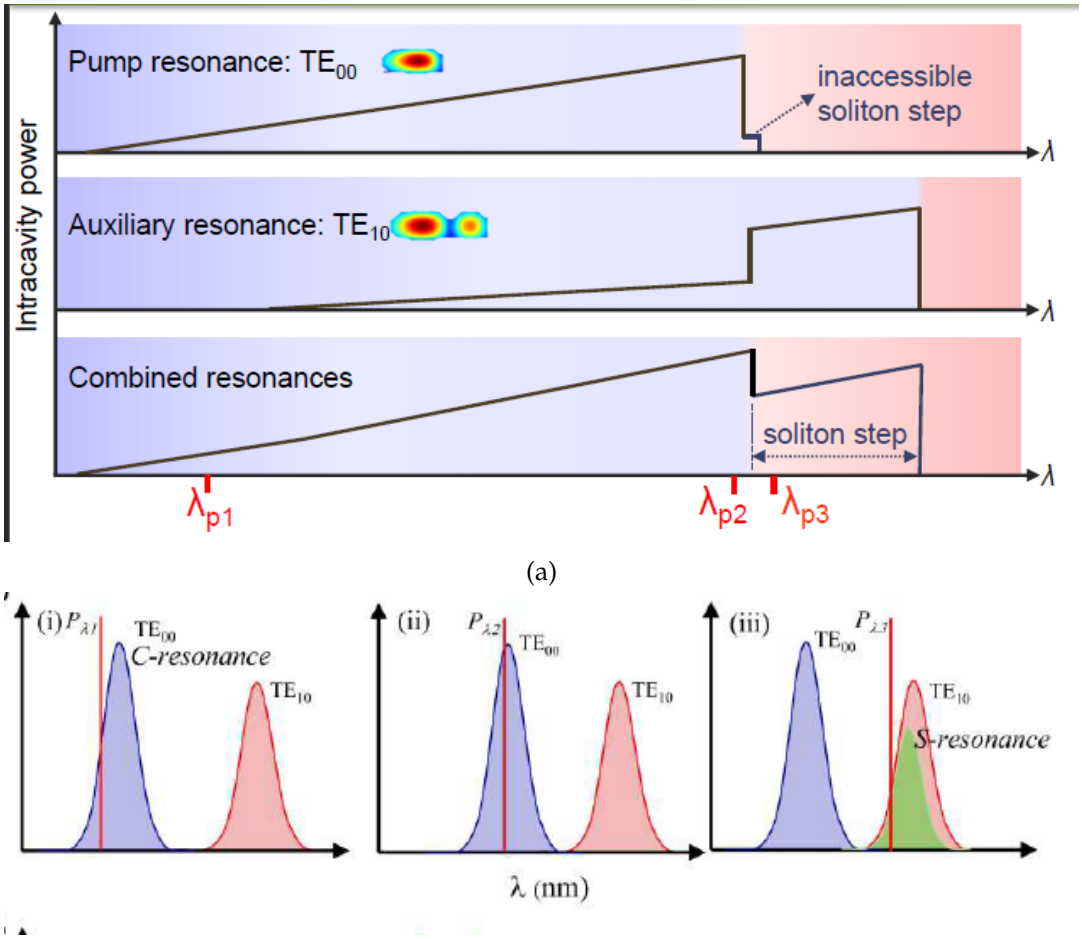

FIGURE 4.14: a) Schematic of intracavity power vs wavelength of the pump resonance, auxiliary resonance and the combination of both resonance as the wavelength is swept. b) Schematic of the process of using dual-modes for soliton stabilisation.

In stage i), the TE_{00} pump mode begins at the blue-detuned region away from the cavity resonance (C-resonance) at λ_{p1}. The wavelength is then swept such that it red-shifts towards the C-resonance, this is known as forward-tuning. As the C-resonance is approached, a primary comb forms with line-spacings equivalent to multiples of the FSR. Continuing to sweep the wavelength such that power is injected into both the TE_{00} and TE_{10} resonance modes causes both resonances to red-shift due to thermal effects (stage ii)). The wavelength λ_{p2} is still blue-shifted relative to the TE_{00} mode and microcomb with modulation instability (MI) is observed. Further forward-tuning of the pump wavelength will eventually result in soliton generation at λ_{p3} and corresponds to a sudden drop in the intracavity power, causing a blueshift in the resonance modes. The pump wavelength is now red-shifted relative to the TE_{00} mode and most of the pump power is now injected into the TE_{10} mode and so the presence of this auxiliary mode has stabilised the soliton state by compensating for the sudden change in intracavity power. In this stable soliton state (stage iii)), the pump resonance has been split into the C-resonance and soliton resonance (S-resonance). The optimal separation between the

TE_{00} and the TE_{10} resonances can be engineered through the design of the resonator geometry and through careful fabrication.

4.5 Microresonator Characterisation

A dual-mode AlN microring resonator with a radius of 60 μm and a cross section of 2.29 μm × 1.2 μm was used for DKS generation. The device was first characterised using a Santec tunable semiconductor laser as a pump source. Figure 4.15 shows the experimental setup for characterisation.

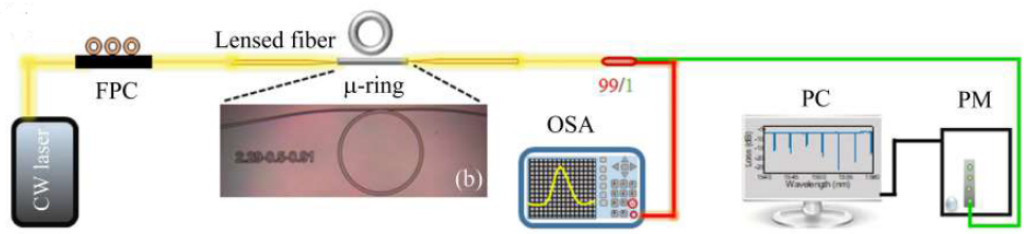

FIGURE 4.15: Experimental setup used for device characterization.

Light from the TSL is injected into the input waveguide via lensed fibre and is collected at the output by another tapered lensed fibre. A fibre polarization controller (FPC) is used to select the desired input polarization. The beam is then split by a fibre coupler with 99 % of he light being sent to the OSA to detect the coupling signal. The remaining 1 % is sent to a power monitor to obtain the transmission spectrum.
The transmission spectrum was measured for wavelength in the range 1544 nm to 1564 nm and is shown in Figure 4.16 a). The two transverse electric (TE) modes, the fundamental TE_{00} and first order TE_{10} , are present and can be distinguished from each other due to the differing FSR spacing (374 GHz and 366 GHz, respectively).

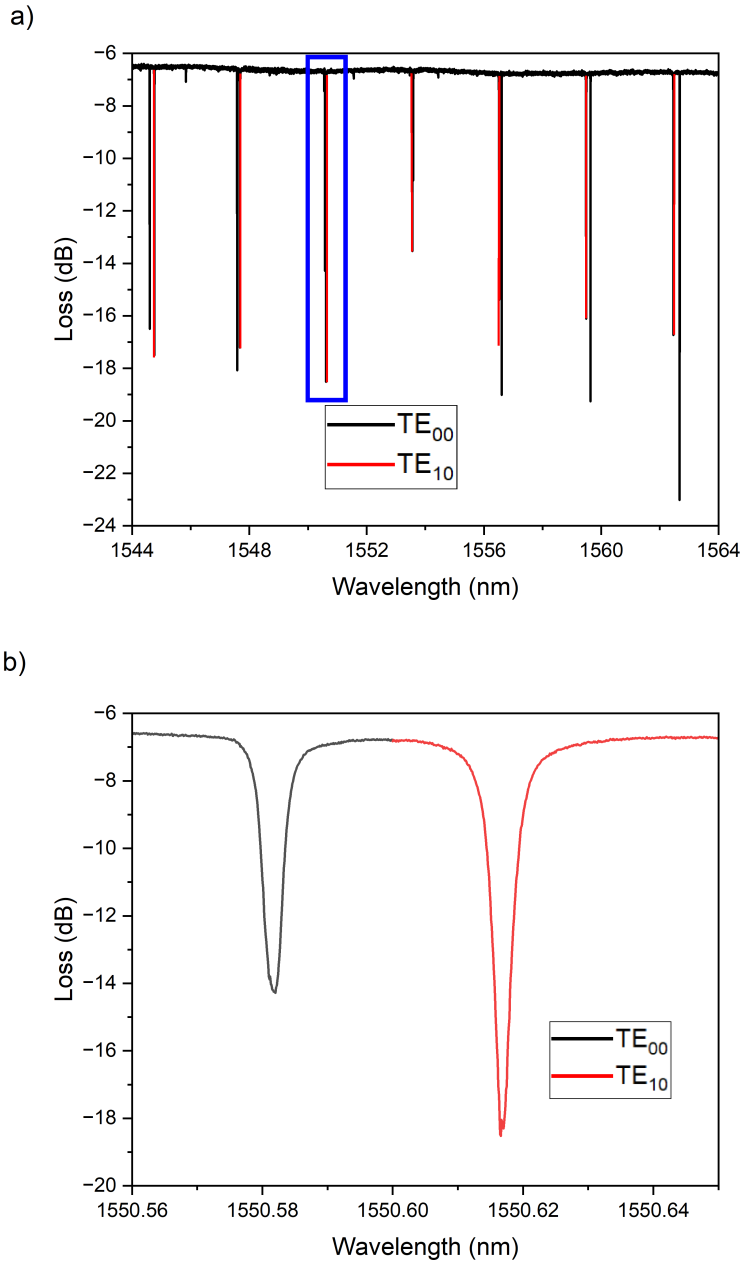

FIGURE 4.16: a) Transition spectrum of TE_{00} and TE_{10} modes in an AlN microresonator. b) Zoomed in view of dual resonances centred about 1550.6 nm. Data recorded by Dr Hai-Zhong Weng.

A pair of closely adjacent resonances were found at approximately 1550.6 nm, the region highlighted by the blue rectangle. The TE_{00} mode (black) was found to be centred at 1550.582 nm while the TE_{10} mode (red) was centred at 1550.617 nm. This corresponds to a separation of 35 pm or approximately 4.37 GHz. The loaded quality factor Q_L, which was previously defined as a measure of the sharpness of the resonances was obtained by fitting a Lorentzian profile to each resonance mode to determine the FWHM. The fitting is shown separately for each mode in Figure 4.17.

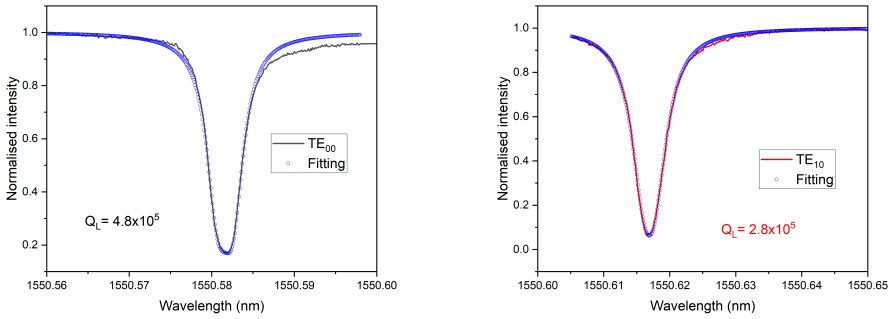

(a) (b)

FIGURE 4.17: Determination of loaded quality factor for a) TE_{00} resonance and b) TE_{10} resonance

The loaded quality factor was determined to be 4.8×10^5 for the TE_{00} resonance and 2.8×10^5 for the TE_{10} resonance.
The integrated dispersion D_{int} was also calculated and is shown in Figure 4.18.

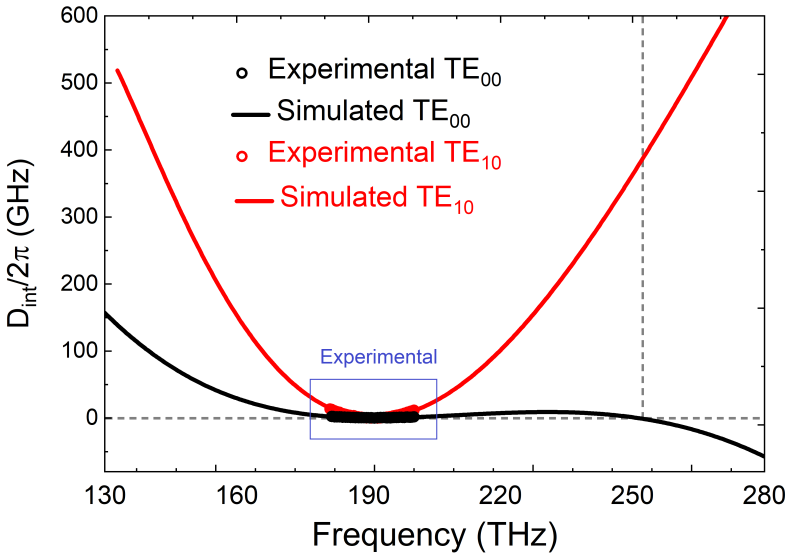

FIGURE 4.18: Simulated integrated dispersal D_{int} for TE_{00} and TE_{10} resonances with experimental results for 50 resonances. Data recorded by Dr Hai-Zhong Weng.

The D_{int} was simulated over a wide frequency range, from 130 THz to 280 THz and plotted along with experimental results from 50 resonances, represented as circles in 4.18. The centre frequency of the TE_{00} and TE_{10} and resonances are 193.292 THz and 193.289 THz, respectively and the $D_2/2\pi$ of these resonances were calculated to be 4.8 MHz and 36.8 MHz, respectively [16]. This means that the dispersion is anomalous, a necessity for broadband comb generation and the TE_{00} resonance in particular has near-zero dispersion.

4.6 Kerr Soliton Frequency Comb Generation.

The experimental setup for generating an octave-spanning soliton microcomb is shown in Figure 4.19.

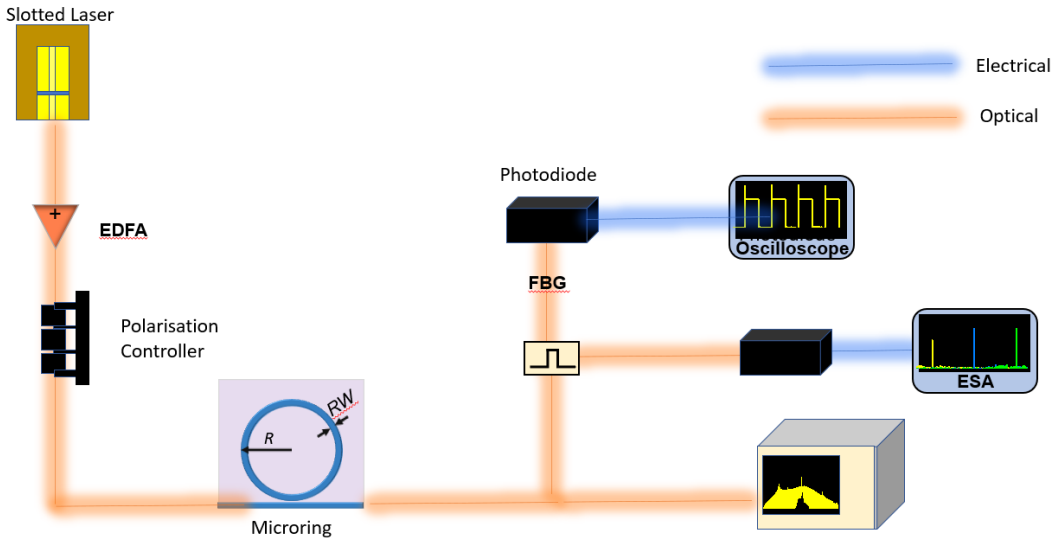

FIGURE 4.19: *Comb generation setup using TSL as pump source.*

The output of a pump laser is amplified by an EDFA. The power required is dependent on parameters such as the Q factor, extinction ratio, and mode separation. This light is passed through a polarisation controller to obtain the optimal polarisation before it is injected into the microresonator waveguide using a lensed fibre. The pump wavelength is swept over a wavelength range from the blue-detuned position of the TE_{00} resonance to the red-detuned position of the TE_{10} mode. A lensed fibre is also used to collect the output from the microresonator. The light is then split with 10% sent to an OSA to record the comb spectrum. The remaining 90% is further split, with one branch going through a fibre Bragg grating (FBG) which suppresses wavelengths around the pump wavelength, removing the pump power and allowing the accurate measurement of the comb power. The other branch is then passed through a tunable band-pass filter (BPF) in order to isolate single comb lines, which is combined with light from another TSL at the same wavelength. The resultant beat note is then recorded on an ESA after the light is incident on a photodiode, allowing noise characterisation to be performed. An octave-spanning microcomb has been achieved in our group with this method in an AlN ring resonator [73] using a Santec TSL-710 tunable laser with a linewidth on the order of 100 kHz. This demonstrated the reliability of the dual-mode scheme to generate and maintain stable soliton microcombs. It was then investigated if these results could be replicated with our group's surface-slotted lasers.

4.6.1 Comb Generation using Slotted Laser.

The same setup from Figure 4.19 was used but the TSL is replaced with a surface-slotted semiconductor laser from an array of 1000 μm cavity length devices centred around 1550 nm. Several devices were characterised in order to satisfy the necessary conditions. The pump laser must be able to cover the wavelength sweeping range with high SMSR and without mode-hopping, while maintaining adequate output power to the EDFA. Figure 4.20 shows the characterisation of the slotted laser that was chosen to be a pump source.

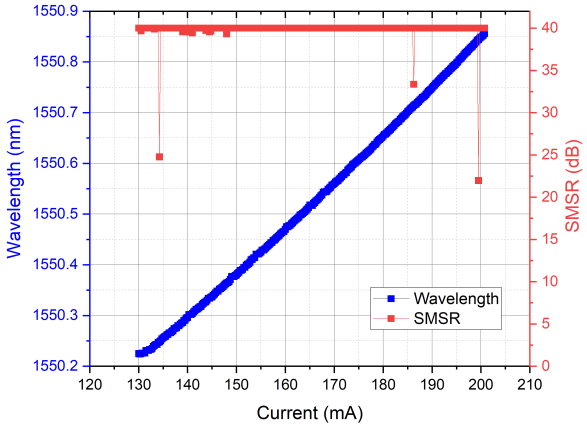

(a) Wavelength and SMSR vs injected current for 1000 μm slotted laser.

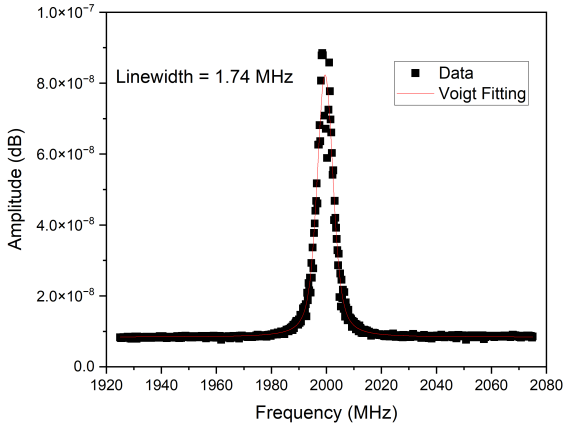

(b) Linewidth spectrum of slotted laser with gain current at 160 mA.

FIGURE 4.20: Wavelength sweep and linewidth spectrum of slotted laser.

By keeping the current to the gain section constant at 35 mA and the temperature constant at 14 ^{o}C using a cooling block, the current to the gain section of the laser could be increased using a current source controlled by a Python programme. As seen in Figure 4.20a, the red-shift in wavelength is linearly

proportional to the gain current. This allowed for the conversion between the current applied into the wavelength using a linear equation. A change in current of 1 mA was approximately equal to a change in wavelength of 0.009 nm. The linewidth of this device at a point towards the end of the tuning range was found to be 1.74 MHz, seen in Figure 4.20b, which is an order of magnitude greater than that of the TSL.
A slow sweeping method was employed where the gain current, and subsequently the wavelength, were increased over a timescale of several seconds. This was necessary to record the transmitted comb power vs gain current as this was limited by the speed of the Python programme used to collect the data. The transmitted power vs wavelength trace proved to be of vital importance when pumping with the slotted laser as it proved very difficult to obtain the correct polarisation of light. In the event that the soliton was not generated, it was necessary to adjust the paddles on the polarisation controller and record a comb power trace in order to gauge adjustments. Figure 4.21 is the transmitted power trace of a sweep where the soliton was successfully generated. The pump wavelength was outside of the range of the FBG and therefore the pump line and resulting power could not be removed from these measurements.

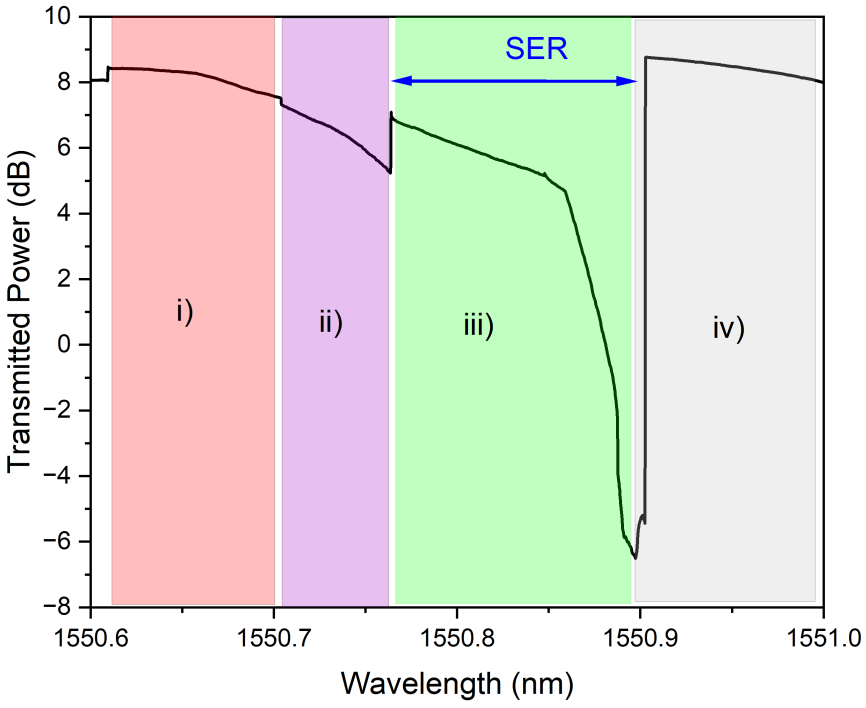

FIGURE 4.21: *Transmitted power vs pump wavelength on a sweep where a soliton state was achieved.*

Stage i) is the region where the primary comb is generated, corresponding to the spectra seen in Figure 4.22b. In stage ii) the modulation instability (MI) comb is generated, corresponding to the spectra seen in Figure 4.22c. In stage

iii), the soliton was generated at a wavelength of 1550.76 nm and remained stable after further detuning of 0.13 nm before annihilation in stage iv). This is the soliton existence range (SER).

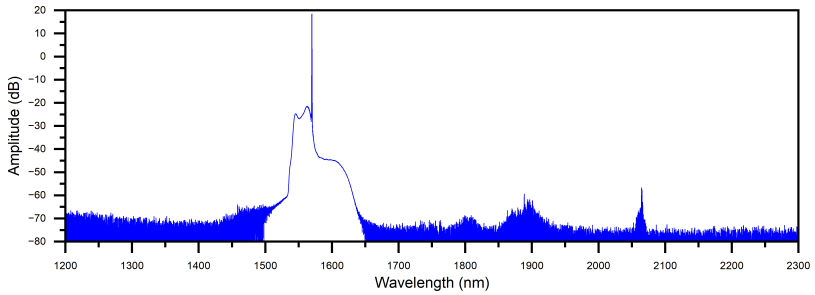

(a) Pump laser spectrum.

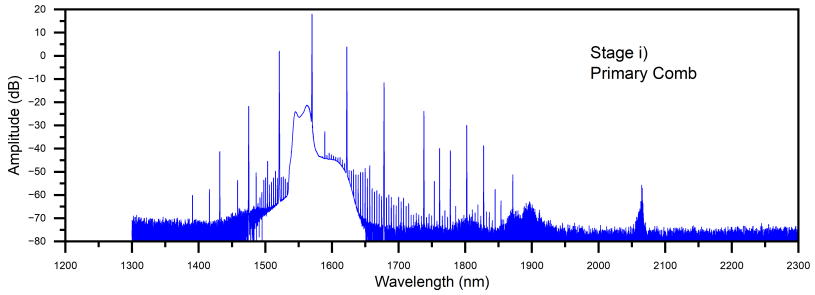

(b) Primary comb.

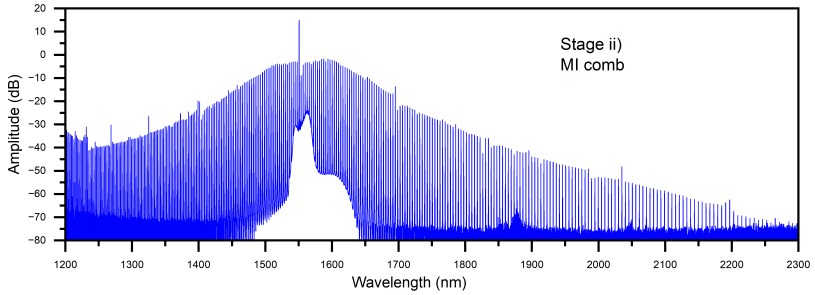

(c) MI comb.

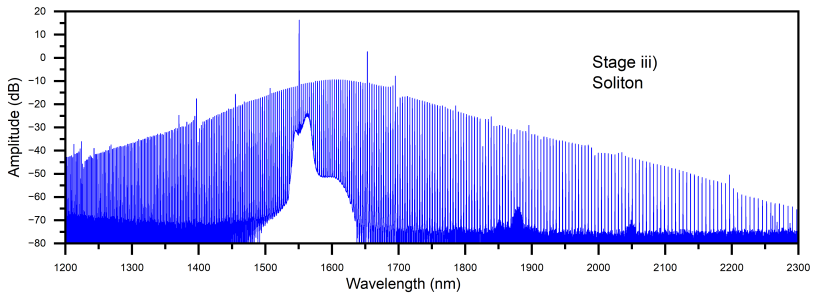

(d) Soliton.

FIGURE 4.22: Evolution of microcomb as wavelength is swept from blue to red.

Once the correct polarisation had been obtained, the soliton state was reliably generated several times and proved to be relatively stable. The soliton state remained for several minutes each time until perturbations around the lab such as doors opening or heavy footsteps caused it to vanish. This is most likely a result of the slotted laser being unpackaged and therefore more susceptible to perturbations in the environment. It was noted that movement near the bench where the laser was operating would often result in the destruction of the soliton. These issues would be minimised if the device were to be packaged or ultimately integrated onto the same chip as the resonator. This is a very promising result as an octave spanning soliton microcomb has been successfully generated with a chip-scale device that is highly suited for photonic integration, although the EDFA remains a necessity for the required power. Figure 4.23 shows that the comb spectrum is octave-spanning from approximately 1100 nm to over 2300 nm. These figures are a composite of spectra taken from two different OSAs as a single OSA was not available capable of recording the full span.

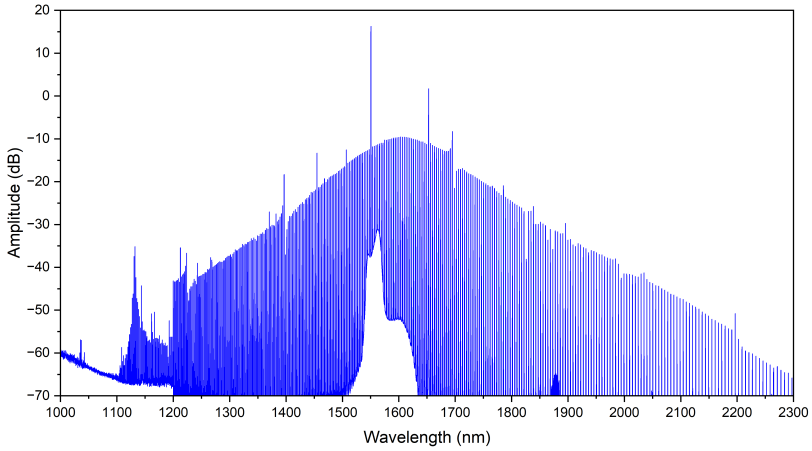

(a) Soliton generated by TSL.

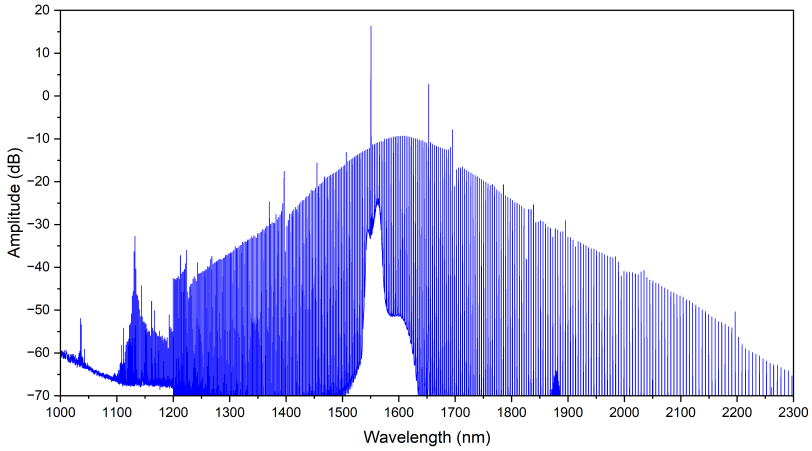

(b) Soliton generated by slotted laser.

FIGURE 4.23

The spectra are almost identical, when overlayed as in Figure 4.24, the only apparent difference is that the TSL spectrum has a lower noise floor. This is to be expected as the TSL has a much narrower linewidth compared to the slotted laser.

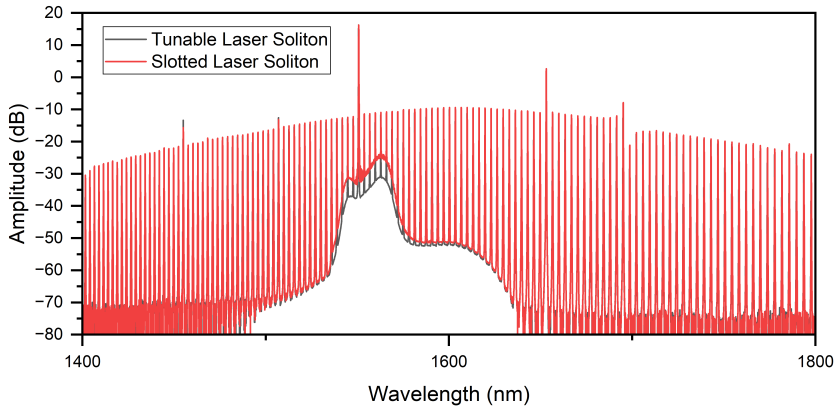

FIGURE 4.24: Spectra of soliton generated using TSL and soliton generated using a slotted laser zoomed in around the pump wavelength, demonstrating the difference in noise floor.

This can also be seen from the recorded RF noise of the the slotted laser comb vs the TSL comb. There is much higher low-frequency noise in the comb that was generated by the slotted laser.

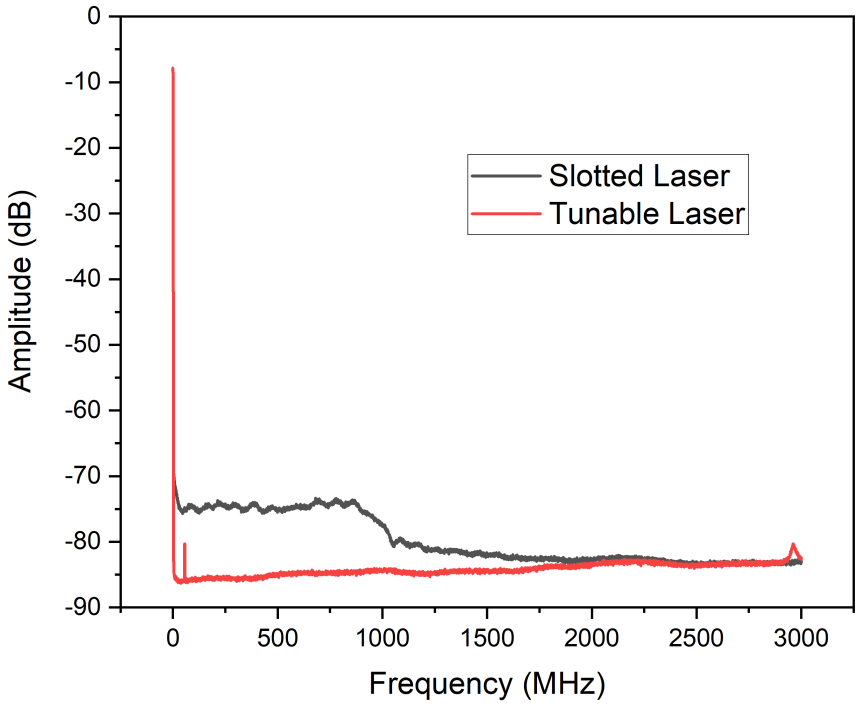

FIGURE 4.25: RF noise of soliton state.

The use of a simple single mode laser, albeit with an EDFA at present is a great result for the potential to integrate a pump laser and resonator for

broadband soliton comb generation. The demonstration of a very large soliton existence range compared with literature values shows that the dual-mode resonator scheme has much potential for applications. It is also possible to use a second pump laser such as those we developed at 1310 nm in conjunction with those at 1550 nm. Now this adds some complexity to the pumping arrangements but could also be investigated for further improvements in the soliton existence range.

Chapter 5

Turn-key Soliton Generation and Tunable Microwave Synthesis in Dual-Mode Microresonators

In this chapter, the results from pumping the microresonators with a Santec tunable semiconductor laser (TSL), a commercial packaged device and one of our unpackaged slotted lasers are presented. Previous work on microresonator pumping performed by our group [16], [17] has utilised a Santec TSL, with its output power boosted by an erbium-doped fibre amplifier (EDFA) as a pump source for microresonators. This system involves two bulky pieces of equipment, and the ultimate goal is to produce an integrated on-chip device for comb generation. To that end, a packaged semiconductor laser and one of our own slotted lasers are investigated as a pump source since these devices could be easily integrated with a microresonator.

5.1 Turn-key Generation

In the previous chapter, a dual-mode scheme was employed to generate an octave-spanning microcomb. This involved a linear sweep of the wavelength from the blue-detuning region to the red-tuning region. This sweep takes several seconds and the transmitted power is simultaneously recorded, allowing us to identify the soliton generation wavelength and the soliton existence range. It also aids in adjusting the polarisation of the pump laser. However, for practical applications, it would be preferable to generate the soliton microcomb quickly in a turn-key fashion. We therefore employ a step-tuning method where the current of our slotted laser is increased from the starting current to the stopping current in a single step. The tuning time is therefore limited by the response of the laser wavelength to the applied current.

5.1.1 Device Characterisation

A Si_3N_4 dual-mode microresonator with a radius of 60 μm was used to investigate turn-key operation. The transverse magnetic (TM) polarised transmission spectrum is shown in Figure 5.1 where the FSR of the fundamental TM modes (TM_{00}) is 384.62 and the FSR of the first-order TM modes (TM_{10}) is 378.89 GHz. There is a crossover of these modes, a result of the differing

FSR of each mode family, occurring around 1570 nm (marked by the blue rectangle). The resonator is pumped near this wavelength with TM_{00} being the pump mode and the TM_{10} mode is the auxiliary mode which is on the red-detuned side of the pump mode and is used for stabilisation of the soliton.

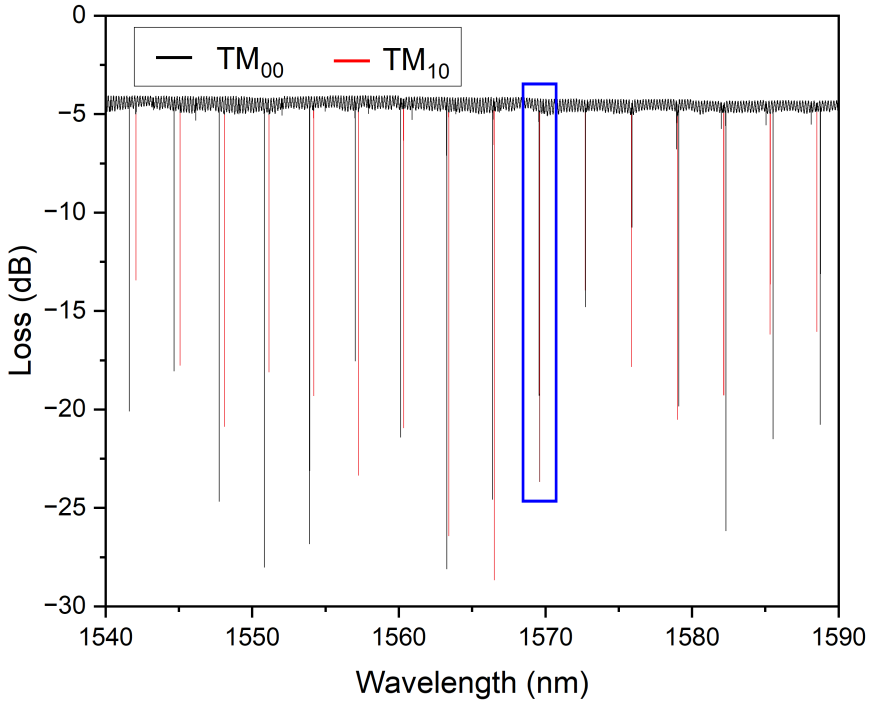

FIGURE 5.1: *Transmission spectrum of transverse magnetic modes in a Si_3N_4 resonator. A blue rectangle highlights the dual-modes used for pumping. Data recorded by Dr Hai-Zhong Weng.*

A zoomed image of the dual-modes is shown in Figure 5.2 showing the spacing of approximately 6.3 GHz and a linewidth of 0.29 GHz and 0.71 GHz of the TM_{00} resonance and the TM_{10} resonance, respectively.

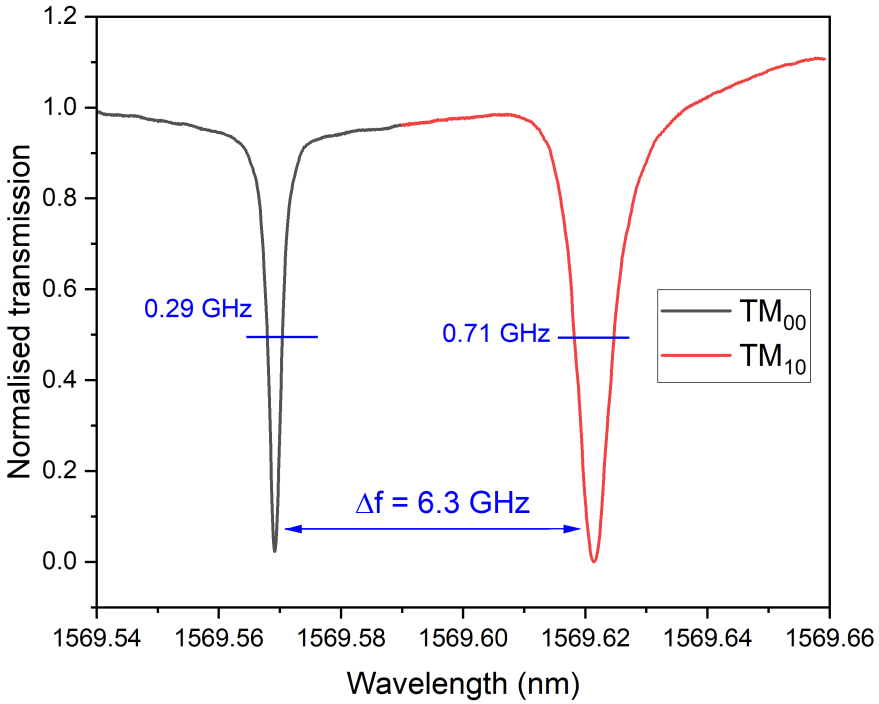

FIGURE 5.2: *Dual resonance modes near 1570 nm with a spacing of 0.053 nm or 6.3 GHz.*

The simulated integrated dispersion D_{int} in Figure 5.3 shows good agreement with the experimentally measured results obtained for 50 resonance modes which were measured. The dispersion is plotted against the mode number μ relative to the pump resonance. Meaning that $\mu = 0$ corresponds to the TM_{00} mode near 1570 nm and negative values are the modes which are blue-shifted relative to this mode.

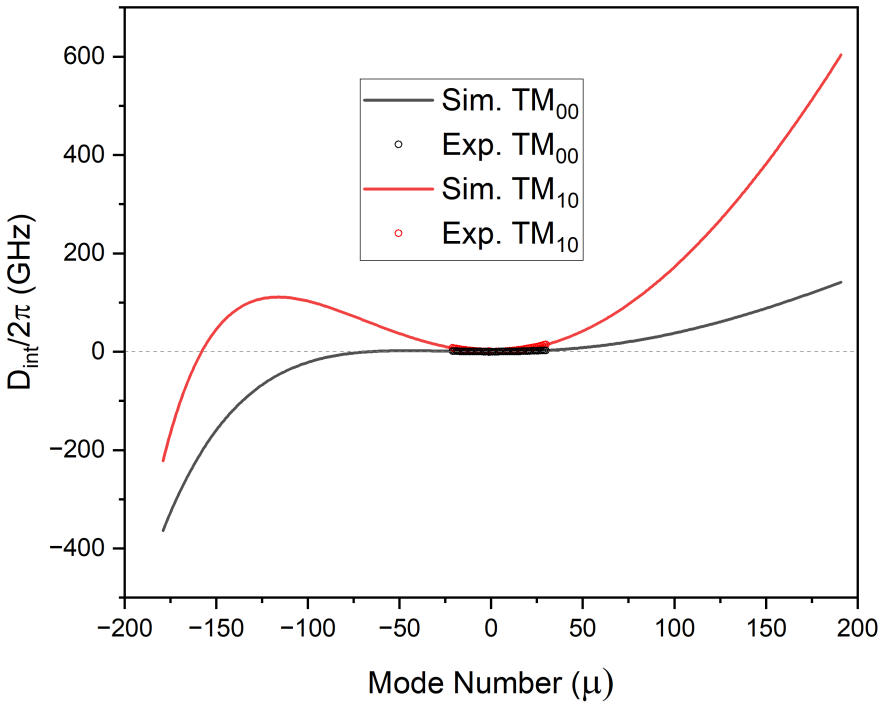

FIGURE 5.3: *Simulation of integrated dispersion and 50 experimentally measured resonances versus mode number relative to the TM_{00} mode. The TM_{10} mode exhibits stronger anomalous dispersion that then the TM_{00} case. Data recorded by Dr Hai-Zhong Weng.*

The TM_{00} mode was shown to have near ideal anomalous dispersion with a second-order dispersion coefficient of 5 MHz. The auxiliary TM_{10} was found to have a dispersion coefficient of 33 MHz.

5.1.2 Turn-key Soliton Generation

The soliton was first generated using slow-tuning by tuning the wavelength of the TSL was swept from 1570.00 nm to 1570.90 and the evolution of the generated microcomb can be seen in Figure 5.4.

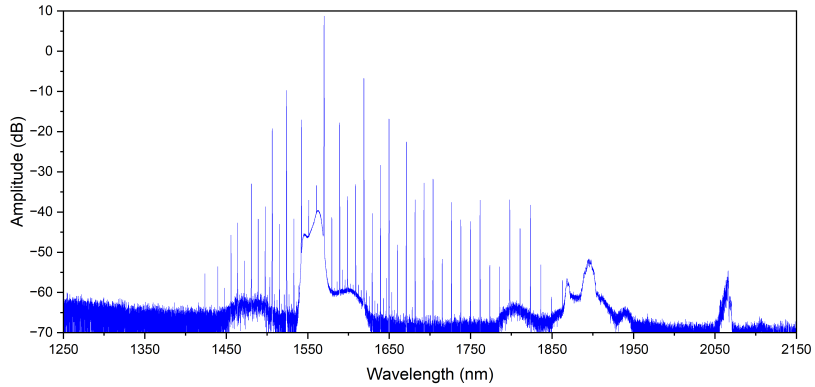

(a) TM_{00} *primary comb.* λ_{pump} = *1570.15 nm*

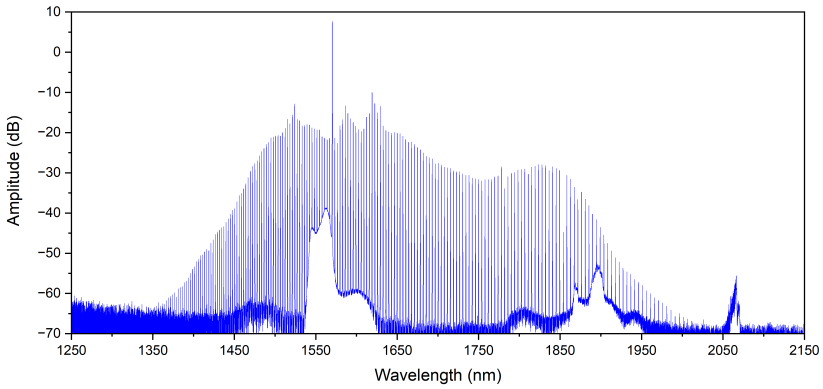

(b) TM_{00} *MI comb.* λ_{pump} = *1570.38 nm*

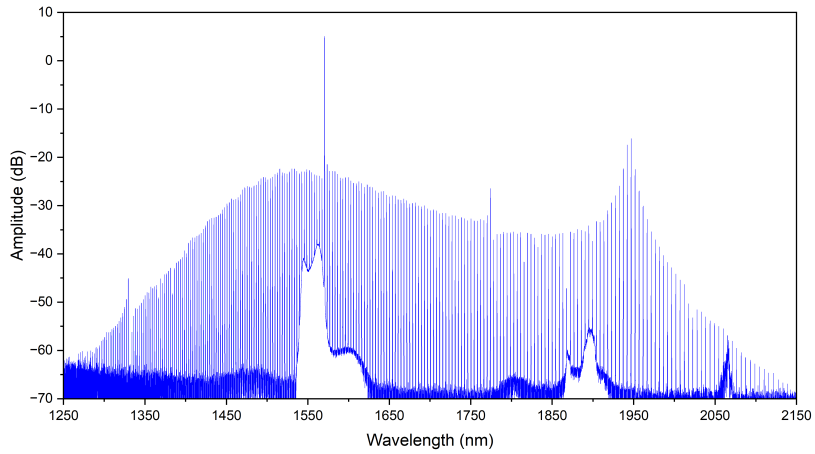

(c) TM_{00} *soliton.* λ_{pump} = *1570.60 nm*

FIGURE 5.4: Evolution of comb as TSL wavelength is swept.

This allowed us to determine the wavelength where the soliton step would be generated. The comb power was recorded as the wavelength was swept and is shown in Figure 5.5.

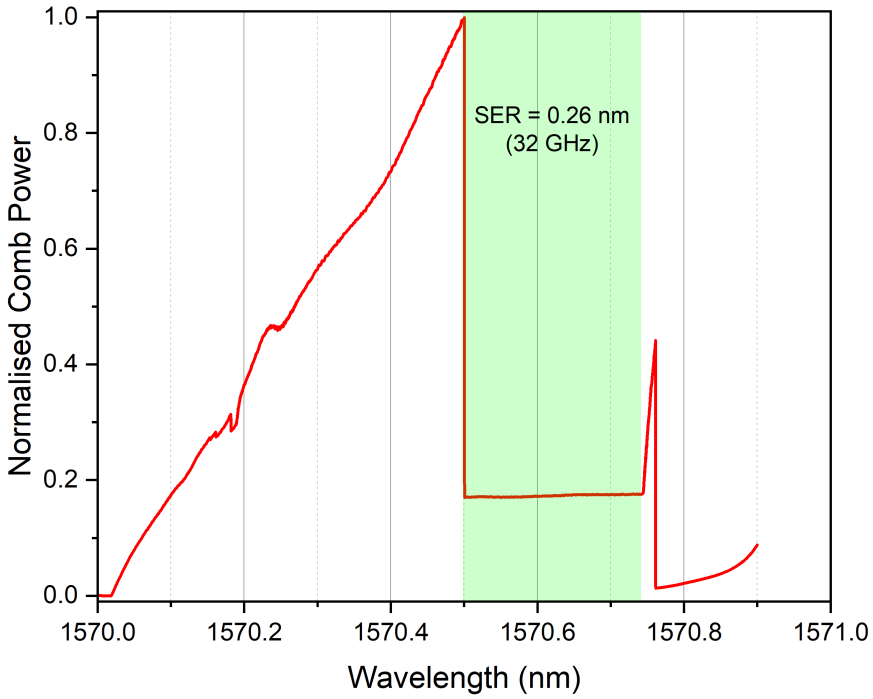

FIGURE 5.5: *Comb power trace while scanning wavelength of TSL pump laser.*

The soliton was generated at a wavelength of 1570.50 nm and remained stable as the wavelength was detuned until it disappeared at 1570.76 nm. This corresponds to a soliton existence range of 0.26 nm or 32 GHz when using the TSL.

A slotted laser was then used to pump the same resonator. A 1000 μm long, two-section, single-period slotted laser was used and the wavelength was tuned by increasing the gain current while the reflector current and temperature remained constant. Slow-tuning was again used initially in order to determine the soliton step wavelength as well as the correct polarisation for the light. Figure 5.6a shows the linear relationship between the injected current as it is swept and the resulting wavelength. This relationship was then used to convert between the applied current and the laser wavelength.

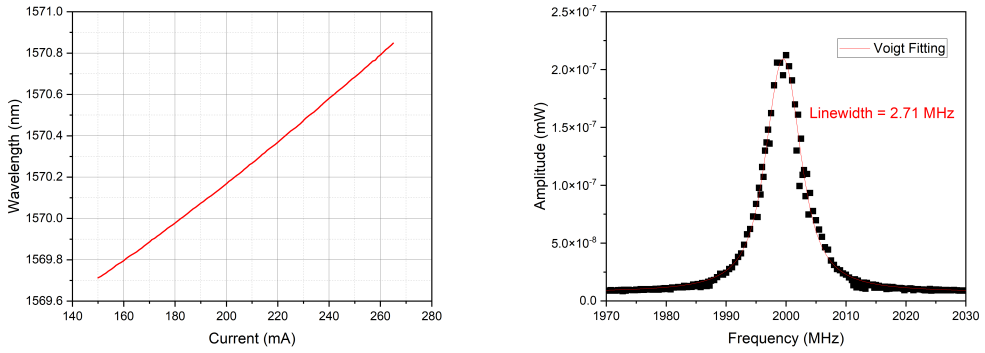

(a) . (b)

FIGURE 5.6: *a) Output wavelength vs current injected into gain section of slotted semiconductor laser at an ambient temperature of 31 ^{o}C and a constant reflector current of 145 mA. b) Linewidth spectrum of slotted pump laser when gain current is 220 mA.*

Figure 5.7 shows the comb power trace when pumping with the slotted laser and was recorded by the Python programme measuring the change in comb power as more current was supplied to the gain section.

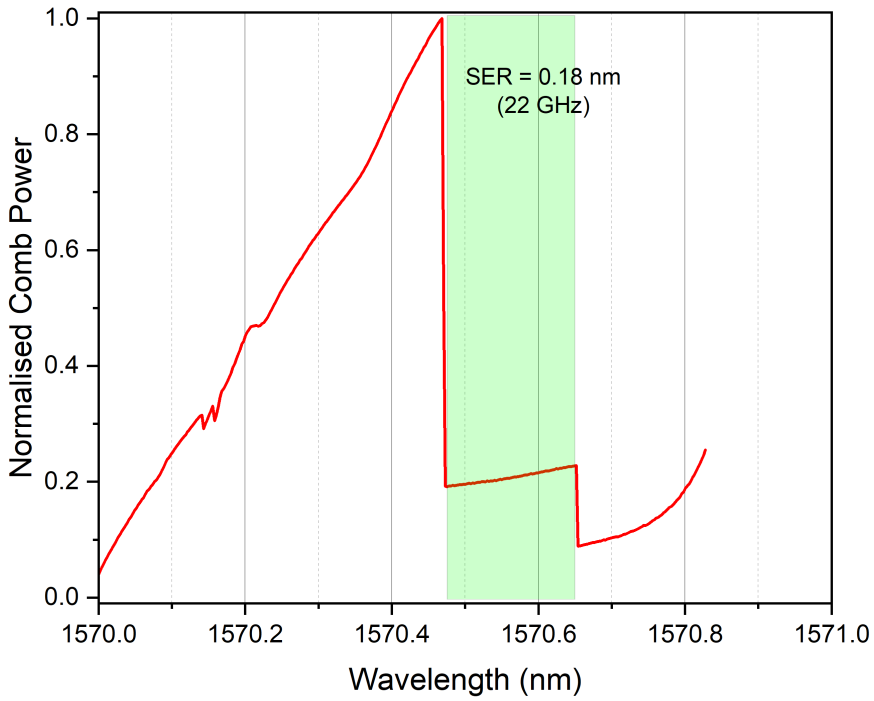

FIGURE 5.7: *Comb power trace while scanning the wavelength of the slotted pump laser.*

The SER was found to be from 1570.47 nm to 1570.65 nm. A range of 0.18 nm or 22 GHz. This is significantly less than the soliton generated using the TSL.

Soliton generation was once gain found to be more difficult using a slotted laser compared with the TSL, likely due to several factors. While the spectral linewidth of the Santec TSL-710 is 100 kHz, the recorded linewidth of the slotted laser as shown in Figure 5.6b is 2.71 MHz, twenty times broader. The slotted laser also proved to have less wavelength stability and the polarisation controllers had to be adjusted very finely to obtain the optimal polarisation of the light injected into the resonator. Despite this, the soliton was shown to be reliably generated once the polarisation was found and the system was unperturbed.
Figure 5.8 shows the soliton generated in the same resonator by sweeping the slotted laser wavelength from 1570.00 nm to 1570.83 nm over several seconds.

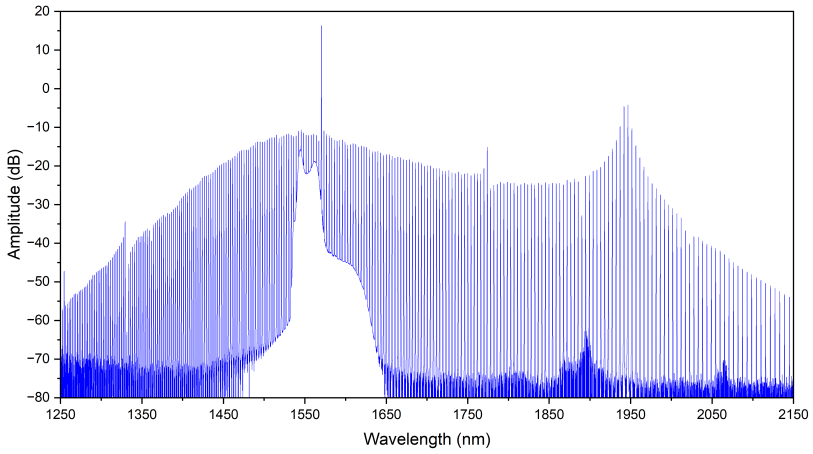

FIGURE 5.8: *TM_{00} soliton. λ_{pump} = 1570.60 nm with slotted laser and EDFA.*

It is clear that the noise floor near the pump wavelength of the slotted laser soliton is much higher than that seen when the soliton is generated by the TSL in Figure 5.4c. This is clearly illustrated when the spectra near the pump are compared in Figure 5.9.

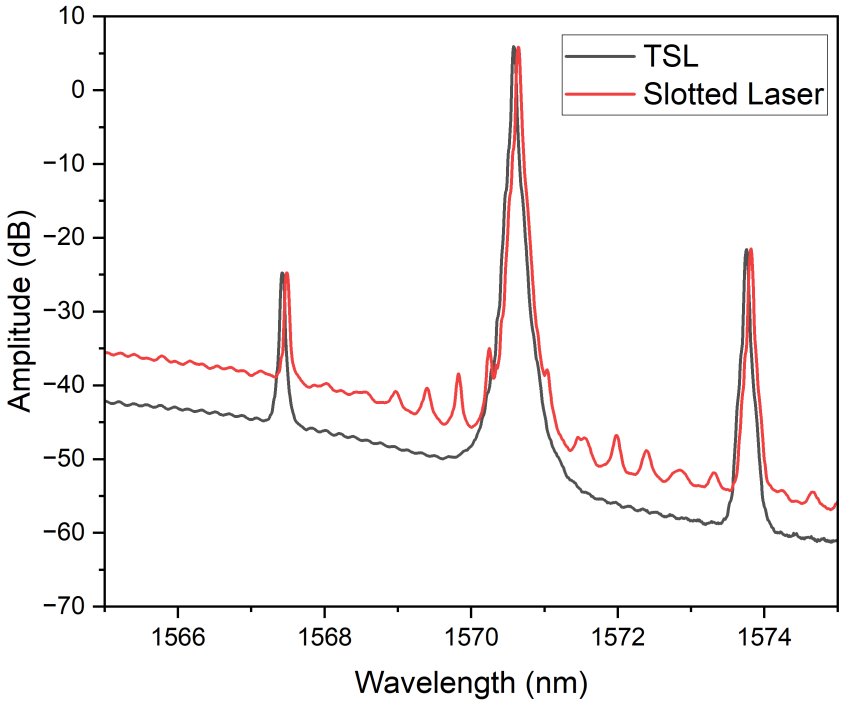

FIGURE 5.9: Soliton spectra around the pump wavelength.

The noise floor of the slotted laser is almost 10 dB higher compared to the TSL and there are several side modes visible in the slotted laser spectrum. To demonstrate turn-key generation of the soliton state, the current into the gain section is increased from the starting current to the stopping current in a single step. In order to step-tune the slotted laser, the current source was connected to an arbitrary waveform generator (AWG) in order to modulate the current. Figure 5.10 shows the experimental setup for turn-key generation.

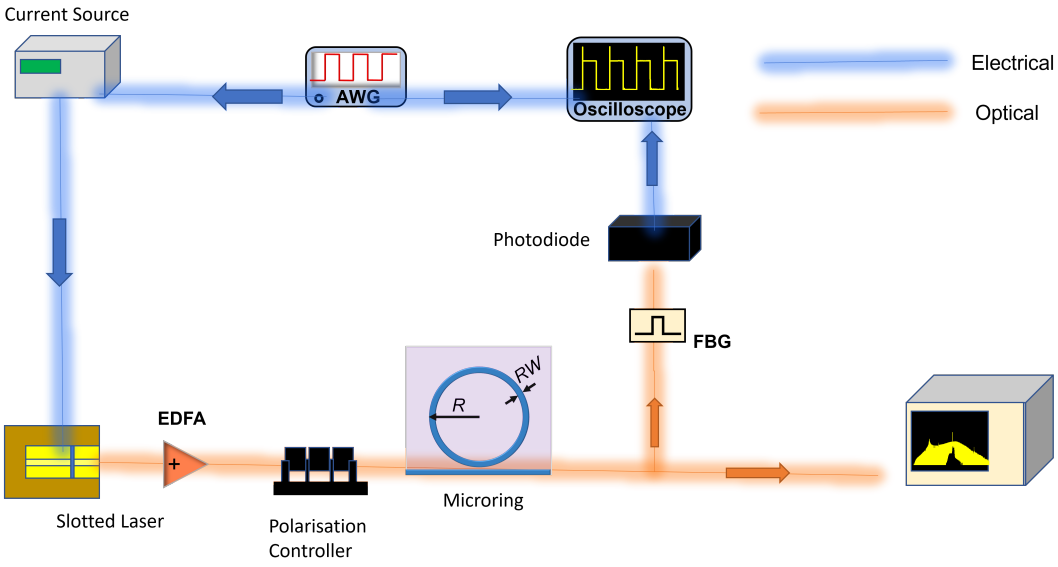

FIGURE 5.10: Experimental setup for turn-key generation of soliton microcomb using a slotted laser as a pump source.

Using the Python programming language, a programme was written to construct an arbitrary waveform given the start current, stop current, time scale and wave shape that was then transmitted to the AWG, which in turn applied it to the current source. The AWG is also connected to an oscilloscope so that the waveform and comb power trace can be recorded simultaneously. The light from the laser facet is collected by a lensed fibre and is then passed through a fibre polarisation controller (FPC). The light is then coupled into the input waveguide of the microresonator with a lensed fibre while another lensed fibre collects the light at the output. The beam is then split, with a portion of the light collected by the OSA where the spectrum is recorded. The rest passes through a fibre Bragg grating (FBG) which reflects wavelengths around the pump wavelength, thus excluding the pump power and allowing us to record the comb power. This comb power is incident upon a photodiode allowing us to record the comb power trace on the oscilloscope along with the the AWG waveform.
To determine the optimal stopping current I_{stop} for soliton generation, 160 mA was chosen as a starting current and then multiple steps were initiated, terminating at a range of stop currents. Figure 5.11 shows the evolution of the soliton generation with the stop current.

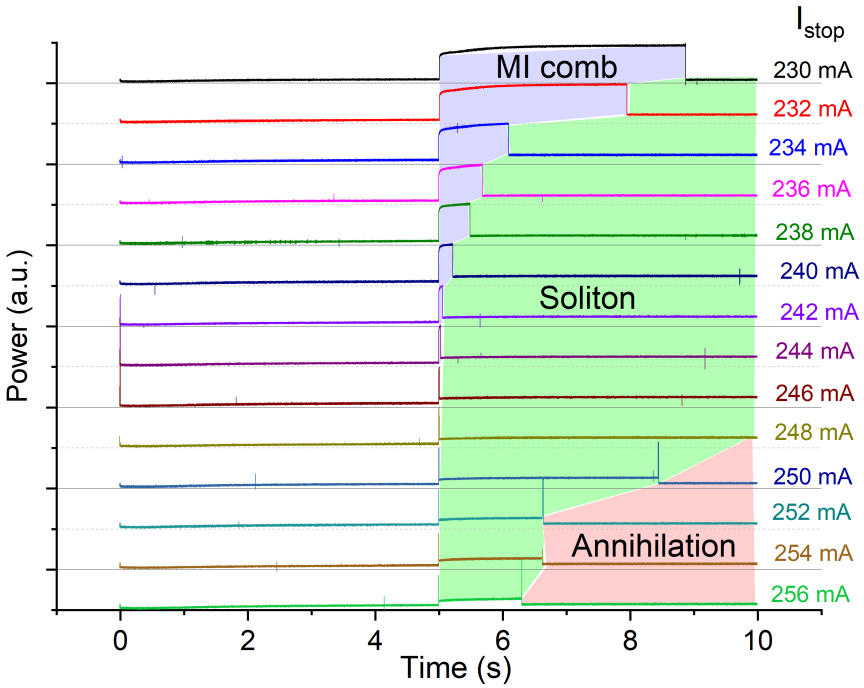

FIGURE 5.11: *Comb power traces at different stopping currents. Start current is 160 mA in each case.*

We can see that for the lower stop currents an MI comb is first generated and exists on the order of seconds before the soliton is formed. As the stop current was increased, the existence time of the the MI comb stage began to decrease until at higher stop currents the soliton was "annihilated". i.e. the wavelength detuning was too great for soliton generation to occur. We believe this is related to the wavelength settling time and the size of the current step. Although the wavelength settling time for a semiconductor laser is limited by thermal effects, these processes occur on the order of microseconds, not seconds as witnessed here. It is likely that the system of an unpackaged device where the ambient temperature is controlled by a TEC connected to a large cooling block, the settling time is further limited by the response time of the equipment. Figure 5.12 illustrates a potential explanation.

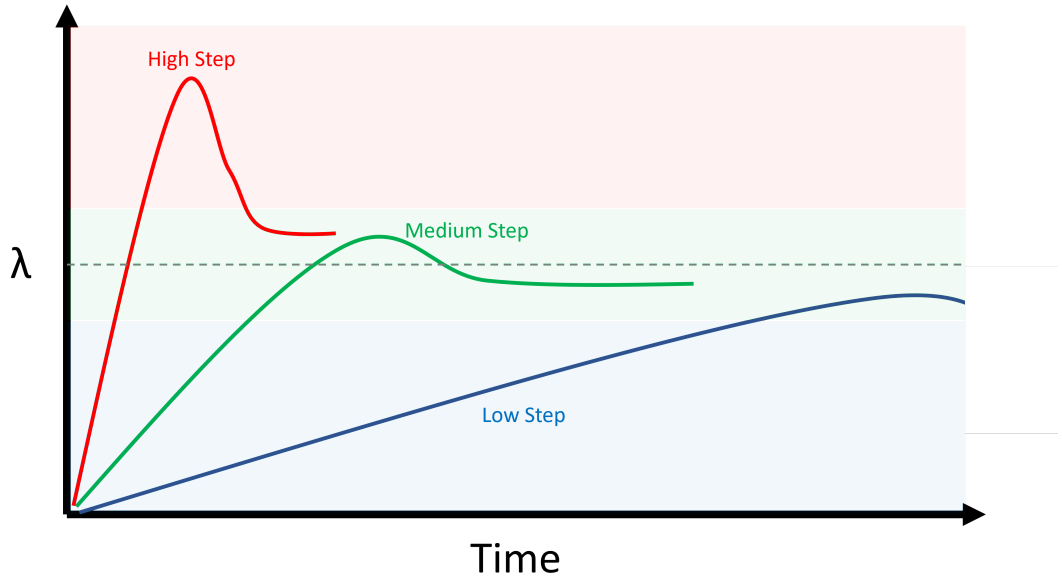

FIGURE 5.12: *Schematic indicating the proposed wavelength settling behaviour depending on the current step size. The dashed line represents the ideal soliton generation wavelength. The red line represents the proposed behaviour of a large current step, the green line is a moderate current step, and the blue line is a low current step. The blue, green and red shaded regions correspond to the MI comb state, soliton existence range, and the annihilated state as in Figure 5.11.*

When the current step size is large, I_{stop} = 256 mA, the wavelength begins to increase quickly, overshooting the soliton existence range before settling. The soliton may be generated briefly but the detuning quickly becomes too large and the soliton is annihilated. With a moderate step size, I_{stop} = 244 mA, the wavelength increase and settles well within the soliton existence range and the soliton is generated in a turn-key fashion. For the smallest step sizes, I_{stop} = 230 mA, the wavelength increases relatively slowly, taking several seconds before reaching the soliton existence range and explaining why the MI comb state is so prolonged at these stopping currents. The shape of the current modulation waveform can potentially be utilised to minimise the effects of wavelength drift. More complex waveforms such as a three-segment current ramp [74] and a double current-step [**doublestep**] have been utilised to great effect in compensating for wavelength drift and thermal instability in order to improve soliton generation. The Python code was developed to be able to apply such waveforms in our pumping experiments, however we only managed to successfully generate solitons with the simple step function.
Figure 5.13b shows an example of a simple step function generated by the Python programme beginning at a current of 160 mA, stopping at 246 mA and remaining at this current for 5 seconds before the waveform repeated and Figure 5.13a shows the resulting trace recorded by the real-time oscilloscope.

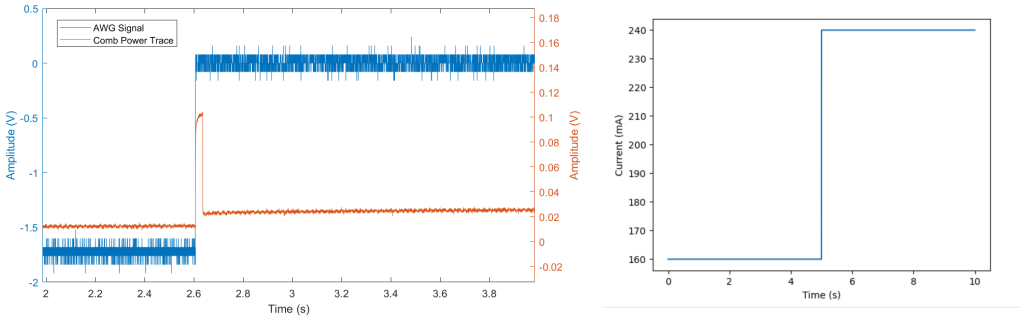

(a) (b)

FIGURE 5.13: *a) Comb power trace and AWG signal during step tuning from 160 mA to 246 mA. b) Step function generated from Python programme.*

The soliton step can be clearly seen shortly after the AWG signal is sent. To show the reliability of the soliton generation, the step tuning was performed twenty times in succession by allowing the waveform to repeat. This is shown in Figure 5.14 where the soliton was successfully generated nineteen times in a row. It was separately found that the soliton state generated in this way would last for several minutes after the waveform had terminated.

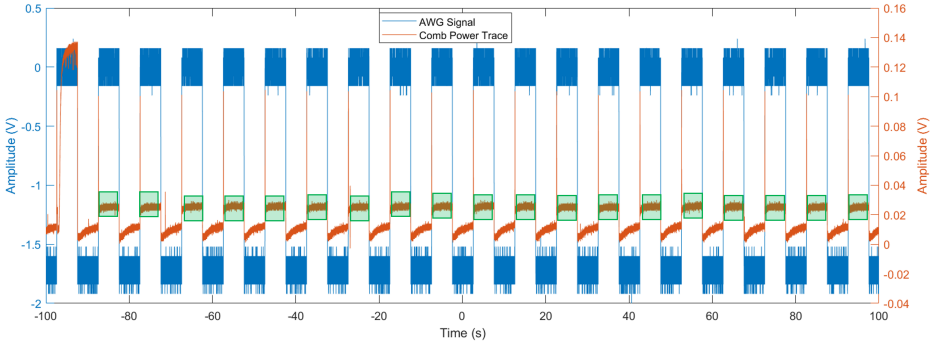

FIGURE 5.14: *Repeated step tuning with successful soliton steps highlighted in green.*

It was separately found that the soliton state generated in this way would remain stable for several minutes after the waveform had terminated.

5.2 Microwave Generation in Dual-Microcomb

Another application of soliton microcombs has been the generation of low-noise microwaves [75]. The oscillation frequency of the wave is dependent on the f_{rep} of the soliton, which is determined by the size of the resonator. This would imply a relatively large resonator would be required to generate signals of a frequency that is detectable by conventional electronics. Multiple solitons can be excited in a resonator and their correlated beat note can be obtained for sensing [76], however the repetition rate between coexisting

solitons is quite small and this beat note is typically below 1 GHz, making it unsuitable for microwave photonics. By generating a dual-comb consisting of a single soliton and a primary comb, we can obtain beat notes in the range of 20 GHz to 40 GHz.
A second resonator with the same dimensions used to demonstrate turn-key operation was used for microwave generation. This resonator, however, features dual TM_{00} and TM_{10} modes near 1567 nm with a smaller separation of 4.9 GHz. This separation was found to be sufficient for generating dual-combs and multiple-solitons (MS). By sweeping the TSL with a speed of 1 nm/s with various pump powers, the evolution of the resulting comb with increasing power was demonstrated in Figure 5.15.

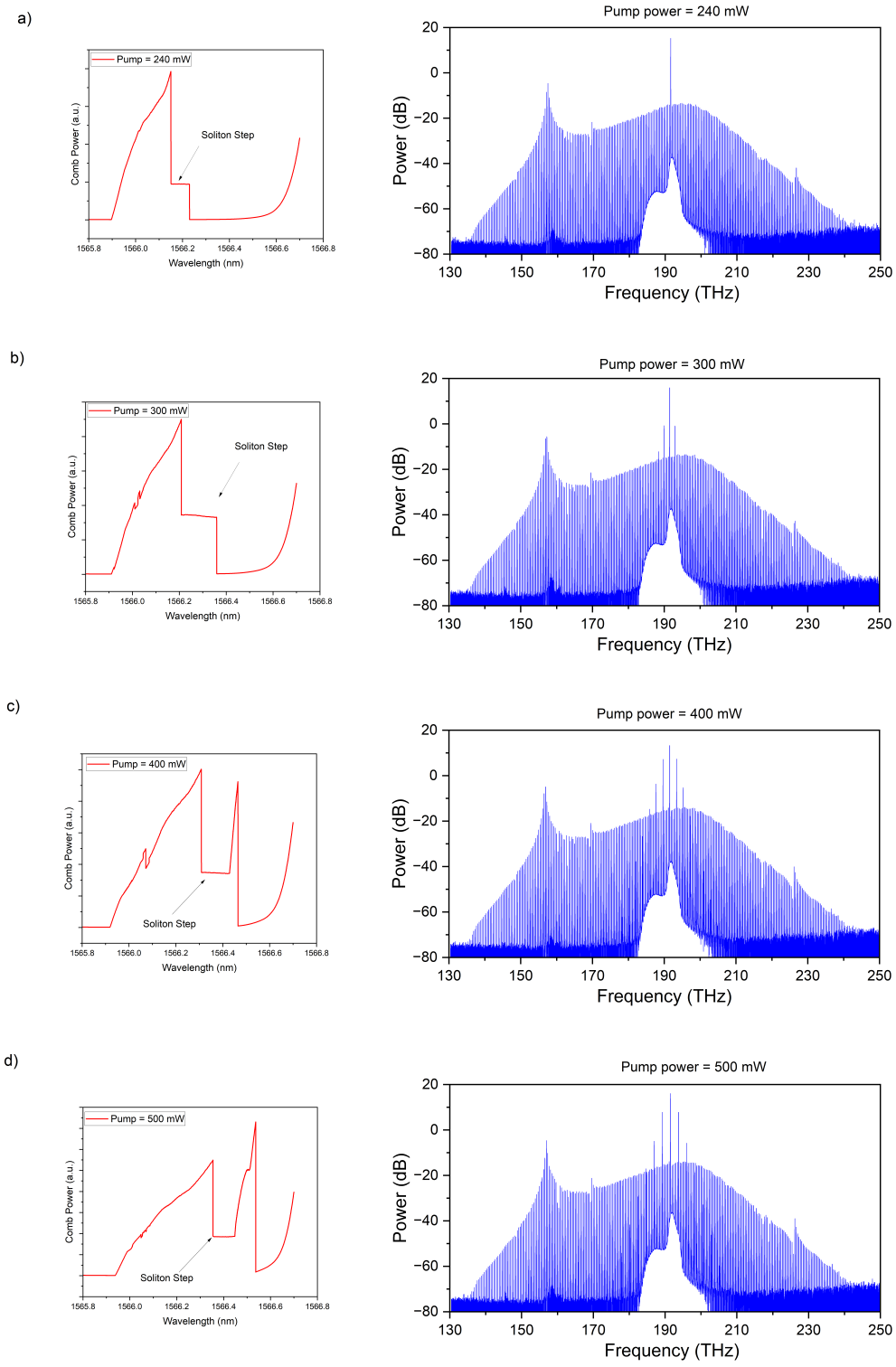

FIGURE 5.15: Comb power trace and corresponding optical spectra when the pump power is a) 240 mW. b) 300 mW. c) 400 mW. d) 500 mW

With a pump power of 240 mW, a single soliton (SS) is reliably generated. When the power is increased between 300 mW and 500 mW, a dual comb is

realised consisting of the SS and the primary comb of the TM_{10} mode. Once the TM_{10} primary comb has been generated along with the SS, the pump power was adjusted in order to tune the line spacing of the primary comb. Figure 5.16 shows the dual-comb spectra around the pump wavelength overlayed with the SS generated with a pump power of 240 mW. It is demonstrated how the primary comb-line spacing can be tuned such that it lines up with the modes of the SS beginning with the modes 4 FSR spacings away from the pump wavelength, denoted by $\mu = 4$, and increasing to $\mu = 5$ and $\mu = 6$ at pump powers of 400 mW and 500 mW, respectively.

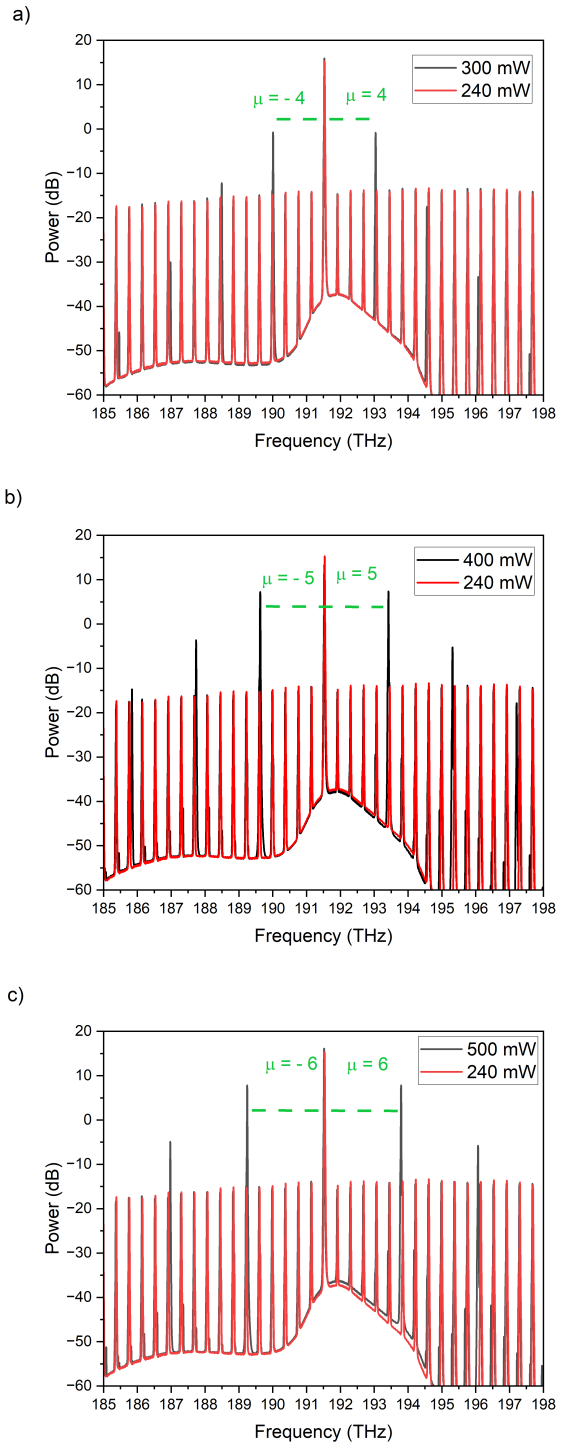

FIGURE 5.16: *Primary comb line-spacing adjusted to coincide with soliton modes.*

Figure 5.17 shows the experimental setup for microwave generation.

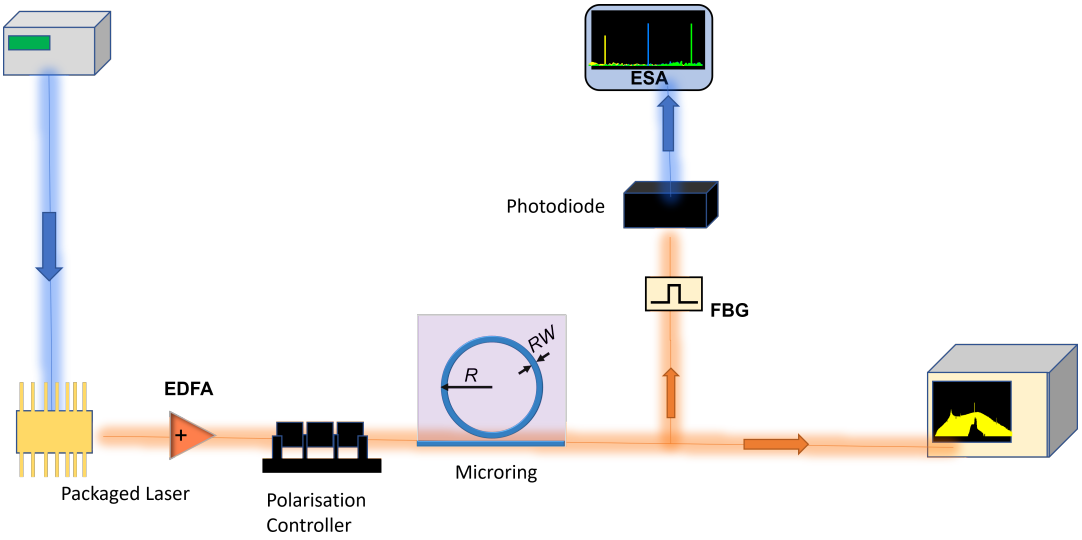

FIGURE 5.17: Experimental setup for dual-comb generation and microwave frequency generation.

A band-pass filter is used to isolate the comb lines belonging to the SS and primary comb and the beat note is detected by a photodiode. The beat notes obtained with the first sidebands of the primary comb from a dual-comb generated by a TSL as a pump for the modes at $\mu = 4, 5, 6$ are shown in Figure 5.18.

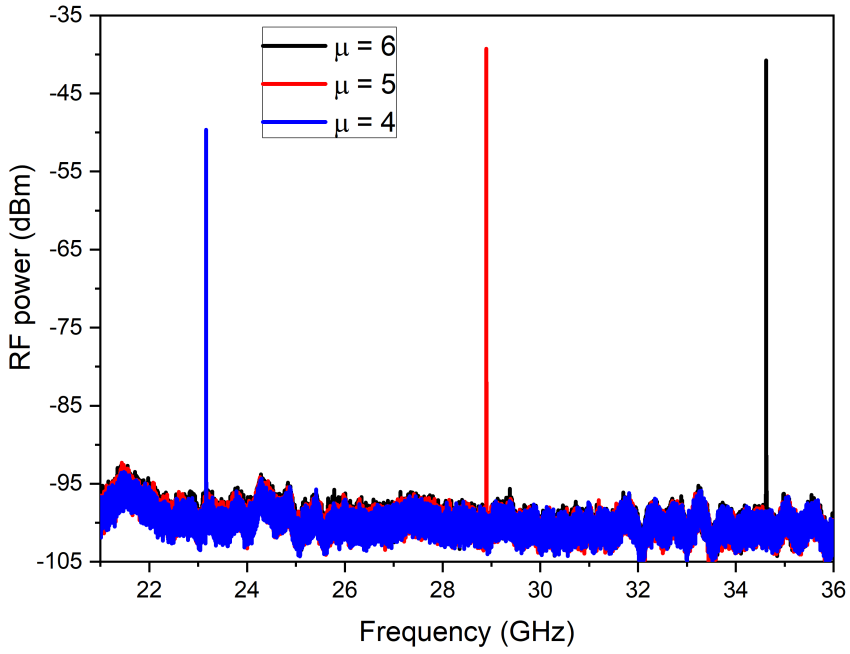

FIGURE 5.18: *Frequencies obtained from beating primary comb lines with corresponding soliton modes.*

The signals generated from these beat notes are at 23.4 GHz, 28.9 GHz and 34.6 GHz. These fall within the K and K_a bands, which is the portion of the electromagnetic spectrum which is used for uplinking to communication satellites as well as high-resolution radar imaging. The harmonics of these beat notes should also be detectable with a higher-speed photodiode than we have available. Higher frequencies could also potentially be generated using the second and third sidebands of the primary comb. The separation between the second sideband modes and the corresponding soliton modes ($\mu = 8, 10, 12$) are 46.8 GHz, 57.8 GHz, and 69.2 GHz which have applications in wireless communication. Similarly, the third sideband modes corresponding to the soliton modes ($\mu = 12, 15, 18$) would yield frequencies of 70 GHz - 100 GHz, meaning the system could operate as a discretely tunable millimetre oscillator.

5.2.1 Commercial Semiconductor Laser

A commercial semiconductor laser in a butterfly package was used to generate the dual-comb. A single injection current was used for wavelength control and the temperature could also be varied by supplying current to the pins connected to the in-built TEC. Figure 5.19a shows the wavelength tuning range possible by varying both temperature and current. The SMSR was above 40 dB for the entire tuning range and an example of the output spectrum is seen in Figure 5.19b.

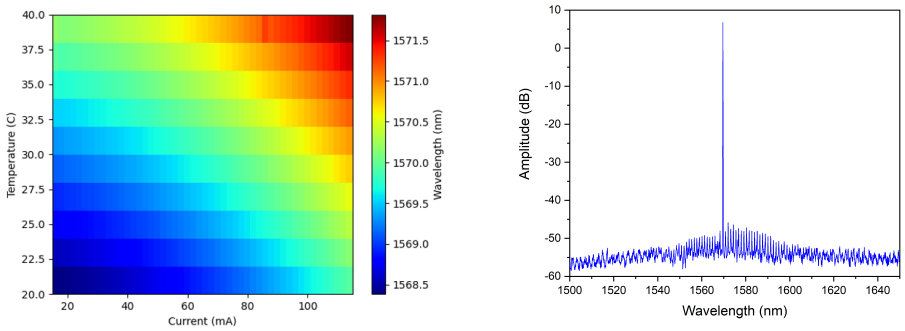

(a) (b)

FIGURE 5.19: *a) Wavelength tuning spectrum of packaged device. Output spectrum of packaged device.*

It was assumed that the packaged device would have greater wavelength stability due to being wire-bonded and also having a much smaller TEC. However, generating and maintaining the soliton state proved difficult just as with the unpackaged slotted laser. The same procedure was followed as with the TSL and a dual-comb was successfully generated and the frequencies at 28.9 GHz and 34.6 GHz were successfully generated. A comparison between the beat note produced with the TSL-generated comb and the beat note produced with the packaged device-generated comb is seen in Figure 5.20.

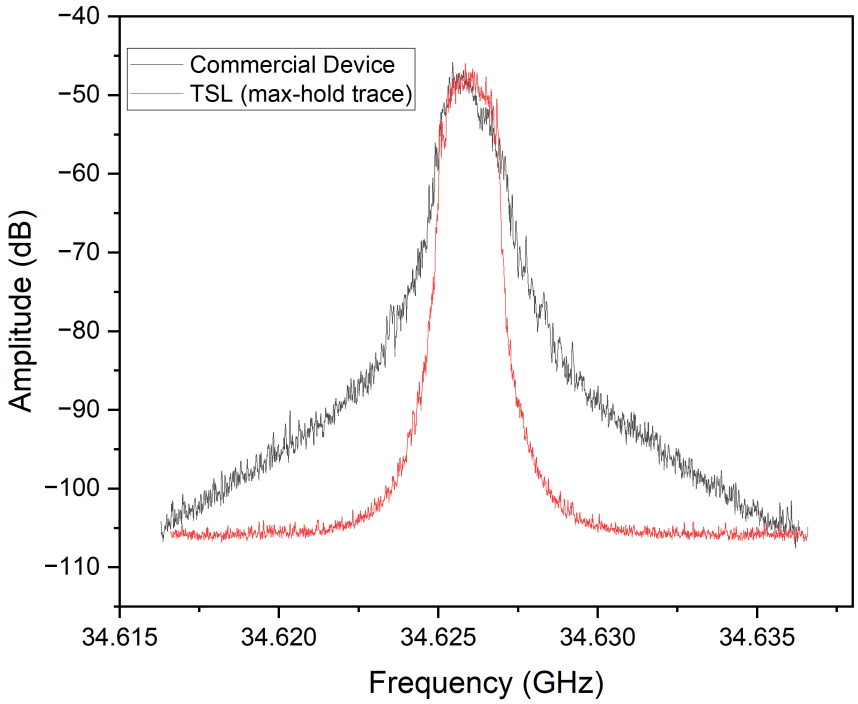

FIGURE 5.20: *Beat note at 34 GHz from comb generated with a packaged semiconductor laser and the max-hold of the beat note at 34 GHz from the TSL comb.*

There was significant jitter of the beat note generated using the TSL and therefore the max-hold amplitude of the signal was recorded. We can see that the beat note generated with the packaged device is much broader than the beat note generated with the TSL. This demonstrates again that the coherence of the pump source will have an effect on the coherence of the generated signals.

The phase noise of the microwave signals generated using both the packaged device and TSL were recorded using an in-built measurement system on the ESA (R&S FSV3-K40) and is shown in Figure 5.21.

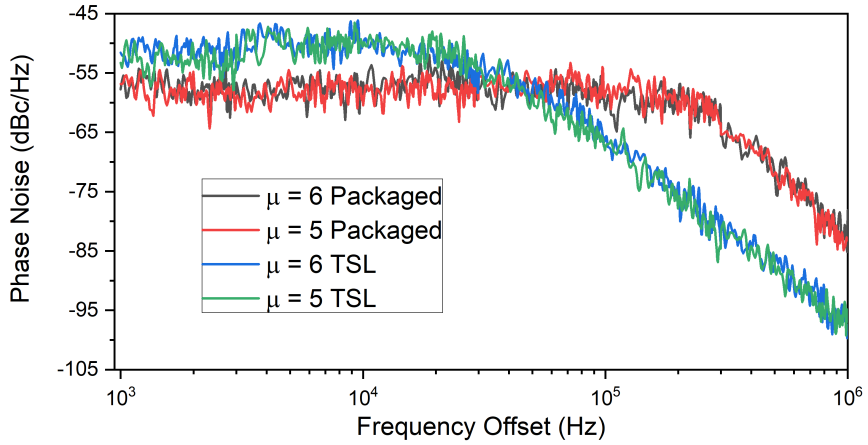

FIGURE 5.21: *Phase noise comparison between beat notes generated by packaged semiconductor laser and beat notes generated by TSL.*

The beat note from the TSL comb was found to have significant jitter, and therefore the max-hold of the RF spectrum was recorded. Considering the solitons are thermally locked and have a much lower noise [77], the jitter is most likely mainly due to the primary comb. The beat note from the packaged device comb is broader than even the max-hold of the TSL. The phase noise also shows that the noise due to the packaged device is significantly greater at offset frequencies above 100 kHz. Therefore, while the frequencies were successfully generated with the packaged device, the result is much noisier than the TSL. It is clear that the linewidth and noise of the pump laser has a significant effect on the quality of the signals generated from the resonator. It is therefore necessary that the lasers we develop with the hopes of future integration with microresonators for chip-scale frequency synthesis must not only have sufficient power and wavelength tunability, but also coherence.

Chapter 6

Conclusions and Future Work

6.1 Conclusions

The concept of optical frequency combs and their potential applications in optical communications, sensing, metrology and frequency synthesis was introduced. It was noted, though, due to the size and environmental susceptibility of current benchtop systems, this technology is not yet suitable for practical applications. However, numerous recent advances in microresonator frequency combs has demonstrated great potential for miniaturising the entire system. Recent work was discussed where microring resonators were able to produce highly stable soliton frequency combs which span an octave, allowing for the $f - 2f$ frequency self-referencing scheme to be employed. Previously in our group, we have demonstrated octave-spanning soliton frequency combs using a commercial tunable semiconductor laser. We suggest that this system can be further miniaturised down to chip-scale if the TSL pump laser could be replaced with one of our surface-slotted semiconductor lasers.
In Chapter 2, the background theory of semiconductor lasers is explored as well as the principals on which our group's slotted lasers are based. The design process for arrays of semiconductor lasers based on slots for optical communication is outlined. The optimisation of the slot parameters to suppress side and FSR modes is discussed as well as the integration of semiconductor optical amplifiers in order to boost the output power. Hybrid square-rectangular lasers (HSRLs) were also introduced, these demonstrate dual-lasing and it was hoped that they could be used to successfully pump two resonance modes simultaneously. The origin and importance of noise in semiconductor lasers is also discussed.
In Chapter 3, a full array of slotted lasers is characterised. These arrays are each based on a different set of slot parameters and are contrasted in order to determine which design performs best and should be incorporated into future fabrication runs. The wavelength tunability, SMSR, output power and linewidth were all contrasted. The array based on non-uniform slots performed the best as it most effectively suppressed FSR modes while still yielding the most uniform performance between devices on the same array. A thermal wavelength tuning range of over 40 nm across the 12 devices on the non-uniform array, as well as output power of over 30 mW, was demonstrated. This output power would not be enough to eliminate the need for the

EDFA when pumping the resonators we can currently fabricate. The HSRLs were characterised but were found to be unsuitable for the application as the output power was very low and there was no tunability of the dual-mode separation.
Chapter 4 covers the background behind ring microresonators and how they are designed in our group in order to realise the dual-mode scheme. An AlN resonator, in which our group has previously demonstrated octave-spanning soliton comb generation, was characterised and this time a slotted laser rather than a TSL was used as a pump source. Despite difficulty in obtaining the correct polarisation in order to generate the soliton state, it was eventually shown that the soliton could be reliably generated using a slotted laser as a pump source. The resulting comb was shown to have a higher level of noise compared with the comb generated using the TSL, which is to be expected due to the broader linewidth of the slotted laser compared with the TSL. This was an important result as it showed that a small semiconductor laser which is well-suited to photonic integration has the ability to generate octave spanning frequency combs. If these devices could have their power amplified on chip, or if the Q factor of the microresonator is high enough ($> 5\times10^6$) such that less power is required to pump, then the need for EDFA would be eliminated, making way for complete chip-scale integration of the resonator and pump source.
Chapter 5 shows the results of using the dual-mode scheme, this time in a Si_3N_4 resonator for turn-key operation and microwave generation. These results had previously been demonstrated using a TSL but now the same result is obtained using one of our slotted lasers as well as a commercial packaged semiconductor laser. By quickly step-tuning the wavelength of a slotted laser using a current source connected to an arbitrary waveform generator, turn-key generation of the soliton state was repeatedly and reliably generated with a slotted laser. It was also shown that it is possible to generate a dual-comb using a packaged device. Generating a stable dual-comb consisting of a primary comb and a single soliton comb simultaneously allows for the synthesis of beat notes at microwave frequency scale.

Ultimately, we demonstrated that the large tunable semiconductor laser used in our work on comb generation could be replaced by a slotted semiconductor laser with only modest depreciation in parameters such as the soliton existence range and the coherence of the generated signals. Considering the ease of fabrication and potential for photonic integration of these devices, this represents a significant step towards miniaturising the entire comb generation system to chip-scale and improving the viability of this technology for practical applications.

6.2 Future Work

Much work still needs to be done in optimising the designs of both the slotted lasers as well as the microresonators themselves. The ultimate goal is to be able to completely integrate both the resonator and the pump laser on the same chip. Accomplishing this requires the elimination of the EDFA which is currently necessary to produce adequate pump power. This could be accomplished through the improvement of the resonator quality factor. A Q of 10 million for example would require optical power of tens of milliwatts for comb generation, which is much more attainable for an integrable device with an SOA section to boost on-chip power. Further optimisation of the SOA section could allow for the improvement of the optical power of the lasers while the Q factor can be improved by refining of the microresonator manufacturing process, or the investigation of new materials.
A phase noise measurement system has also been implemented in the lab. However, due to the low power of the comb lines after passing through the filter to isolate single lines, a phase noise characterisation of the comb lines was not possible. It would be desirable to optimise this setup such that the phase noise of the comb lines could be characterised and compared with the noise of the pump used to generate the comb.

Bibliography

[1] David J Jones et al. "Frequency comb generation using femtosecond pulses and cross-phase modulation in optical fiber at arbitrary center frequencies". In: *Optics letters* 25.5 (2000), pp. 308–310.

[2] R Holzwarth et al. "Optical frequency synthesizer for precision spectroscopy". In: *Physical review letters* 85.11 (2000), p. 2264.

[3] Th Udem, Ronald Holzwarth, and Theodor W Hänsch. "Optical frequency metrology". In: *Nature* 416.6877 (2002), pp. 233–237.

[4] Scott A Diddams et al. "Direct link between microwave and optical frequencies with a 300 THz femtosecond laser comb". In: *Physical review letters* 84.22 (2000), p. 5102.

[5] Scott A Diddams et al. "Design and control of femtosecond lasers for optical clocks and the synthesis of low-noise optical and microwave signals". In: *IEEE Journal of Selected Topics in Quantum Electronics* 9.4 (2003), pp. 1072–1080.

[6] Ian Coddington et al. "Rapid and precise absolute distance measurements at long range". In: *Nature photonics* 3.6 (2009), pp. 351–356.

[7] Takuro Ideguchi et al. "Coherent Raman spectro-imaging with laser frequency combs". In: *Nature* 502.7471 (2013), pp. 355–358.

[8] David A Long et al. "Multiplexed sub-Doppler spectroscopy with an optical frequency comb". In: *Physical Review A* 94.6 (2016), p. 061801.

[9] Daryl T Spencer et al. "An optical-frequency synthesizer using integrated photonics". In: *Nature* 557.7703 (2018), pp. 81–85.

[10] Tara E Drake et al. "Terahertz-rate Kerr-microresonator optical clockwork". In: *Physical Review X* 9.3 (2019), p. 031023.

[11] Scott A. Diddams. *Frequency combs*. URL: https://www.mpq.mpg.de/6512235/frequencycombs.

[12] Pascal Del'Haye et al. "Octave spanning tunable frequency comb from a microresonator". In: *Physical Review Letters* 107.6 (2011), p. 063901.

[13] Yoshitomo Okawachi et al. "Octave-spanning frequency comb generation in a silicon nitride chip". In: *Optics letters* 36.17 (2011), pp. 3398–3400.

[14] Tobias Herr et al. "Temporal solitons in optical microresonators". In: *Nature Photonics* 8.2 (2014), pp. 145–152.

[15] Akira Hasegawa and Frederick Tappert. "Transmission of stationary nonlinear optical pulses in dispersive dielectric fibers. I. Anomalous dispersion". In: *Applied Physics Letters* 23.3 (1973), pp. 142–144.

[16] Haizhong Weng et al. "Directly accessing octave-spanning dissipative Kerr soliton frequency combs in an AlN microresonator". In: *Photonics Research* 9.7 (2021), pp. 1351–1357.

[17] Haizhong Weng et al. "Octave-spanning Kerr solitons with repetition rates of 1, 2, and 3 THz in a Si3N4 microresonator". In: *CLEO: Science and Innovations*. Optica Publishing Group. 2022, SW4H–7.

[18] Xingchen Ji et al. "Methods to achieve ultra-high quality factor silicon nitride resonators". In: *APL Photonics* 6.7 (2021), p. 071101.

[19] Nicolas Volet et al. "Micro-resonator soliton generated directly with a diode laser". In: *Laser & Photonics Reviews* 12.5 (2018), p. 1700307.

[20] Boqiang Shen et al. "Integrated turnkey soliton microcombs". In: *Nature* 582.7812 (2020), pp. 365–369.

[21] Wei-Hua Guo et al. "Integrable slotted single-mode lasers". In: *IEEE Photonics Technology Letters* 24.8 (2012), pp. 634–636.

[22] Qiaoyin Lu et al. "Tunable single mode laser array based on slots". In: *2013 Optical Fiber Communication Conference and Exposition and the National Fiber Optic Engineers Conference (OFC/NFOEC)*. IEEE. 2013, pp. 1–3.

[23] Azat Abdullaev et al. "Improved performance of tunable single mode laser array based on non uniformly spaced slots". In: *CLEO: Applications and Technology*. Optical Society of America. 2015, JTh2A–3.

[24] Qiaoyin Lu et al. "Slotted single mode lasers integrated with a semiconductor optical amplifier". In: *IEEE Photonics Technology Letters* 25.6 (2013), pp. 564–567.

[25] Michael McDermott et al. "1.3 μm wavelength tunable single-mode laser arrays based on slots". In: *Optics Express* 29.10 (2021), pp. 15802–15812.

[26] Per Malm. "A Polarisation Coupled Diode Laser System for Photodynamic Therapy". In: (Nov. 2002).

[27] G Thompson and P Kirkby. "(GaAl) As lasers with a heterostructure for optical confinement and additional heterojunctions for extreme carrier confinement". In: *IEEE Journal of Quantum Electronics* 9.2 (1973), pp. 311–318.

[28] Keang-Po Ho. "Advanced Topics in Lightwave Communications Generation of Optical Signals". In: (Feb. 2005).

[29] Larry A Coldren, Scott W Corzine, and Milan L Mashanovitch. *Diode lasers and photonic integrated circuits*. Vol. 218. John Wiley & Sons, 2012.

[30] LD Westbrook. "Measurements of dg/dN and dn/dN and their dependence on photon energy in λ= 1.5 μm InGaAsP laser diodes". In: *IEE Proceedings J (Optoelectronics)* 133.2 (1986), pp. 135–142.

[31] Qiaoyin Lu et al. "Design of slotted single-mode lasers suitable for photonic integration". In: *IEEE Photonics Technology Letters* 22.11 (2010), pp. 787–789.

[32] MJ Wallace et al. "Tuning behaviour of slotted vernier widely tunable lasers". In: *Optics express* 27.12 (2019), pp. 17122–17137.

[33] Peter Bienstman. "Rigorous and efficient modelling of wavelenght scale photonic components". PhD thesis. Ghent University, 2001.

[34] Michael J Wallace et al. "Genetic algorithm optimization of high order surface etched grating tunable laser array". In: *Optics Express* 28.6 (2020), pp. 8169–8184.

[35] Jens Buus, Markus-Christian Amann, and Daniel J Blumenthal. *Tunable laser diodes and related optical sources*. John Wiley & Sons Hoboken, New Jersey, 2005.

[36] J-P Weber. "Optimization of the carrier-induced effective index change in InGaAsP waveguides-application to tunable Bragg filters". In: *IEEE Journal of Quantum Electronics* 30.8 (1994), pp. 1801–1816.

[37] J-P Weber. "Optimization of the carrier-induced effective index change in InGaAsP waveguides-application to tunable Bragg filters". In: *IEEE Journal of Quantum Electronics* 30.8 (1994), pp. 1801–1816.

[38] Gorachand Ghosh. "Temperature dispersion of refractive indices in semiconductors". In: *Journal of applied physics* 79.12 (1996), pp. 9388–9389.

[39] K Chinen et al. "Low-threshold 1.55-μm InGaAsP/InP buried heterostructure distributed feedback lasers". In: *Applied physics letters* 51.4 (1987), pp. 273–275.

[40] Fu-Li Wang et al. "Relative intensity noise in high-speed hybrid square-rectangular lasers". In: *Photonics Research* 6.3 (2018), pp. 193–197.

[41] A. L. Schawlow and C. H. Townes. "Infrared and Optical Masers". In: *Phys. Rev.* 112 (6 1958), pp. 1940–1949.

[42] Melvin Lax. "Classical noise. V. Noise in self-sustained oscillators". In: *Physical Review* 160.2 (1967), p. 290.

[43] H Gerhardt, H Welling, and A Güttner. "Measurements of the laser linewidth due to quantum phase and quantum amplitude noise above and below threshold. I". In: *Zeitschrift für Physik* 253.2 (1972), pp. 113–126.

[44] Charles Henry. "Theory of the linewidth of semiconductor lasers". In: *IEEE Journal of Quantum Electronics* 18.2 (1982), pp. 259–264.

[45] Wenle Weng et al. "Gain-switched semiconductor laser driven soliton microcombs". In: *Nature communications* 12.1 (2021), p. 1425.

[46] Peicheng Liao et al. "Dependence of a microresonator Kerr frequency comb on the pump linewidth". In: *Optics Letters* 42.4 (2017), pp. 779–782.

[47] Hisanao Sato and Jun Ohya. "Theory of spectral linewidth of external cavity semiconductor lasers". In: *IEEE journal of quantum electronics* 22.7 (1986), pp. 1060–1063.

[48] Azat Abdullaev et al. “Linewidth characterization of integrable slotted single-mode lasers”. In: *IEEE Photonics Technology Letters* 26.22 (2014), pp. 2225–2228.

[49] Wei-Hua Guo et al. “Nine-channel wavelength tunable single mode laser array based on slots”. In: *Optics Express* 21.8 (2013), pp. 10215–10221.

[50] Qiaoyin Lu et al. “31nm quasi-continuous tuning single mode laser array based on slots”. In: *CLEO: Applications and Technology*. Optica Publishing Group. 2014, JW2A–77.

[51] Gaurav Jain et al. “Design optimization for semiconductor lasers with high-order surface gratings having multiple periods”. In: *Journal of Lightwave Technology* 36.22 (2018), pp. 5121–5129.

[52] Naoki Hashizume and Hideyuki Nasu. “Mode hopping control and lasing wavelength stabilization of fiber grating lasers”. In: *Furukawa Review* 20 (2001), pp. 7–10.

[53] Takanori Okoshi, Kazuro, and Akira Nakayama. “Novel method for high resolution measurement of laser output spectrum”. In: *Electronics letters* 16.16 (1980), pp. 630–631.

[54] Tam N Huynh, Lim Nguyen, and Liam P Barry. “Phase noise characterization of SGDBR lasers using phase modulation detection method with delayed self-heterodyne measurements”. In: *Journal of lightwave technology* 31.8 (2013), pp. 1300–1308.

[55] Andrey S Voloshin et al. “Dynamics of soliton self-injection locking in optical microresonators”. In: *Nature communications* 12.1 (2021), p. 235.

[56] Tobias J Kippenberg, Ronald Holzwarth, and Scott A Diddams. “Microresonator-based optical frequency combs”. In: *science* 332.6029 (2011), pp. 555–559.

[57] George A Sefler. “Frequency comb generation by four-wave mixing and the role of fiber dispersion”. In: *Journal of lightwave technology* 16.9 (1998), p. 1596.

[58] John Heebner, Rohit Grover, and Tarek Ibrahim. *Optical microresonator theory*. Springer, 2008.

[59] Ioannis Chremmos, Otto Schwelb, and Nikolaos Uzunoglu. *Photonic microresonator research and applications*. Vol. 156. Springer, 2010.

[60] Wim Bogaerts et al. “Silicon microring resonators”. In: *Laser & Photonics Reviews* 6.1 (2012), pp. 47–73.

[61] Jacob Levy. “Integrated nonlinear optics in silicon nitride waveguides and resonators”. In: (2011).

[62] Govind P Agrawal. “Nonlinear fiber optics: its history and recent progress”. In: *JOSA B* 28.12 (2011), A1–A10.

[63] T Hansson, D Modotto, and S Wabnitz. “Dynamics of the modulational instability in microresonator frequency combs”. In: *Physical Review A* 88.2 (2013), p. 023819.

[64] N Yu Dmitriev et al. "Measurement of Dispersion Characteristics of Integrated Optical Microresonators and Generation of Coherent Optical Frequency Combs". In: *Journal of Experimental and Theoretical Physics* 135.1 (2022), pp. 9–19.

[65] T Herr et al. "Universal formation dynamics and noise of Kerr-frequency combs in microresonators". In: *Nature photonics* 6.7 (2012), pp. 480–487.

[66] Shun Fujii and Takasumi Tanabe. "Dispersion engineering and measurement of whispering gallery mode microresonator for Kerr frequency comb generation". In: *Nanophotonics* 9.5 (2020), pp. 1087–1104.

[67] Tobias J Kippenberg et al. "Dissipative Kerr solitons in optical microresonators". In: *Science* 361.6402 (2018), eaan8083.

[68] Victor Brasch et al. "Photonic chip–based optical frequency comb using soliton Cherenkov radiation". In: *Science* 351.6271 (2016), pp. 357–360.

[69] Chaitanya Joshi et al. "Thermally controlled comb generation and soliton modelocking in microresonators". In: *Optics letters* 41.11 (2016), pp. 2565–2568.

[70] Zheng Gong et al. "High-fidelity cavity soliton generation in crystalline AlN micro-ring resonators". In: *Optics letters* 43.18 (2018), pp. 4366–4369.

[71] Hairun Guo et al. "Universal dynamics and deterministic switching of dissipative Kerr solitons in optical microresonators". In: *Nature Physics* 13.1 (2017), pp. 94–102.

[72] Qing Li et al. "Stably accessing octave-spanning microresonator frequency combs in the soliton regime". In: *Optica* 4.2 (2017), pp. 193–203.

[73] Haizhong Weng et al. "Dual-mode microresonators as straightforward access to octave-spanning dissipative Kerr solitons". In: *Apl Photonics* 7.6 (2022), p. 066103.

[74] Travis C Briles et al. "Generating octave-bandwidth soliton frequency combs with compact low-power semiconductor lasers". In: *Physical Review Applied* 14.1 (2020), p. 014006.

[75] Xu Yi et al. "Soliton frequency comb at microwave rates in a high-Q silica microresonator". In: *Optica* 2.12 (2015), pp. 1078–1085.

[76] Qi-Fan Yang et al. "Stokes solitons in optical microcavities". In: *Nature Physics* 13.1 (2017), pp. 53–57.

[77] Zhonghan Wu et al. "Coexistence of multiple microcombs in monochromatically pumped Si 3 N 4 microresonators". In: *Optics Letters* 47.5 (2022), pp. 1190–1193.